A Transport Equation Approach to Modeling the Influence o f Surface Roughness on Boundary Layer Transition

Christopher M. Langel, Raymond Chow, and C.P. van Dam

David C. Maniaci, Sandia Technical Manager

Ⓜ **Sandia National Laboratories**

A Transport Equation Approach to Modeling the Influence of Surface Roughness on Boundary Layer Transition [*]

Christopher M. Langel, Raymond Chow, and C.P. van Dam
Department of Mechanical and Aerospace Engineering
University of California, Davis
Davis, CA 95616

Sandia Contract No. 1228734

Technical Manager:

David C. Maniaci
Wind Energy Technologies Department
Sandia National Laboratories
P.O. Box 5800
Albuquerque, NM 87185-1124

Abstract

A computational investigation has been performed to better understand the impact of surface roughness on the flow o ver a c ontaminated s u rface. T his re port hi ghlights t he i mplementation a n d d evelopment of the roughness amplification m odel i n t he fl ow so lver OV ER FLOW-2. Th e mo del, or iginally pr oposed by Dassler, Kozulovic, and Fiala, introduces an additional scalar field r oughness a mplification qu an tity. This value is explicitly set at rough wall boundaries using surface roughness parameters and local flow quantities. The additional transport equation allows non-local effects of surface roughness to be accounted for downstream of rough sections. This roughness amplification v ariable i s c oupled w ith t he Langtry-Menter model and used to modify the criteria for transition. Results from flat plate test cases show good agreement with experimental transition behavior on the flow o ver v arying s and g rain r oughness h e ights. Additional validation studies were performed on a NACA 0012 airfoil with leading edge roughness. The computationally predicted boundary layer development demonstrates good agreement with experimental results. New tests using varying roughness configurations h ave b een c arried o ut at t he Texas A &M O ran W. N icks Low Speed Wind Tunnel to provide further calibration of the roughness amplification m ethod. An o verview and preliminary results are provided of this concurrent experimental investigation.

---

[*]The work described in this report was performed for Sandia National Laboratories under Contract No. 1228734

Acknowledgment

Contents

References 91

List of Figures

9

List of Tables

Nomenclature

Re_k — Roughness Reynolds number ($Re_k = U_k k_s / \nu$)

$Re_{k,cr}$ — Critical roughness Reynolds number

U_k — Flow velocity at roughness height

k_s — Roughness height

k^+ — Dimensionless roughness height ($k^+ = \mu_t k_s / \nu$)

k/c — Roughness height non-dimensionalized by airfoil chord

A_r — Roughness amplification quantity

θ — Boundary layer momentum thickness

δ^* — Boundary layer displacement thickness

H — Boundary layer shape factor (δ^*/θ)

Re_θ — Momentum thickness Reynolds number ($Re_\theta = \theta U_e / \nu$)

$\tilde{Re}_{\theta,t}$ — Local transition onset momentum thickness Reynolds number (computed from transport equation)

$Re_{\theta,t}$ — Transition onset momentum thickness Reynolds number (computed from correlation function)

Re_ν — Vorticity/strain-rate Reynolds number

γ — Intermittency variable in Langtry-Menter transition model

Tu — Freestream turbulence intensity

DNS — Direct numerical simulation

LES — Large eddy simulation

DES — Detached eddy simulation

RANS – Reynolds averaged Navier-Stokes

SST — Shear stress transport turbulence model

LCTM – Local correlation transition model

FSTI — Freestream turbulence intensity

HLLC – Harten-Lax-van Leer contact wave

SSOR – Successive symmetric over-relaxation

LSWT – Low Speed Wind Tunnel

Chapter 1

Introduction

The effect of surface roughness on the flow over bodies and lifting surfaces has been studied for almost a century, and there have been a large number of experimental studies that document how roughness changes flow properties. Despite such studies, a comprehensive analytical description, or even a robust and effective computational method to predict detailed flow behavior over a rough surface has eluded the engineering and scientific communities. As there are many factors outside the roughness itself that can change its interaction with the surrounding flow field, and even the most fundamental effects can be quite physically complicated, studies attempting to describe the influence of roughness must keep a narrow scope. This means reducing cases studied to very specific roughness distributions, freestream conditions, surface geometries, and more. As a result, extending the results from the experiments to more complex roughness configurations has been a substantial challenge for many researchers.

The role of surface roughness in many flow applications is of great practical importance as a well known effect is the acceleration of the laminar-turbulent transition process. The implications of the premature appearance of turbulent flow are vast due to the changes in skin friction, heat transfer, and gas mixing properties. There is an interest in understanding the effects of surface roughness across many engineering disciplines, for example the effects seen in gas turbines to better approximate maintenance cycles [1], applications to icing effects seen on aircraft wings [2], and combustion analysis [3].

The wind industry in particular has seen a recent rise in interest regarding the effects of surface roughness for several reasons [4]. For one, accurate prediction of wind turbine power output is fundamental to integration of wind power systems into existing infrastructure. Surface roughness can have a substantial impact on the aerodynamic properties of the blades by influencing boundary layer development over contaminated sections [5]. Furthermore, the changes in the flow over rough portions extends to the performance of the full turbine, potentially reducing power output and annual energy capture significantly. Additionally, many airfoils intended specifically for use on utility scale wind turbines were designed to be lift insensitive to surface roughness due to the expected environmental conditions [6, 7]. Field observations are showing this is frequently not the case, so there is a renewed interest in examining roughness sensitivity for airfoil design [8]. This poses numerous challenges due to the limited number of roughness configurations that have been thoroughly analyzed, and the non-trivial extension of roughness effects. As physically testing each profile is not practical, numerical design and optimization methods are used to generate airfoils with desired properties. However, there are limited computational techniques availible to analyze the effects that surface roughness will have on the aerodynamic performance.

For the purpose of both accurate power prediction and roughness insensitive airfoil design, a robust computational method that predicts the effects of various surface roughness distributions has been desired. The objective of the work presented this thesis was to develop and implement a computational roughness model into the flow solver OVERFLOW-2 [9] that allows the influence of surface roughness to be included in

engineering simulations. The approach taken was to add an additional global field quantity and corresponding transport equation to create a region of roughness influence where modifications to the transition and turbulence characteristics can be made accordingly. A primary goal is that the method must be able to accurately simulate configurations outside what has been tested experimentally, allowing the model to predict the aerodynamic behavior around observed in-field roughness, and to be used in future design optimization.

The current work is part of an on-going collaboration between University of California, Davis; Texas A&M University; and Sandia National Laboratories. Experimental tests are being carried out at the Texas A&M Oran W. Nicks Low Speed Wind Tunnel (LSWT) to provide high quality experimental data for the roughness model to be validated against. Sandia serves to oversee the collaboration and provides HPC resources on RedSky for model calibration. In addition to describing the proposed roughness model the present work provides a detailed description and further validation of the underlying Langtry-Menter transition model, the platform on which the roughness modification is built. Finally a number of validation studies are provided to demonstrate the effectiveness and potential of the roughness amplification method.

Chapter 2

Literature Overview

The review of literature is divided into four different topics that the current work spans. A brief overview of the laminar-turbulent transition process is presented, followed by an account of various transition prediction methodologies. Additionally, a few historical experimental investigations of the effects of roughness on both transition, and other flow properties are summarized. Finally attempts at modeling the influence of surface roughness are presented and the current work is introduced. As both boundary-layer transition and the effects of surface roughness are far from well understood, and the body of work on both topics is vast, the review does not attempt to be fully comprehensive, but hopes to provide a platform on which the present model is built.

Transition Process

The laminar-turbulent transition region has been the subject of scientific investigation nearly as long as the process has known to exist. In nearly every example of a solid bounded flow, the result is a growth of a laminar boundary layer profile followed by breakdown into a fully turbulent state. As the difference between a laminar and turbulent flow are substantial from both a physical and practical engineering standpoint, it has long been the objective of researchers to better understand the transition process. It is often viewed as a stability problem, where the laminar boundary layer can be thought of as the ground state, and transition to turbulence as the system going unstable.

The governing equations in fluid dynamics are the Navier-Stokes (NS), along with the mass and energy conservation equations. The full conservation equation set does contain the physical phenomena of the turbulent breakdown. However, the complexity of the system of equations equations renders a full analytical solution essentially impossible. For the study of boundary layers the simplification of incompressibility and locally parallel flow is usually made. Applying the principles of linear stability analysis to the simplified NS equations yields the Orr-Sommerfeld (OS) equation. At the present, solutions are obtained numerically for various initial disturbances, as even with the simplifications introduced the OS equation does not have a general analytical solution. Due to the fact modern computational techniques were unavailable when the stability of laminar boundary layers was initially studied, the assumption of inviscid flow was made to further simplify the OS equation. Lord Rayleigh studied the inviscid OS equation extensively around the turn of the 20th century, and determined that a laminar boundary layer should remain stable unless there is an inflection in the velocity profile [10]. Although this is indeed criteria to trigger transition onset, which is now referred to as a Rayleigh instability, the condition proved to be insufficient. It was observed experimentally that even very simple flows would transition to turbulent without ever experiencing an inflection.

Following the initial work, Prandtl reasoned that viscosity must somehow contribute to the transition

process due to the discrepancies in inviscid analysis. The destabilizing effect of viscosity, and the existence of wave like perturbations causing transition was debated until the famous experiment of Schubauer and Skramstad [11]. Moving forward the scientific community began a rigorous study of the non-linear stability of the OS equation and a large number of experiments on the transition process. Under stable conditions, small disturbances within the boundary layer are dissipated away and the flow remains l aminar. However, as the laminar boundary layer grows, the flow becomes susceptible to destabilizing disturbance frequencies that can cause the perturbations to grow in magnitude. The initial viscously amplified growth of disturbances became known as Tollmien-Schlichting (TS) waves [11].

The appearance of Tollmien-Schlichting waves marks the first step in the "natural transition" process. Once the disturbance has grown to a point where the mean flow profile is altered, the boundary layer becomes susceptible to another band of disturbance frequencies which accelerates the process by which fluctuations are amplified. These secondary instabilities are three dimensional in nature and can take multiple forms. They are referred to as K-type, H-type, and C-type instabilities and named after Klebanoff [12], Herbert [13], and Craik [14] respectively for their initial contributions. After secondary disturbances are introduced, there is a rapid appearance of isolated turbulent spots, followed by a complete breakdown into a turbulent boundary layer. As the growth of the second band of disturbance frequencies is inherently non-linear, linear stability analysis fails to predict the secondary breakdown. This process is by no means universal and is extremely sensitive to freestream turbulence levels [15], surface conditions [7], external noise [16], and more making it very difficult to quantize generally.
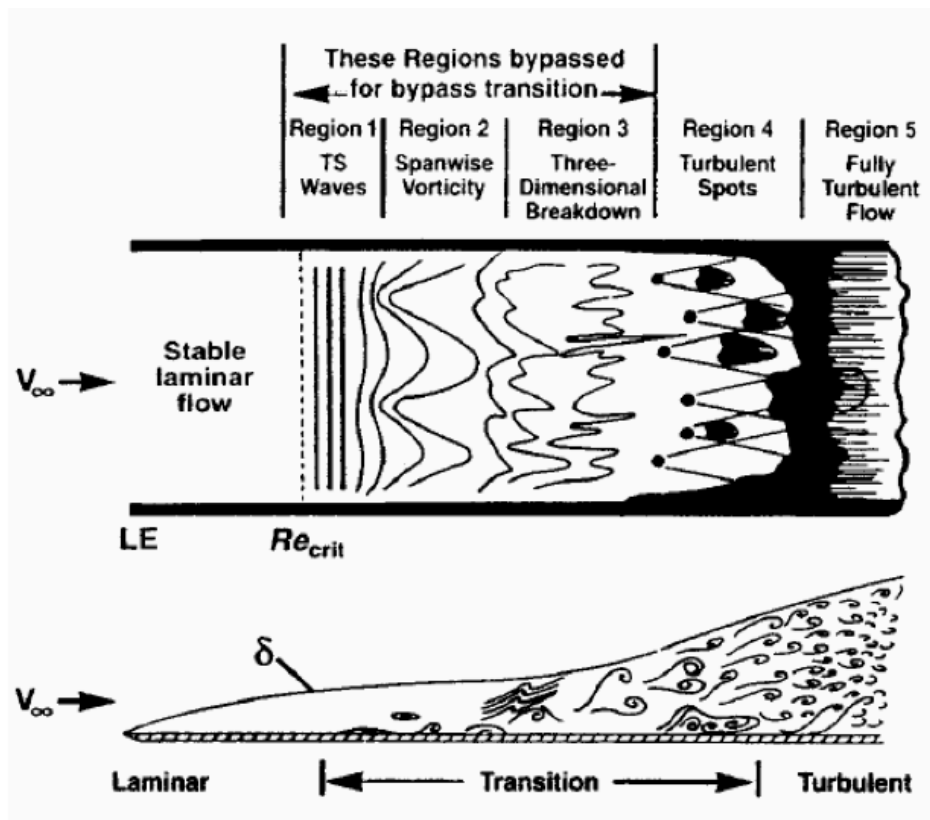
Figure 2.1. Stages of natural transition and sketch of developing boundary layer, adapted from Schlichting [17]

An enveloping term to describe a transition process that is missing one or more of the steps listed above is "bypass transition". Aptly named by Morkovin [18], an external disturbance can introduce a strong enough perturbation to introduce secondary disturbances without going through the viscous TS amplification process. Bypass transitions are often attributed to high freestream turbulence levels where strong freestream fluctuations can introduce large disturbances into the boundary layer. Tollmien-Schlichting waves are known to be absent in the transition process where the freestream turbulence level exceeds 1% [3]. Other ways the transition process can be accelerated, and the initial steps bypassed is through the influence of surface roughness, or encounters with external jets of fluid. As the term is given to a number of different paths to transition, and it is an inherently nonlinear phenomena, there is no known analytical means of describing the evolution of a bypass transition once triggered.

Other flow features that can initiate a bypass transition include laminar separation bubbles and wake induced transition in turbomachinery and airplane multi-element high lift systems [19, 20]. Several different modes of separation are known to exist. The flow can remain separated, as in a high Reynolds number flow around bluff bodies or around an airfoil in stall. Both of these scenarios will introduce large turbulent spots in the separated region. Additionally a "separation bubble" may form where after the initial separation, the flow reattaches under the presence of favorable flow conditions. Separation bubble induced transition depends strongly on the size of the bubble that is influenced by the surface geometry and freestream conditions [3, 21]. The boundary layer experiences an inflection over the bubble, a well known inviscid instability. Wake induced transition refers to the periodic turbulent wakes downstream vanes are subjected to in gas turbines. Frequently the interaction from the wake of an upstream vane immediately introduces turbulent spots into the laminar boundary layer of downstream vanes [22, 23]. For flows over three dimensional swept wings, spanwise variations in velocity can introduce additional disturbances that can interact with the TS waves or create an entirely new instability mechanism. The appearance of a new instability due to spanwise velocity fluctuations is referred to as a crossflow instability [24].

Transition Prediction

Understanding the physical process has only been half of the equation regarding research on the transition process. Predicting the onset of transition has its importance across many fields and various flow applications. Attempts at modeling the process have ranged from purely mathematical to correlations based on various experimental observations. Through proper direct numerical simulation (DNS), transition onset due to all possible mechanisms can be predicted. DNS can be regarded as a rigorous mathematical determination as it represents the full governing equation set. The drawback is the computational cost associated with such simulations and at the present time, DNS primarily serves to validate and calibrate simplified transition models. A slightly simplified alternative to DNS is the space filtered models of large eddy simulations (LES). Provided the grid spacing is fine enough, certain implicit formulations in LES can theoretically predict transition. However the computational power required still places these LES models in the realm of impracticality for everyday simulations [25].

Linear Stability Models (e^N)

One of the more popular and frequently utilized models that does not inherently require a an impractically fine mesh, such as in DNS and LES, is referred to as the e^N method [26]. It is based on linear stability analysis and can predict the naturally occurring amplification of TS waves well under certain con-

ditions [27]. As long as the growth of the disturbances remain linear, the linearization represents an accurate solution to the NS momentum equations [28]. The panel code X-FOIL utilizes the e^N method in its prediction of transition location, however there has been limited success in implementation in Reynolds-averaged (RANS) codes for reasons discussed below. The fundamental process of the e^N method requires multiple steps.

1. Obtain flow solution based on the assumption the flow is laminar

2. Calculate the amplification rate of a natural TS disturbance based off the laminar solution

3. Integrate growth rates in the boundary layer in the streamwise direction until a critical amplitude ratio (e^N) is reached.

The underlying idea is that the flow will be laminar until the point of transition and the initial amplification of the disturbances is linear within that laminar profile. One can see the challenge associated with implementation for a 3-D flow as the streamline may not follow an underling direction provided by the grid topology. There also needs to be a slight empirical justification for the choice of the N factor. This is regarded as how the model is adjusted for changes to freestream turbulence levels and other outside factors that influence transition. An N value of 9 is generally taken as the default, however in highly turbulent environments it can be much lower [27].

There are a number of other non-ideal attributes of the e^N method as it is not equipped to predict any form of bypass transition. For example, the linear stability analysis fails to account for surface roughness induced transition as the perturbations immediately send the flow into the non-linear regime, entirely voiding the validity of the linearization. In addition to only being capable of predicting the "natural" transition process, the e^N method requires the computation of integral values, which is a challenge to implement into parallizable CFD codes. Other similar models that use a multiple step calculation of disturbance growth rates have been implemented including a study performed at UC Davis [29, 30]. Despite slightly different formulations, most end up suffering from the same issues when attempting to implement in a general CFD code: the dependence on non-local information, very high near wall grid resolution, and the inability to predict bypass transition mechanisms other than those associated with natural amplification of disturbances in the form of TS waves.

Correlation Based Models

An alternative to the mathematical based models, where at least a portion of the turbulent breakdown is represented from a physical perspective is that of correlation modeling. A frequently used correlation relates the freestream turbulence levels to the momentum thickness Reynolds number (Re_θ), see Figure 2.2.

In a similar manner to the e^N process, a fully laminar solution is assumed, then the momentum thickness Reynolds number is computed at all locations. The Re_θ values are then compared to the empirical correlation to determine the location of the onset of transition. Correlation based methods have an inherent advantage over linear stability methods as other modes of transitions can be predicted with correlation models. The dependence on freestream turbulence allows correlation based models to account for by-pass transition mechanisms associated with external disturbances. Correlations from Abu-Ghannam and Shaw [31] and Mayle [3] have been implemented with relatively high levels of success, however, there are still challenges associated with the calculation of Re_θ across the domain. In a Navier-Stokes solver the computation of momentum thickness is also challenging due to need to define a boundary layer edge. For proper
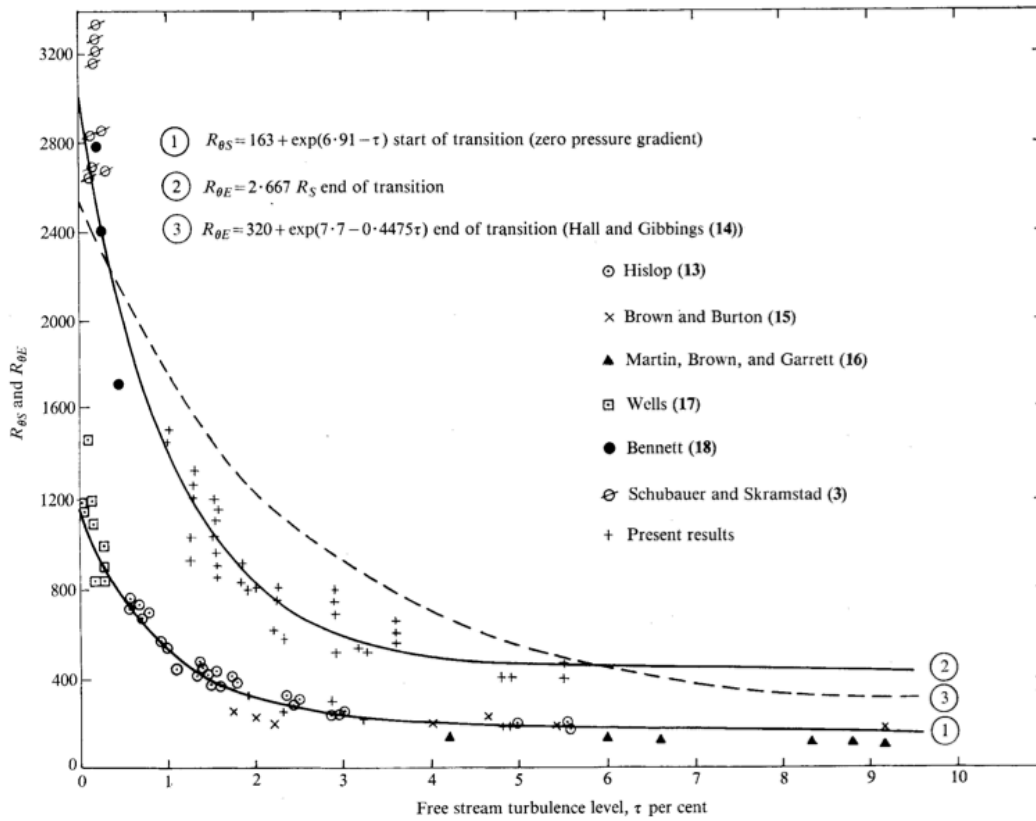
Figure 2.2. Plot of Re_θ correlations against freestream turbulence intensity, adapted from Abu-Ghannam and Shaw [31]

implementation, a search algorithm is required increasing the computational costs and the complications compound when using unstructured grids, or in a parallel architecture environment.

Low-*Re* Models

Most widely used turbulence models do not have the capacity to represent the transition process. Certain low-Reynolds number (low-*Re*) turbulence models do have the potential to predict transition when applied to three dimensional flows and parallel codes [32]. These turbulence models are designed to predict the viscous sublayer behavior so they function well without the use of wall functions. At relatively high freestream turbulence levels, several models have demonstrated an ability to predict the location of transition onset. Nonetheless, low-*Re* methods have proven to frequently estimate the onset of transition too early and do not have any sensitivity to pressure gradients. Despite being able to match up with selected experimental cases, the lack of any sort of robust prediction has prohibited the wide spread use of low-*Re* turbulence models.

19

Intermittency

Both e^N and correlation based methods are capable of predicting the onset of transition, however once initialized, the length of the transition region and any other flow effects caused by transitional zone are usually excluded. The concept of an intermittency factor dates back to 1950's when Dhawan and Narasimha introduced an algebraic function that prescribed the evolution of the transitional boundary layer once the process had been triggered [33]. A number of different algebraic models have been proposed including those by Gostelow [34], and Steelant and Dick [35]. Most intermittency models serve as a scaling factor to the turbulent eddy viscosity, taking a value between zero and one and scaling based on a prescribed algebraic function. Intermittency models require the use of a triggering mechanism to mark the onset of transition and are frequently coupled with an Re_θ correlation.

Local Correlation Based Models

Despite the inherent difficulties encountered in transition modeling, the necessity to include a predictive mechanism for the accuracy of flow simulations has continued to push the development of transition models. The next step forward was the application of transport equations to correlation based approaches eliminating the need to compute integral values along the length of the boundary layer. In addition to eliminating the computational costs associated with the integral computations, the transport equation approach eliminates the need to define the boundary layer edge or a stream direction. Transport equations were also applied to the concept of intermittency in order to accommodate the localized effects rather than relying on a predetermined algebraic function. Menter et al. introduced the concept referred to as local correlation transition modeling (LCTM) whereby a transport equation for both the transition onset momentum thickness Reynolds number ($Re_{\theta t}$) and intermittency (γ) are introduced simultaneously and coupled to the SST turbulence model [36]. Recently, the model was further developed by Langtry over the course of his doctoral studies and has been implemented successfully in a number of industrial and research CFD codes [37]. Chapter 4 of the current work provides a detailed description of the Langtry-Menter transition model.

Roughness Effects

Surface roughness can significantly alter the flow field over a contaminated surface, introducing velocity perturbations, increasing the momentum deficit in the boundary layer, and altering transition characteristics. [38]. A frequently studied effect of surface roughness is the premature transition of a laminar boundary layer to a turbulent profile [39]. Additionally even more effects are seen as a fully developed turbulent boundary layer has a tendency to thicken over rough sections. This is due to the increase in turbulent fluctuations and subsequent turbulent kinetic energy production over rough surfaces. The early onset of transition and modifications to the fully turbulent boundary layer on an airfoil can increase drag, alter stall characteristics, change the lift-curve slope, and even force the flow to become unsteady.

A crucial component is characterization of the roughness such as the height, shape, and distribution. All must all be taken into consideration to fully understand the effects. The relationship between the height of the roughness element and the flow disturbance induced is not easily correlated. Roughness elements shorter than the height of the viscous sublayer generally have little effect on the transition process as the disturbances are dissipated away due to the high levels of viscous damping [28]. Additionally, as the boundary layer does not have a constant thickness, the effects can not be generalized along the boundary layer of a rough surface.

Accordingly, roughness heights are usually nondimensionalized with respect to the displacement thickness (k/δ^*) or described using a roughness Reynolds number, Re_k. The roughness Reynolds number is defined:

$$Re_k = \frac{\rho U_k k}{\mu} \tag{2.1}$$

where U_k is the velocity in an undisturbed boundary layer at height k. Frequently experimental studies have attempted to identify a critical roughness Reynolds number, $Re_{k,cr}$. This represents the critical value Re_k has to reach to immediately trigger the transition process at the location of the roughness.

Types of roughness have been broadly characterized into three different subsets, beginning with 2-D isolated roughness (such as a trip strip or other protuberance that consistently covers the entire span). Furthermore, a second category describes three dimensional isolated roughness, such as a single hemisphere, cylinder, or other three dimensional shape. Finally there is distributed roughness, which encompasses any sort of arranged group of rough elements and is an inherently three dimensional occurrence. The first two have been studied extensively and relatively consistent results have been seen in various experiments. However, studies on distributed roughness have been plagued by inconsistencies and difficulties generalizing the observed effects [38, 40]. The extremely non-linear nature, and interactions between individual structures create complex flow features that can vary substantially across experiments, and are not practically represented analytically.

Isolated 2-D Roughness

Characterized by a consistent spanwise protuberance, two-dimensional roughness is known to create pockets of separated flow both down and upstream of the 2-D element. The downstream separation can extend vastly beyond the location of the trip strip or other isolated 2-D feature. The flow separation causes an inflection in the velocity profile and produces an inviscid Rayleigh instability. Despite introducing a relatively large disturbance, a 2-D isolated roughness does not immediately introduce turbulent spots into the the boundary layer but rather accelerates the amplification of naturally occurring TS waves [41]. The increase in amplification depends strongly on the height of the roughness relative to the boundary layer thickness (k/δ^*) and can immediately trigger the onset of transition or may only slightly change the transition location compared to a "clean" configuration. Trip strips are considered a controlled way to promote the onset of the natural transition process as the resulting amplification of instability waves can be described by linear stability analysis.

In conjunction with physically altering the boundary layer profile, the roughness element can have additional secondary effects on the boundary layer development. The separated region promotes the receptivity to external disturbances such as freestream turbulence and sound pulses by increasing the momentum deficit downstream of the roughness. Despite being an ideal way to amplify the natural transition process in a closed controlled environment (such as a low turbulence wind tunnel), a 2-D isolated feature can increase the likelihood of a bypass transition in an external environment [42].

Isolated 3-D Roughness

The effects of a three dimensional rough feature on the boundary layer flow are considerable different than those of a 2-D disturbance. A separation pocket does frequently appear behind the isolated element,

however, the downstream extent is considerably less than a 2-D disturbance. Additionally distinctive flow features appear at the location of the isolated feature. Qualitatively, it has been observed that isolated rough elements of various symmetrical shapes introduce similar vortical structures, however differences in $Re_{k,cr}$ have been observed [43]. A number of early investigations on isolated roughness elements were conducted by Tani et al. [44], Gregory and Walker [45], and Mochizuki [46] in the 1940's and 50's. Gregory and Walker utilized a cylindrical shaped rough element, while Mochizuki [46] utilized a single sphere of varying diameters and smoke visualization to explore the flow characteristics. The results from the two studies show similar flow features, and some details from Mochizuki are presented as a canonical representation of flow features around an isolated roughness element. Figure 2.3 shows the effect of varying the freestream velocity on the flow behind the roughness element.
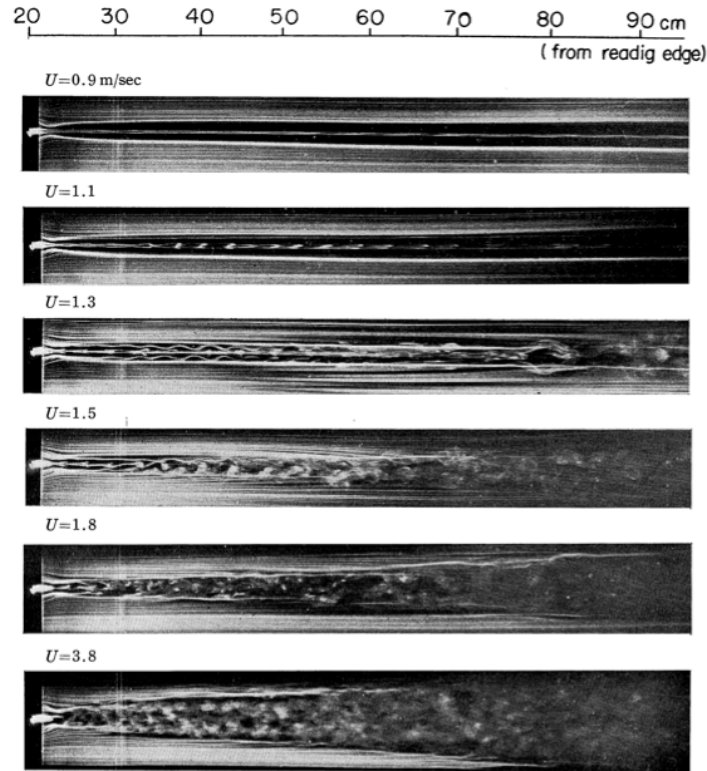
Figure 2.3. Varying freestream velocities and the flow feature generated behind the roughness element, adapted from Mochizuki [46]

The distinctive flow feature of an isolated element is a primary vortex filament that wraps around the sphere creating two symmetric trailing vortices on either side. These symmetric vortices behind the element induce a downwash in the wake [47]. The shape of the induced flow structure has given it the name "horse-shoe vortex". Smoke streaks at various heights that provide a picture of the structure of these vortices are shown in Figure 2.4.

It can be observed in Figure 2.3 at low freestream velocities ($U = 0.9m/s$), a single smoke trail appears behind the rough element. As the velocity is increased ($U = 1.1 - 1.3m/s$), the trailing vortices begin to periodically deform introducing "hairpin" vortex structures, the symmetric feature seen in between the two primary trailing vortices in Figure 2.3 ($U = 1.3m/s$). The existence of hairpin vortices was observed in

22

Mochizuki's experiment [46], however it was not explored in great detail until Acarlar and Smith [43]. The rotation of the hairpin vortices is opposite that of the primary horseshoe structure.

2 mm

4 mm

6 mm
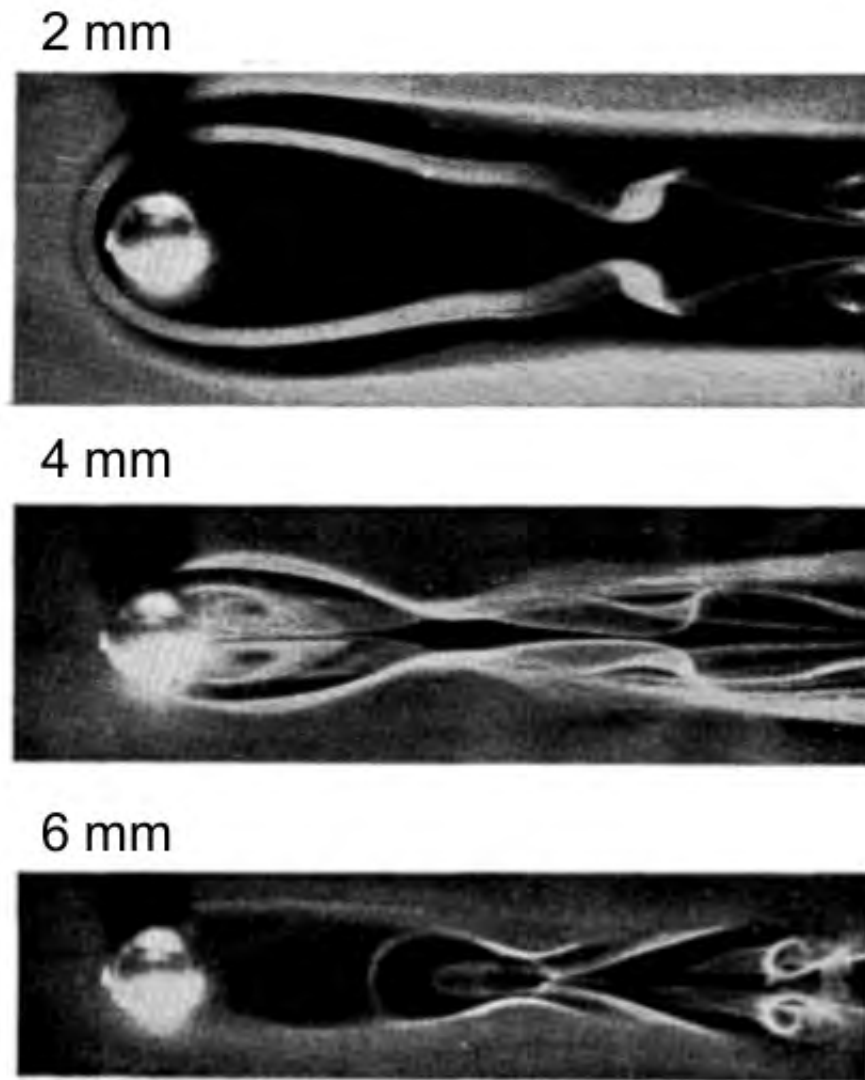
Figure 2.4. Details of the horseshoe vortex system using smoke streaks at various heights, the hairpin structure can also be seen, adapted from Mochizuki [46]

At low Re_k values ($Re_k < 300$), the system of vortices are steady and do not affect the stability of the flow around them. The vortex structures remain isolated until they are pushed up out of the shear layer and dissipated away. As the the value of Re_k increases ($300 - 400$), the horseshoe vortex system becomes unstable and the protuberance begins to shed hairpin vortices periodically. The shedding frequency of the vortices is higher than the critical disturbance band for the amplification of TS waves, therefore the transition process is only slightly accelerated in this range of Re_k. A further increase in Re_k to the critical range (on the order of 400 to 600 depending on the shape of the roughness element) results in the sudden appearance of a turbulent wedge behind the rough element ($U = 3.8m/s$ in Figure 2.3). The wedge rapidly extends and

soon causes a transitional boundary layer bypassing the traditional 2-D amplification process.

Furthermore, a study by Morkovin and Norman showed that if the roughness element extended outside the boundary layer, additional vortex structures are generated up-stream of the roughness [48]. Similarly, at relatively low Re_k values the vortices remain stable and do not promote the transition process. Shedding begins after an increase in Re_k and can result in the collapse and reappearance of the system of vortices as a whole, referred to as "burping". An increase past a critical level will even trigger the transition process upstream of the roughness due to the induced vortex.

Distributed Roughness

Single isolated roughness elements have been studied experimentally, and DNS experiments have been performed at low Reynolds numbers with good agreement and consistency [49]. Despite the susceptibility of the shedding properties to freestream conditions and external disturbances, the effects of isolated rough structures are considerably better understood than the influence of distributed surface roughness. Even after almost a century of study on distributed roughness, there is still much unknown about the effects in various flow applications. The well behaved and relatively understood vortex structures seen in the presence of isolated 3-D roughness vanish under the influence of multiple clustered roughness elements.

The study of distributed roughness began with the work of Nikuradse [50] in 1933 and continued shortly thereafter with the extension of roughness correlations by Schlichtling [17]. The primary focus of the early experiments was not to study the influence of roughness on transition, or to provide a detailed analysis of the surrounding flow field, but to study the practical friction factor increases in pipe flows. After a quiet period, the influence of distributed roughness on external flows sparked the interest of the scientific community around World War II. Aircraft design played a dominant role and the study of scaling and similarity became necessary to determine the effects of roughness at higher flight speeds [45, 28]. Dryden [39], Braslow and Knox [51] all contributed significantly to the early era of roughness investigations. Much of their early work attempted to identify the critical height necessary to trip the flow under given conditions, and despite changes in the shape of the individual roughness elements $Re_{k,cr}$ remained constant at a value of approximately 600.

Three characteristics have been identified as having a significant influence (by no means do they provide a comprehensive list) on the overall effects of distributed roughness.

1. Streamwise Location

The streamwise location with respect to the leading edge of a flat plate or stagnation point of an airfoil must be considered due to the growing boundary layer, and localized pressure gradients. Roughness patches located near the onset of the boundary layer have a much larger effect on the flow due to the thin but high momentum portion of the boundary layer. The ratio of roughness height to displacement thickness (k/δ^*) rises due to the relatively small value of δ^*, along with Re_k as U_k also increases. This emphasizes the impact of icing on aircraft performance and leading edge erosion on various airfoil applications. In addition, the pressure gradients developed on a lifting surface are known to play a vital role in the flow disturbance introduced by the rough elements, further adding to the importance of the relative location.

2. Roughness Density

A second factor that must be considered is the density of the roughness structures. Microscopically, roughness elements close together can impact each other and hinder the growth of the horseshoe vorticies observed with isolated 3-D roughness. To a certain extent, this can damp out the perturbations introduced by each individual element, and it has been observed that a decrease in $Re_{k,cr}$ is seen for tighter packed rough sections. Gartshore and de Croos studied this phenomena and noted that a spacing of roughly $3k$ was the critical distance for which the clustering effect began, and the effective height of the roughness decreases for smaller spacings [52]. If the individual rough structures were further apart, the downstream flow had recovered enough to be fully influenced by the roughness elements. Additionally, von Doenhoff and Braslow discovered a similar increase in $Re_{k,cr}$ for tightly clustered roughness elements. An altering of $Re_{k,cr}$ has also been observed if the roughness elements are sparse and begin to resemble isolated roughness. There has been some progress attempting to quantify how roughness density will alter transition characteristics by Bons [1], Stripf et al. [53], and Elsner and Warzecha [54]. The general consensus is that the roughness has the most impact at a certain density, whereby an increase, or decrease in density will result in the lowering of the influence of the roughness.

3. Height Distribution

Frequently distributed roughness is modeled with uniformly sized particles packed together to create a rough section. An inherent issues is the assumption that surface roughness follows a constant size and pattern. In realistic applications this is frequently known to be false. It has been reported that the size of the largest elements dominates the effects of the smaller protuberances. Therefore, an attempt to recreate a realistic roughness pattern by taking the RMS value of roughness heights may not adequately represent the effects observed. This is of particular interest in analytical spectral methods as a particular wavenumber must be constantly amplified to simulate a rough surface. This has the unfortunate consequence of only adequately representing very uniform roughness configurations where the disturbances introduced can be easily quantified and represented with the amplification of a certain frequency in Fourier space.

One of the first studies that attempted to detail the effects of distributed roughness on the transition process was Feindt in 1956 [55]. By using various roughness heights across the length of a flat plate, he determined the effect of changing the roughness Reynolds number on the transition onset location. From here he was able to correlate a Re_{ks} to Re_{xt} (Reynolds number of transition onset) for various pressure gradients. Additionally, the study documented that for flow over a surface with an $Re_k < 120$, the roughness does not influence the location of transition. Walls contaminated with roughness below this minimum are regarded as "hydraulically smooth". This value has since been proven to not be universal and is used as a rough estimate rather than a hard limit. Morkovin has more recently suggested a threshold of $Re_k < 25$ for a surface to remain hydraulically smooth [18].

A study by Levanthal provided more insight in determining the effects of distributed roughness with Re_k values of 10 and 150 [56]. At the lower $Re_k = 10$ value, the boundary layer profiles observed were Blasius in shape and the mean profile remained unaffected. At the higher $Re_k = 150$ value, the mean profile was observed to be Blasius in shape for the initial laminar portion of the boundary layer with the exception that it was shifted upwards. Additionally, the amplification rate of the initial disturbances was found to be three times larger than the equivalent smooth TS waves. The frequencies that were amplified under the influence of distributed roughness were all below that of the natural TS frequencies, indicating that the mechanism that influenced transition was markedly different than an isolated roughness element at $Re_k = 300$. A study by Kendall further confirmed the existence of an outwardly displaced Blasius profile in the intermediate range of Re_k [40]. Additionally, Kendall reported an inflection in the velocity profile, that he attributed to the vertical transfer of streamwise momentum caused by the shape of the roughness elements. An inflection

in the profile is a significant observation as it is known to be a powerful amplifier of TS waves from inviscid stability analysis [10].

Following the investigation by Kendall, an experiment conducted by Corke, Bar-Sever, and Morkovin utilized randomized grit type roughness in hopes of finding amplified TS waves [38]. The investigators were also careful taking measurements near the top of the roughness to try and observe an inflection similar to what was seen by Kendall. Once again, no disturbances in the natural TS band were found, and despite the increased focus, no inflection in the mean profile was observed. It was further speculated the reason for the inflection in Kendall's experiment was the uniform shape and distribution of the roughness elements that promoted the vertical transfer of streamwise momentum. In the study of Corke et al., the receptivity of the roughness influenced boundary layer to external disturbances was also examined. It was postulated that the low inertia fluid below the top of the roughness increased the susceptibility of the fluid to freestream disturbances. The discrepancies in the results from the two experiments exemplify the nature of many distributed roughness studies as inconsistencies are frequently seen, and limitations in measurement techniques often limit further explanations.

Moving on to more complex geometries, much of the work aims once more to quantify the effect of roughness on practical performance quantities, such as lift and drag. For airfoil applications, the effects of icing has motivated a large amount of work, and especially in the earlier years of the study of roughness, many experiments did not detail the effects of the roughness on the transition process. A case study that did provide a detailed account of a boundary layer development along the surface of an airfoil with large scale leading edge erosion was performed by Kerho [2, 57]. The experiment provided a number of insights regarding the nature of roughness induced transitional boundary layers and the influence of Reynolds number on roughness effects. The study confirmed the importance of streamwise location as a primary factor influencing the effects of various distributed roughness patterns on boundary layer development. The results from this study are used as benchmark calibration runs in the current work as very detailed boundary layer profiles and turbulence variables were recorded.

Although a large portion of the work on the influence of surface roughness was through experimentation, analytical attempts have slowly progressed through the years. A few noteworthy early analytical studies attempting to describe the influence of surface roughness were conducted by Singh and Lumley [58] as well as Lessen and Gangwani [59]. Both studies took a spectral route and amplified specific Fourier components to represent the influence of roughness. In both studies an inflection was observed above rough sections. This result provides insight into the nature of these spectral amplification methods and the inherent limitations. The only experimental study that found an inflection in the mean profile was that of Kendal [40], and the uniform spherical roughness pattern used was supposed as the cause of the inflection. As this phenomena was only observed when using very specific homogenous roughness distributions it is not hard to see that applying a similar spectral approach to realistic non-uniform roughness may not adequately represent the configuration. The analytical approaches inherently produce uniform redistributions and transport of momentum, producing solutions that do alter the mean profile, but can lack the ability to represent unsteady effects and modifications to turbulent properties.

While the use of a critical roughness Reynolds number has proven as a useful criteria for determining if a rough element will cause the flow to transition, the less dominant effects of subcritical roughness ($Re_k < Re_{k,cr}$) are frequently excluded from computations. The lack of theoretical framework, difficulty measuring these more subtle effects, and high sensitivity to freestream disturbances all contribute to the general shortage of understanding regarding subcritical behavior. It was frequently observed that after encountering a rough section, the flow would remain laminar for sometime before transitioning. Morkovin referred to the period of laminar disturbance evolution as the incubation distance [18]. In general the flow

over subcritical roughness will transition earlier than an equivalent smooth surface. Despite this observation, it proved to be exceptionally difficult to create an analytical method to determine exactly how far the roughness would shift the transition location. An emerging theory to describe the path to transition generated by intermediate roughness heights is that of transient growth. The theory provides a well suited mathematical foundation as it is focused on spatially stationary perturbations that can effect the stability of the OS equation [42]. An experiment conducted by Ergin and White found evidence of transient growth caused by an isolated 3-D rough feature [42]. Furthermore, the theory has seen recent growth as applied to distributed roughness as well by Downs and White [60] . More information regarding transient growth can be found in [61, 62].

Distributed Roughness Summary

Although a large body of work has been developed on the influence of distributed roughness on the flow over a contaminated surface, the exact mechanism by which the roughness alters transition characteristics remains unknown. Several conjectures have been made as to how distributed roughness promotes the transition process. These include streamwise vortex structures produced in a similar manor to isolated 3-D elements, increased receptivity of the low inertia fluid in between the rough elements, and vertical transfer of streamwise momentum altering the mean profile. Despite challenges in identifying exact mechanisms by which the transition process is accelerated, there has been progress in identifying correlations that represent the aggregate effects of the roughness on flow properties. Through the use of a roughness Reynolds number, Re_k, the criteria for which the flow will not be altered or immediately transition can be determined. Slight progress has been made, but the intermediate range above the hydraulically smooth limit and below the critical onset value remains deeply misunderstood, and an active area of research.

Roughness Modeling

Presently and in the past, most roughness models are fundamentally correlation based. Much of the work on roughness modeling centers around identifying an equivalent sand grain roughness height, k_s, and then applying the respective correlation. A prominent issue is that often it is not straight forward to measure the exact diameter of the roughness, or other characteristics that influence how the roughness effects the flow. Several attempts have been made to correlate measurable parameters to an "equivalent" sand grain roughness heights. A review conducted by Bons [1] provides the details of many efforts to create an equivalent k_s value given certain measurable parameters. Other studies conducted concerning the modeling and parameterizing of roughness have been conducted by van Rij et al. [63] and Zhang et al. [64].

Computationally, attempts at roughness modeling can be broadly categorized into three distinct groups: (1) Modifying the turbulent eddy viscosity near wall in accordance to the relative height of the roughness. (2) Modify the governing flow equations directly to account for blockage effects and momentum loss due to increased drag. (3) Discretely model the rough features using an ultra fine near wall mesh. Due to the impractically high grid generation and computational costs, the option of discretely modeling the roughness is rarely taken [1]. Adding terms to the governing equations to account for the macroscopic physical behavior does have advantages; however, small miscalculations can severely effect the accuracy of the flow solution [53]. Modifying near wall turbulent behavior by adjusting parameters in the turbulence model is a popular approach and several strategies have been implemented by Durbin [23] and Hellsten and Laine [65]. These include modifying the boundary conditions for the turbulence dissipation rate and the subsequent

computation of the turbulent eddy viscosity, or directly modifying the one equation Spalart-Allmaras model [66].

While the modifications to the turbulence model boundary conditions can adjust the mean profiles once the boundary layer has fully transitioned, the acceleration of the transition process requires additional considerations. As there are many different methods implemented attempting to predict the onset of transition, the manner by which each are changed to accommodate surface roughness also differs greatly. Modifications to the linear stability based e^N method can be made by adjusting the N factor; however the correlation is far from universal and the method itself suffers from incompatibilities with implementation in parallel codes [27]. It is troublesome to modify other disturbance growth rate prediction methods to account for roughness for similar reasons, as the roughness induced perturbations bypass the linear growth of the disturbances.

A number of studies performed at Case Western Reserve University and Texas A&M University by White et al. have focused on using the theory of transient growth to determine the effects of roughness on the receptivity to external disturbances [67]. During a natural TS dominated transition, the growth of disturbances is dominated by the discrete eigenmodes of the Orr-Sommerfeld (OS) equation. However, under the influence of surface roughness the entire spectrum of the equation must be considered [60]. This method, referred to as continuous spectrum analysis, can theoretically predict the interaction of the normally decaying modes of the OS equation that are amplified due to the presence of disturbances introduced by surface roughness. This continuous spectrum method has been successfully implemented on a flat plate geometry, however, an extension to more complex configurations has yet to be robustly achieved [67].

As local correlation transition models (LCTM) have shown promise in implementation in general purpose CFD codes, it follows to try and modify the transition correlation to account for the presence of surface roughness. Recently, several attempts at modeling the influence of surface roughness have sought to incorporate roughness correlations into LCTM's. Notably, Stripf et al. [53] and Elsner and Warzecha [54] both proposed a direct modification of the transition onset criteria based on roughness height and displacement thickness (δ^*). This unfortunately introduces a necessary integral computation making the method non-local. Despite the unfavorable characteristics, the results from the experiments provide more insight into how roughness will alter the transition correlations used in LCTMs.

A similar approach to modeling roughness taken by Dassler, Koluvic, and Fiala was to introduce a field quantity governed by an additional transport equation that defines a region of roughness influence. The scalar field is then used to modify the transition onset criteria [68, 69]. This approach is taken in the current work due to the generalizable nature of local correlation modeling, and its inherent ability to predict by-pass transitions in RANS simulations. The details of the amplification of the initial roughness induced instabilities are not included in the methodology; however, the holistic effects of transition are represented well. The formulation of the roughness amplification variable becomes an issue of modifying the transition onset correlation, a much simpler problem than representing the increased disturbance growth rates. With proper calibration, subcritical roughness behavior can be represented and incubation period determined using a number of different parameters. By not directly modifying the primary flow equations the chances for error in the final flow solution become much lower. As the method does not require redefining the computational mesh, it can be applied to existing grids. Finally, many of the cited influential parameters (streamwise location, pressure gradient, etc.) can be included through coupling with a local correlation transition model.

Chapter 3

Governing Equations

Navier Stokes

The development of the governing equations has a rich historical background littered with the name's of some of the most influential mathematicians and scientists of all time. The Navier-Stokes equations were originally derived by Navier in 1822 however he made a few incorrect assumptions about the nature of the viscous forces [70]. The equations were re-derived by Cauchy and Poisson in 1828 and 1829 respectively [71]. The full equation set was also independently derived by Saint-Venant in 1843 and Stokes in 1845 with a more accurate consideration of the effect of viscosity [72]. Only the most fundamental information is given here, however there are countless references that detail the development and subsequent work on the equations that span a number of different fields. Frequently the Navier-Stokes (NS) and mass conservation equations are presented together and can be expressed quite elegantly in vector notation:

$$\rho(\mathbf{u_t} + \mathbf{u} \cdot \nabla \mathbf{u}) = \nabla \cdot \boldsymbol{\sigma} + \mathbf{f} \tag{3.1}$$

$$\rho_t + \nabla \cdot (\rho \mathbf{u}) = \mathbf{0} \tag{3.2}$$

Here the velocity field is given by $\mathbf{u}(\mathbf{x}, t) = u_j(x_1, x_2, x_3, t)$, $(j = 1, 2, 3)$, where $u_{1,2,3}$ represent the measure of velocity in each direction of a three dimensional orthogonal basis. The subscript t implies a partial derivative with respect to time. The right side of the equation represents the resultant body force, $\mathbf{f}$, on the domain and the internal force tensor $\boldsymbol{\sigma}$. The ∇ operator is defined by $\nabla = \sum_{j=1}^{N} \frac{\partial}{\partial x_j}$.

There are a number of ways to arrive at these equations, the most common is by examining the fluid as a continuum and applying the laws of classical mechanics. However the equations can also be derived by taking spatial averages of the Boltzmann equation, or from the kinetic theory of gasses. Equation 3.1 represents the laws of conservation of momentum applied to an element of fluid, and is referred to as the NS momentum equation. Equation 3.2 is referred to as the continuity or mass conservation equation and follows from fundamental mass conservation principles.

A third equation must be included in the set to account for thermodynamic properties and energy and is referred to as the energy equation. It is often presented separately from the mass and momentum conservation equations, as it decouples in the incompressible case. The energy equation is expressed:

$$\rho(e_t + \mathbf{u} \cdot \nabla e) = -p(\nabla \cdot \mathbf{u}) + \boldsymbol{\tau} \nabla \mathbf{u} + \nabla \cdot (\kappa \nabla T) \tag{3.3}$$

where e is the internal energy per unit mass, $\boldsymbol{\tau}$ is the viscous stress tensor (discussed below), κ the thermal diffusivity, and T temperature. In this regard the right most term can be thought of as the heat flux. Although

the full conservation equation set (momentum, mass, and energy) must be considered to fully represent various flows, the momentum equation is frequently singled out and studied more extensively.

The internal forces, $\boldsymbol{\sigma}$, can be regarded as the combination of the normal, or pressure forces, and the shearing or viscous stresses. One can consider the pressure terms as the diagonals of $\boldsymbol{\sigma}$ and all other components the viscous stress tensor ($\boldsymbol{\tau}$), such that:

$$\boldsymbol{\tau} = \boldsymbol{\sigma} - p\mathbb{I} \tag{3.4}$$

Where $p(\mathbf{x},t)$ represents the dynamic pressure distribution. In the case of an inviscid fluid, all but the pressure terms vanish, therefore $\boldsymbol{\sigma} = p\mathbb{I}$, and 3.1 simplifies to the Euler momentum equation:

$$\rho(\mathbf{u_t} + \mathbf{u} \cdot \nabla \mathbf{u}) + \nabla p = \mathbf{f} \tag{3.5}$$

The Euler equation has provided deep insight into the nature of high Reynolds number flows where the off-body flow behavior is dominated by the inertial terms and can be approximated by an inviscid assumption. Potential flow theory originated from the incompressible inviscid continuity equation and has remained a powerful analytical tool. However, for fluid-solid interfaces where boundary layers develop, the viscous stresses influence the problem substantially.

An approximation relating the strain on an element of fluid to its deformation ($\frac{1}{2}(\nabla \mathbf{u} + \nabla \mathbf{u^T})$) must be made to close the equation for the elements of the viscous stress tensor. If a linear approximation is taken where the fluid is assumed to deform proportional to the rate of strain, it is referred to as a Newtonian fluid. The internal tensor can be expressed as:

$$\boldsymbol{\sigma} = -p + \mu(\nabla \mathbf{u} + \nabla \mathbf{u^T}) + \left(\zeta - \frac{2\mu}{3}\right)(\nabla \cdot \mathbf{u})\mathbb{I}$$

Here ζ and μ are the first and second viscosities of the fluid. Inserting into 3.1 provides a more detailed description:

$$\rho(\mathbf{u_t} + \mathbf{u} \cdot \nabla \mathbf{u}) + \nabla p - \nabla \cdot \left[\mu(\nabla \mathbf{u} + \nabla \mathbf{u^T}) + \left(\zeta - \frac{2\mu}{3}\right)(\nabla \cdot \mathbf{u})\mathbb{I}\right] + \mathbf{f}$$

The equation further simplifies assuming μ to be constant and incompressibility to:

$$\rho(\mathbf{u_t} + \mathbf{u} \cdot \nabla \mathbf{u}) + \nabla p - \mu \Delta \mathbf{u} = \mathbf{f} \tag{3.6}$$

Where Δ is the Laplacian given by $\Delta = \sum_{j=1}^{N} \frac{\partial^2}{\partial x_j^2}$. Assuming ρ to be constant and given the definition of Reynolds number ($Re = \rho U L / \mu$), the equation can be recast in dimensionless form as:

$$\mathbf{u_t} + \mathbf{u} \cdot \nabla \mathbf{u} + \nabla p - \frac{1}{Re} \Delta \mathbf{u} = \mathbf{f} \tag{3.7}$$

In this form it is easy to see that as $Re \rightarrow \infty$, Equation 3.7 $\rightarrow$ Equation 3.5. At first glance this appears to simplify the equation substantially, however, the rate of convergence is troublesome as the $\Delta \mathbf{u}$ term does not follow the same rate of rapid decrease. Therefore, even when resolving high Reynolds number flows, the viscous term cannot be excluded.

Despite almost two centuries of work since the equations were first supposed, there is no general analytical solutions to the full conservation equation set. In very specific cases where the equations can be significantly reduced, such as laminar pipe flow, analytical solutions have been obtained [73]. Despite the difficulty in obtaining a closed form solution, the equations still provide an enormous insight into flow phenomena and various avenues have been developed to utilize various simplifications of the equations. Numerical simulations have helped obtain approximate solutions for a given flow configuration, and as both processing power increases and more efficient algorithms are developed numerical methods become more accurate.

DNS and Large Eddy Simulations

DNS

The full conservation equation set contains all forces and governing dynamics associated with a fully turbulent flow, the temporal behavior, large discrepancies in eddy scales, energy cascade, self dissipative nature and more. Direct numerical simulation (DNS) refers to the method by which the equations are directly solved numerically. The equations may be discretized directly or solved using a spectral method. The theoretical process itself is not troublesome, however, a necessary condition for the accuracy of DNS is that all time and spacial scales associated with a turbulent flow must be resolved [74]. To accomplish this, the computational mesh required becomes unpractically large. As a general guideline DNS is considered to require $O(Re^3)$ mesh points for proper resolution. A few representative configurations are listed.

Automobile – $Re \approx 6 \cdot 10^5 \rightarrow \approx 10^{15}$ mesh points required for DNS simulation.

Wind Turbine – $Re \approx 4 \cdot 10^6 \rightarrow \approx 10^{19}$ mesh points required for DNS simulation.

Large Airplane – $Re \approx 2 \cdot 10^7 \rightarrow \approx 10^{21}$ mesh points required for DNS simulation.

Clearly, the processing power required to handle that magnitude of points is entirely out of reach. Even with the most powerful supercomputers today, DNS can only be applied to flows around simple geometries at relatively low Reynolds numbers. Furthermore, even if there existed a machine capable of managing a problem of the size high Reynolds number DNS requires, complications would arise defining precise boundary conditions at each boundary node. As the full range of scales are represented, small discrepancies in the initial and boundary conditions may yield dramatically different solutions. Despite the limitations, DNS serves as a powerful validation tool and can provide detailed flow information that experimental techniques can not measure. Even with advances in processing capabilities and more efficient numerical algorithms, the use of direct numerical simulations for everyday engineering applications is still in the distant future.

Large Eddy Simulation

The most challenging motions to capture in DNS simulations are the smallest both spatially and temporally down to nearly the molecular level. Capturing these microscopic scales is the exact reason the mesh requirements are so impractical. An inclination is to define a length scale in which fluid motions below have very little influence on the macroscopic flow. This is the central idea behind Large Eddy Simulations (LES); modify the primary equations to not directly depend on the smallest scales and the mesh resolution required drops substantially. This is accomplished by defining a decomposition of the turbulent flow variables as:

$$\mathbf{u}(\mathbf{x},t) = \tilde{\mathbf{u}}(\mathbf{x},t) + \mathbf{u}''(\mathbf{x},t) \tag{3.8}$$

where $\tilde{\mathbf{u}}$ is the LES averaged portion of the variable and $\mathbf{u}''$ (a double prime is used to distinguish between a spatially and time averaged quantity) is the turbulent fluctuation defined based on the deviations from the averaged value. It is possible to directly average the flow variable over a cell volume, but the grid requirements to accomplish this are inhibitive, i.e. very uniform and structured. A more utilized option to accomplish the spatial average is to apply a filter kernel via convolution on the decomposed flow variables. Given a filter $g(\mathbf{x})$ and a length scale $\delta > 0$ as the minimum eddy size the filter takes the form:

$$g_\delta(\mathbf{x}) = \frac{1}{\delta^d} f\left(\frac{\mathbf{x}}{\delta}\right) \tag{3.9}$$

where d is an exponent that depends on the filter choice. For example a typical Gaussian filter can be expressed:

$$g_\delta = \left(\frac{\gamma}{\pi}\right)^{3/2} \frac{1}{\delta^3} e^{-\gamma \frac{|\mathbf{x}|^2}{\delta^2}} \tag{3.10}$$

where γ is a constant parameter. With the filter defined, $\tilde{\mathbf{u}}(\mathbf{x},t)$ becomes:

$$\tilde{\mathbf{u}}(\mathbf{x},t) := (g_\delta * \mathbf{u})(\mathbf{x},t) = \int_\Omega g_\delta(\mathbf{x} - \mathbf{s})\mathbf{u}(\mathbf{s},t)\, d\mathbf{s} \tag{3.11}$$

After applying the filter, LES sets out to model the influence of the removed energy scales. The modeling of the removed scales is known as closure or turbulence modeling and is discussed in more depth in the section on the Reynolds-averaged equations. A few of the more commonly used sub grid models are the Smagorinsky and Gaussian-Laplacian [75]. As a consequence of the definition, as $\delta \to 0$, so does $\mathbf{u}''$ and furthermore $\tilde{\mathbf{u}}(\mathbf{x},t) \to \mathbf{u}(\mathbf{x},t)$. This is even more substantial if one realizes that it implies LES $\to$ DNS.

For those interested in the mathematical details of LES, Berselli et al. provide an excellent account of the primary LES tools available [75].

Despite the simplifications introduced, the grid required to properly resolve an LES problem is still enormously large. Additionally, assumptions have to be made regarding the nature of wall bounded flows, as the spatial filter encounters trouble approaching a solid boundary. As the distance to the wall goes to zero, what does one do with the δ limit? Other issue arise as certain required filter operations do not commute at wall boundaries. LES will likely serve as stepping stone to full DNS simulations, however the process still

has a few theoretical shortcomings and requires vastly more computing power than is practical for everyday use.

Reynolds-Averaged Navier Stokes Equations

A very distinguishing characteristic of turbulence is its *unsteady* nature, eddies of all sizes are created and dissipated continuously, the mean flow might have a well defined direction but with in the stream lie boundless fluctuations. An approach to eliminate the temporal behavior is to look at the flow as a combination of both a time averaged flow and a fluctuating component, similar to the LES decomposition. Given a finite time interval, there is a well defined average velocity at a particular location in the flow field, from there the instantaneous deviations from the mean can be defined as the turbulent fluctuations. Frequently the following notation is used:

$$\mathbf{u}(\mathbf{x}, t) = \bar{\mathbf{u}}(\mathbf{x}) + \mathbf{u}'(\mathbf{x}, t) \tag{3.12}$$

Here the mean flow is represented with an overbar and defined as $\bar{u} = \frac{1}{T} \int_0^T u(t)\, dt$. The prime indicates the fluctuating component. An important consideration is that the RANS mean velocity does not carry a time dependence, unlike the LES counterpart. For reference, the turbulent decomposition actually began with the definition in a time averaged sense and was later progressed to the spatial variant.
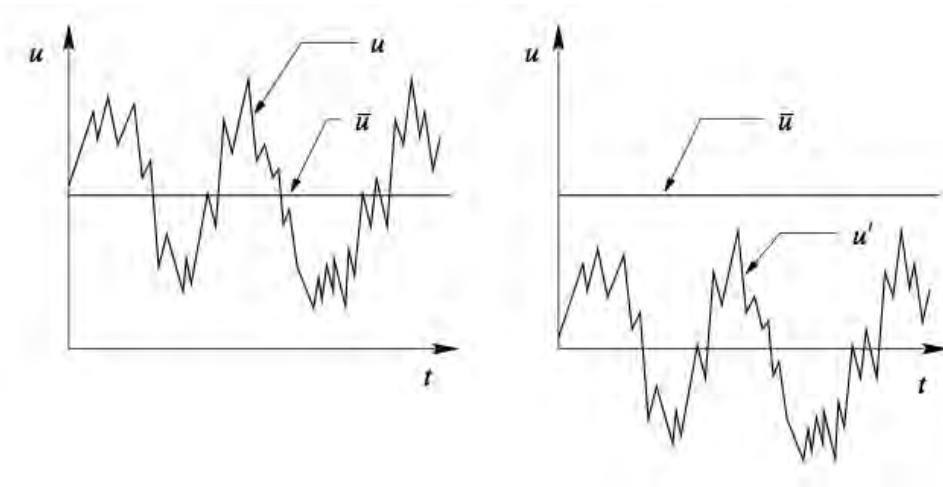
Figure 3.1. Plot of Reynolds decomposition indicating mean flow and fluctuating component

Osborn Reynolds is credited as the first to exploit the fact that without a time dependence the governing flow equations are simplified greatly. In addition, two properties of the decomposition are the following.

$$\bar{\bar{u}} = \frac{1}{T} \int_0^T \bar{u}\, dt = \bar{u} \quad \& \quad \overline{u'} = \frac{1}{T} \int_0^T u'(t)\, dt = 0 \tag{3.13}$$

The first follows as the time average of a time averaged quantity remains the same, additionally the time average of the fluctuating component goes to zero by definition.

The Reynolds-averaged Navier Stokes equations are obtained by inserting the Reynolds decomposed flow variables into 3.1 and 3.2 and time averaging the entire equations. The full derivation is omitted, however the final result as applied to the momentum equation can be written generally as:

$$\nabla \cdot \overline{\mathbf{u}}^2 + \nabla \cdot \overline{\mathbf{u}'^2} = \nu \Delta \overline{\mathbf{u}} - \nabla \overline{\mathbf{p}} \tag{3.14}$$

Reynolds-stress Term

There is an inherent problem that arises during the averaging process, that is the time average of the product of two fluctuating components does not go to zero.

$$\overline{u_i' u_j'} \neq 0 \quad (i, j = 1, 2, 3) \tag{3.15}$$

Therefore, the term $\nabla \cdot \overline{\mathbf{u}'^2}$ needs additional consideration. The quantity is referred to as the Reynolds-stress term. Traditionally, the RANS equations and complimentary turbulence models are expressed in tensor or Einstein summation notation. The subscript indices correspond to the directions in a generalized orthogonal basis and are used to differentiate scalars, vectors, and tensors. The relationship between vector and tensor notation can been observed in the following:

$$\nabla \cdot \overline{\mathbf{u}'^2} = \nabla \cdot \begin{bmatrix} \overline{u_1' u_1'} & \overline{u_1' u_2'} & \overline{u_1' u_3'} \\ \overline{u_2' u_1'} & \overline{u_2' u_2'} & \overline{u_2' u_3'} \\ \overline{u_3' u_1'} & \overline{u_3' u_2'} & \overline{u_3' u_3'} \end{bmatrix} = \nabla \cdot \overline{u_i' u_j'} = \frac{\partial}{\partial x_j} \overline{u_i' u_j'} \tag{3.16}$$

In tensor notation 3.14 can be written:

$$\frac{\partial}{\partial x_j} \overline{u}_i \overline{u}_j = -\frac{\partial \overline{p}}{\partial x_i} + \nu \frac{\partial^2 \overline{u}_i}{\partial x_j \partial x_j} - \frac{\partial}{\partial x_j} \overline{u_i' u_j'} \tag{3.17}$$

All terms are dependent on mean quantities with the exception of the Reynolds-stresses term. This posses a problem when trying to resolve the RANS equations as more unknowns are created than equations available.

Turbulence Modeling

The practice of creating a model to account for the Reynolds stress term is known as closure, or turbulence modeling. Turbulence modeling has been the subject of extensive scientific investigation over the past half century. To conduct a thorough review of all the research conducted, even if only the most significant contributions are discussed would require considerably more space than available here. With this in mind only the most fundamental details are provided. The reader is directed to Wilcox for a more complete examination of turbulence modeling [76]. It should also be stressed that most turbulence models are based on

34

extensive numerical investigations and are not derived from first principles. Regardless, turbulence modeling has made significant progress and RANS simulations have proven to accurately represent a wide variety of flows.

The primary approximation used in the process of modeling the Reynolds stresses was originally proposed by Boussinesq in 1877. He supposed the turbulent shearing is related to the mean rate of shear of turbulent and eddy viscosity. The approximation is frequently referred to as the Boussinesq hypothesis. Closure methods that depend on it are titled eddy-viscosity models, due to the inclusion of the additional term, ν_t. It relates the Reynolds-stress term to the mean rates of shear and is given by:

$$-\overline{u_i' u_j'} = \nu_t \left(\frac{\partial \overline{u}_i}{\partial x_j} + \frac{\partial \overline{u}_j}{\partial x_i} \right) - \frac{2}{3} \delta_{ij} \left(\nu_t \frac{\partial \overline{u}_k}{\partial x_k} + k \right) \tag{3.18}$$

with δ_{ij} is the Kronecker delta function, k is the turbulent kinetic energy given by $k = \frac{1}{2}(u_i'^2)$ and ν_t is the turbulent eddy viscosity, which is an additional quantity that needs modeling for proper RANS closure. Much like the molecular viscosity and kinematic viscosity are related, there is the relationship $\nu_t = \mu_t/\rho$. Methods for modeling ν_t can be characterized by their order of closure. The order of the method is given by the number of additional partial differential equations used in determining the approximation of turbulent eddy viscosity.

Zero and First Order Models

Zero order closure models are based off the Boussinesq approximation that do not use any additional PDE's and that compute the turbulent eddy viscosity using an algebraic expression based on local flow quantities. One of the initial zero order methods was Prandtl's mixing length model, determined using dimensional analysis. It was first supposed in the 1920's with ν_t defined as:

$$\nu_t = l_m^2 \left| \frac{\partial u}{\partial y} \right| \tag{3.19}$$

From Eq. 3.19, one can see the turbulent eddy viscosity is proportional to the magnitude of the shear stress, $|\partial u/\partial y|$, and l_m, the mixing length that depends on the flow conditions and needs to be prescribed by the user. The mixing length is both a property of the fluid and of the local flow characteristics. This raises issues as the length scales at different regions in the boundary layer are markedly different. An approach to solve the problem of changing length scales is the implementation of the Van Driest damping function [77]:

$$l_m = \kappa y [1 - e^{-y^+/A_o^+}] \tag{3.20}$$

with y^+ the non-dimensional wall distance defined $(\sqrt{\tau_w/\rho_w})(y/\nu)$ and A_o^+ a model constant.

Similar approaches incorporating a damping function have been taken in LES to resolve the issue of the filter length as a solid boundary is approached [75].

Other zero order models have been developed by Smagorinsky, Baldwin and Lomax. Most modern simulations do not use algebraic correlations due to non-general nature of the parameters involved. Additionally

zero order models require the direct use of an empirical correlation. Transport equations are frequently used to incorporate the local flow conditions allowing the model to function without prescribing the type of flow in a region when initializing the simulation.

Models that use one additional transport equation in determining v_t are referred to as first order closure models. They have been developed by Baldwin and Barth [78], as well as Spalart and Allmaras [79]. The Spalart-Allmaras (SA) model represented a significant leap forward in the accuracy of turbulence modeling and, provided the flow remains attached, is still regarded as one of the more trusted approximations in RANS simulations [80, 81]. The SA model has been continually developed with iterations of the model released with rotational corrections and the use of a laminar-turbulent trip specification.

Concurrent to the development of the one equation turbulence models was the initial work attempting to incorporate the length scales associated with a turbulent flow directly into the computation of the turbulent eddy viscosity. The primary quantity of interest is the turbulent kinetic energy (k) and some form of the dissipation rate. Models that solve two additional quantities for the transport of the turbulent quantities are known as two equation models.

$k - \varepsilon$ and $k - \omega$ Two Equation Models

One of the initial two equation approaches incorporates the turbulent dissapation rate (ε) along with the turbulent kinetic energy into the formulation for v_t. Jones and Launder are credited as developing the $k - \varepsilon$ model which models the transport of turbulent kinetic energy and dissipation rate using transport equations [82]. The full development spans many different researchers and the model has evolved over the years. Much like the SA model, the $k - \varepsilon$ model has proven to behave well in attached flows however it has been cited with under predicting the effects of flow separation. Additionally, the near wall behavior is considered dubious and requires the use of wall damping function to better represent the near wall dynamics has become common practice. The turbulent eddy viscosity is then defined as the ratio between the turbulent kinetic energy and the dissipation rate as:

$$v_t = \frac{k}{\varepsilon} \tag{3.21}$$

A similar model to the $k - \varepsilon$ was developed by Wilcox [83]. Much like other two equation models, it uses the turbulent kinetic energy as one of the primary quantities of interest, however a slightly different scale is used for the dissipation parameter (ω). The $k - \omega$ turbulence model, as it is referred, is known to represent near wall flows much more accurately than the $k - \varepsilon$ and does not require the use of wall damping functions. The $k - \omega$ model also includes the influence of streamwise pressure gradient, an additional upgrade from the $k - \varepsilon$ formulation. The changes to the $k - \omega$ model when compared to the $k - \varepsilon$ are not all positive. The freestream condition for ω must be non-zero, something that is non-physical. Additionally, the choice of this freestream value is not universal and can have a strong impact on the flow solution [84]. The turbulent eddy viscosity is computed similarly with the exception of using ω rather than ε, $(v_t = k/\omega)$.

SST Two Equation Model

The strengths and weaknesses of the $k - \varepsilon$ and $k - \omega$ models naturally suggest the two be combined to create a model that can behave well both near wall and in the freestream. Mentor's shear-stress transport

(SST) model takes the advantages of both and creates a blending function that switches between the two [85]. The $k-\omega$ model is incorporated near a viscous wall that is switched over to the $k-\varepsilon$ near the boundary layer edge and free shear layer. The dissipation parameter is given the name "specific dissipation rate" and is labeled ω; therefore, when referring to the SST model, ω represents a blend of the turbulence dissipation scales from either model. The SST model is the underlining turbulence model that the present work looks to build upon, therefore more details will be given. The turbulent eddy viscosity is given in a similar manner to other two equation models as:

$$\nu_t = \frac{k/\omega}{\max\left[1 \; ; \; \frac{\Omega F_2}{a_1 \omega}\right]} \tag{3.22}$$

The F_2 function is determined by:

$$F_2 = \tanh\left(\left[\max\left(2\frac{\sqrt{k}}{0.09\omega y} \; ; \; \frac{500\mu}{\rho y^2 \omega}\right)\right]^2\right) \tag{3.23}$$

The transport equation for turbulent kinetic energy (k) and specific turbulent dissipation rate (ω) are as follows:

$$\frac{\partial(\rho k)}{\partial t} + \frac{\partial(\rho U_j k)}{\partial x_j} = P_k - \beta^* \rho \omega k + \frac{\partial}{\partial x_j}\left[(\sigma_k \mu_t + \mu)\frac{\partial k}{\partial x_j}\right] \tag{3.24}$$

$$\frac{\partial(\rho \omega)}{\partial t} + \frac{\partial(\rho U_j \omega)}{\partial x_j} = P_\omega - \beta \rho \omega^2 + 2(1 - F_1)\sigma_\omega \frac{\mu_t}{k}\frac{\partial k}{\partial x_j}\frac{\partial \omega}{\partial x_j} + \frac{\partial}{\partial x_j}\left[(\sigma_\omega \mu_t + \mu)\frac{\partial \omega}{\partial x_j}\right] \tag{3.25}$$

with the production terms (P_k, P_ω) defined:

$$P_k = \left(\mu_t\left[\left(\frac{\partial u_i}{\partial x_j} + \frac{\partial u_j}{\partial x_i}\right) - \frac{2}{3}\frac{\partial u_k}{\partial x_k}\delta_{ij}\right] - \frac{2}{3}\rho k \delta_{ij}\right)\frac{\partial u_i}{\partial x_j} \tag{3.26}$$

$$P_\omega = \frac{\zeta}{\nu_t}P_k \tag{3.27}$$

The F_1 term in Eq. 3.25 represents the primary blending function between the $k-\omega$ and the $k-\varepsilon$ models. It is designed to switch from the ω variant near the wall to the ε formulation in the far field. When the F_1 functions takes a value of one, the transport equation for ω transforms into the equation for ε. The function utilizes the smooth properties of the hyperbolic tangent function and is given by:

$$F_1 = \tanh\left(\left[\min\left\{\max\left(\frac{\sqrt{k}}{0.09\omega y} \; ; \; \frac{500\mu}{\rho y^2 \omega}\right) \; ; \; \frac{4\rho \sigma_{\omega 2} k}{CD_{k\omega} y^2}\right\}\right]^4\right) \tag{3.28}$$

$CD_{k\omega}$ is the cross diffusion term given by:

$$CD_{k\omega} = \max\left[\frac{2\rho\sigma_{\omega2}}{\omega}\frac{\partial k}{\partial x_j}\frac{\partial \omega}{\partial x_j} \; ; \; 10^{-20}\right] \tag{3.29}$$

The model constants are given by:

$$
\begin{aligned}
&a_1 = 0.31, \quad \kappa = 0.41, \quad \beta^* = 0.09 \\
&\sigma_{k1} = 0.85, \quad \sigma_{\omega1} = 0.5, \quad \beta_1 = 0.075 \\
&\sigma_{k2} = 1.0, \quad \sigma_{\omega2} = 0.856, \quad \beta_2 = 0.0828 \\
&\zeta_1 = 0.553, \quad \zeta_2 = 0.440
\end{aligned} \tag{3.30}
$$

In addition to switching the transport equation for ω, the model parameters are blended using the F_1 function by:

$$\phi = F_1\phi_1 + (1 - F_1)\phi_2 \tag{3.31}$$

where ϕ represents an arbitrary model constant and subscripts refer to that parameters value in each of the respective models. A constant that does not include an explicit subscript in the model description is blended in using Eq. 3.31.

The SST model has consistently outperformed either of its built in variants, particularly near separation and predicting near wall flow behavior. A primary issue is that it does not account for the laminar-turbulent transition region nor can it predict the location of the onset of transition. A partial fix was to incorporate a manually defined location to switch on the production of turbulent kinetic energy representing the position turbulent fluctuations initiate and the physical onset of t ransition. The trouble with using a manual specification is that a well defined location of transition onset must be known in advance, otherwise it is at best an educated guess. This shortcoming has been addressed by the development of transition models that are coupled with the turbulence model to better approximate the state of the boundary layer, and its subsequent effects on the surrounding flow fi eld. The topic of transition modeling is explored in much more detail in the next chapter as it is of great interest to the current study.

Local correlation transition modeling (LCTM) is briefly mentioned in the review of transition prediction methodologies and is worth noting the interaction it has with the SST turbulence model here. A widely used LCTM is referred to as the Langtry-Menter transition model. It couples a correlation based transition onset criteria with an intermittency (γ) transport equation. In the Langtry-Menter model, γ acts as a scaling of the production of turbulent kinetic energy, P_k.

The modified production term becomes:
$$\tilde{P}_k = \gamma P_k \tag{3.32}$$

The value of γ is pushed to zero by the model in the laminar boundary layer where there is no production of turbulent kinetic energy, and then progressively switches to one where the turbulence model is fully activated. To ensure the turbulence model functions properly globally, the value of intermittency is initialized to one in the entire domain, and reduced only in the laminar boundary layer. This is opposite to the usual experimental definition, where intermittency is assumed to be zero everywhere until the flow transitions.

Although this does switch on the turbulence model in the freestream, production of turbulent kinetic energy is inherently limited due to lack of shear stress in the mean flow.

Eddy Viscosity Alternatives

The modeling of Reynolds-stresses by means of the Boussinesq hypothesis is not the only method for representing the fluctuating products. Another approach is to model the transport of the Reynolds stress terms directly, and methods that employ this technique are known as Reynolds-stress transport models (RSTM) [86]. Frequently referred to as second order closure models, the use of these is inhibited by the significant computational costs associated with resolving the additional unknown quantities. The cost derives from the fact that five or more additional transport equations are required to use the second order closure models [87, 86].

A common critique of the approximation using an eddy-viscosity model is the assumption of isotropic turbulence at all scales. While this is generally assumed to be true for the smallest turbulent scales, the largest eddies do not behave isotropically. It can be observed from 3.16 that $\overline{u'_i u'_j}$ is a tensor, and therefore a constant value of ν_t does not account for differences in the transport of the Reynolds-stress terms in each direction. Closure models that treat ν_t as a tensor have been proposed; however, this requires each term of the tensor to be individually modeled adding even more equations [88].

Both RSTM's and the anisotropic modeling of the eddy viscosity are "physically" more accurate approximations, and one might expect that they produce more accurate solutions. This does not always prove true, because there are trade offs that come with the discretization error that compounds due to the additional model equations. It brings up the debate of what is more accurate, a more physically correct model that has a large modeling error, or a physically less accurate model with a much smaller modeling error. In the case of turbulence modeling, the more refined but less physically accurate models have generally won out [81].

Detached Eddy Simulation

A recently developed simulation technique is that of Detached Eddy Simulation (DES). Originally proposed in 1997 by Spalart et al., DES is hybrid method that includes both RANS and LES modeling approaches [89]. DES attempts to take advantages of the strengths of both methods by applying a RANS procedure in the near wall region and an LES off body. This helps resolve the issues of near wall behavior that LES has struggled with, including the grid resolution required and spacial filtering problems encountered at solid boundaries. Applying an LES approach in the far field is desirable to retain flow structures frequently smoothed away in RANS procedures. The non-physical smoothing of vorticity or other unsteady features has plagued RANS simulations due to fundamental consequences of time averaging. Proper vortical resolution can be obtained in RANS but requires carefully designed grids for complex geometries [90].

DES is very appealing theoretically, however in practice it has been reported the method displays unfavorable sensitivity to grid spacing, in some cases creating a solution less accurate than either a pure RANS or LES performed on the same grid [91]. Other more fundamental issue arise as the LES turbulent decomposition is not the same as in RANS, i.e. $\mathbf{u}' \neq \mathbf{u}''$ & $\tilde{\mathbf{u}} \neq \overline{\mathbf{u}}$ using the notation from above. DES is currently an active area of research and given its young age conceptually it will likely see improvements in the near future. Considering the near wall flow is modeled using a RANS approach, the present work is of great

interest as it can theoretically be included in DES in the future.

In terms of accuracy from the perspective of physically represented scales:

$$DNS > LES > DES > RANS$$

LES and DNS are still considered far away from practicality in an engineering sense so RANS and DES will likely remain prominent for some time. The implications of this are that a model capable of predicting the effects of roughness on near wall behavior with a RANS turbulence approach will continue to have use even if a shift is made in the engineering community towards DES simulations.

OVERFLOW-2

OVERFLOW-2 is finite difference, unsteady RANS code developed by NASA over the past few decades. The code was initially developed as a cleaner more robust version of the flux-vector splitting code F3D, originally developed by Joe Steger. Throughout its history the code has seen input from scientists across several NASA research centers including Ames, Johnson Space center, and Langley. Although a large number of researchers have contributed to the development of OVERFLOW a few that have made a significant impact include, Joe Steger, Pieter Buning, Dennis Jespersen, Tom Pulliam, Robert Meakin, and many more [92].

OVERFLOW-2 allows the user to select a wide variety of numerical spacial discretization and time advancement techniques of varying order of accuracy [93, 9]. Additionally, a number of linear factorization and flux splitting schemes are implemented for more efficient computation. The interaction the user has with the code is through an input file where the specified discretization schemes, boundary conditions, and many other flow parameters are set. When applicable the variable name is provided as (&*CATEGORY* < *VARIABLENAME*) to provide some indication of how the conditions are set within OVERFLOW-2.

Version 2g of OVERFLOW-2 contains an implementation of the Langtry-Menter transition model and is the platform upon which the current work is built. Many details of the code's development and capacity are left out as providing a comprehensive overview would require far more space than available. The reader is directed to [9, 92, 93] for further details pertaining to the development and features built into OVERFLOW-2.

Chapter 4

Langtry-Menter Transition Model

The concept of correlation based transition modeling was one of the first to be explored when the engineering community desired to include the effects of the laminar-turbulent transition region in calculations. In such models, freestream quantities such as turbulence intensity and pressure gradients are used to compute a critical flow quantity, usually some form of a momentum thickness Reynolds number ($Re_\theta = U_e \theta / \nu$), that is used to determine when transition onset occurs. The method is similar to linear disturbance growth approximations (e.g. van Ingen's e^N method [27]) as both require multiple steps, the computation of the laminar flow solution and the subsequent calculation of either the disturbance growth rate or Re_θ. From there, a search algorithm is performed whereby if the local $Re_\theta > Re_{\theta,onset}$, the transition process is triggered. The primary limitation in use of these models is the non-local operations required to integrate the growth rates or compute the momentum thickness of the boundary layer (including the definition of a boundary layer edge). Additionally, many of the concepts such as the linear growth of disturbances are inherently 2-D. To alleviate the problems posed in the implementation of previous methods Menter et al. presented a new class of transition model based on transport equations [36]. The original model was then iterated to its current version by Langtry with the following goals as to be compatible with general purpose CFD codes [37, 94]:

1. Robustly predict transition location by means of extensive experimental calibration

2. Include the ability to predict multiple modes of transition (natural, bypass, separation induced, etc.)

3. Only rely on local terms in computations to allow for use on parallel architecture and unstructured grids

4. Allow integration into underlying SST turbulence model without affecting the validity of a fully turbulent solution

5. Three-dimensional compatibility without additional consideration or modification

Model Principles

As a broad overview, the model combines an empirical correlation with an intermittency equation that acts as a progressive switch for the production of turbulent kinetic energy. At the core of the model lies the connection between Van Driest and Blumer's vorticity Reynolds number [15], empirical transition onset criteria [31], and local flow quantities [37]. The vorticity or likewise known strain-rate Reynolds number is defined:

$$Re_v = \frac{\rho y^2}{\mu}\left|\frac{\partial u}{\partial y}\right| = \frac{\rho y^2}{\mu}S \tag{4.1}$$

The vorticity Reynolds number is dependent on ρ, viscosity, μ, along with distance to the nearest wall, y. Although not an entirely local quantity the wall distance can be computed using a Poisson equation [37] when not directly available from the grid topology. In the transition model, Re_v is related to the momentum thickness Reynolds number (Re_θ) by the following:

$$Re_\theta = \frac{\max(Re_v)}{2.193} \tag{4.2}$$

The $\max(Re_v)$ corresponds to the maximum value the vorticity Reynolds number obtains in the plane normal to the surface. The constant 2.193 is calibrated such that for a Blasius profile $\max\{(2.193Re_\theta)/Re_v\} = 1$. The relative error (as compared to a Blasius profile) of this relationship between Re_v and Re_θ when considering laminar boundary layers of different shape factors remains on the order of less than 10% provided the pressure gradient does not become too adverse. When encountering an adverse pressure gradient, particularly near separation, the difference between the computed Re_θ based on Re_v and the actual momentum thickness spikes. However, this fact is used to help the model predict separation induced transition, something a purely momentum thickness based approach is unable to achieve.

Creating an expression for Re_θ as a function of Re_v localizes the computation of momentum thickness and eliminates the need to define a boundary layer edge. It can be observed that Re_v naturally obtains a maximum within the boundary layer due the quantities it is based on. If there are multiple walls in the vicinity, the max function can predict which surface causes the flow to destabilize first. In essence, this takes the momentum thickness, an inherently 2-D concept, and allows for three dimensional effects to be accounted for.

Having established a procedure to compute the local Re_θ without having to perform any integrations, the next step was to define the empirical correlation throughout the flow field to facilitate the comparison between the local Re_θ and $Re_{\theta,onset}$. The model defines the "transition onset momentum thickness Reynolds number" ($\tilde{Re}_{\theta t}$) to serve as the onset criteria. A transport equation is used to define the distribution of $\tilde{Re}_{\theta t}$ that is extensively calibrated with an empirical correlation based on freestream turbulence intensity (Tu) and streamwise pressure gradient. The onset criteria is coupled with a transport equation for intermittency (γ) which acts as a progressive switch for the production of turbulent kinetic energy, and therefore transition from laminar to turbulent flow.

Model Formulation

The transport equation defining the distribution of $\tilde{Re}_{\theta t}$ is given by:

$$\frac{\partial(\rho\tilde{Re}_{\theta t})}{\partial t} + \frac{\partial(\rho U_j\tilde{Re}_{\theta t})}{\partial x_j} = P_{\theta t} + \frac{\partial}{\partial x_j}\left[\sigma_{\theta t}\left(\mu+\mu_t\right)\frac{\partial\tilde{Re}_{\theta t}}{\partial x_j}\right] \tag{4.3}$$

The form is of a standard scalar convection-diffusion equation, where $\left(\partial(\rho U_j\tilde{Re}_{\theta t})/\partial x_j\right)$ serves as the

convective flux of$\tilde{R}e_{\theta t}$ while the right hand partial term corresponds to diffusive effects. The production term contains the empirical correlation, referred to as $P_{\theta t}$. The function is defined;

$$P_{\theta t} = c_{\theta t} \frac{\rho}{t} (Re_{\theta t} - \tilde{R}e_{\theta t})(1 - F_{\theta t}) \qquad (4.4)$$

$Re_{\theta t}$ is a direct computation of the correlation, while $\tilde{R}e_{\theta t}$ is determined purely by the transport equation to account for localized effects. By taking the difference between the two $(Re_{\theta t} - \tilde{R}e_{\theta t})$, the production term forces the local $\tilde{R}e_{\theta t}$ closer to the empirically computed value. $F_{\theta t}$ acts as a switching function to shut off the production in the boundary layer, while $c_{\theta t}$ is a model constant and t a time scale included for dimensional reasons. The full expressions for both $F_{\theta t}$ and $Re_{\theta t}$ are given by Langtry and Menter [37]. It should be emphasized that:

$$Re_{\theta t} = f(Tu, \lambda_\theta) \qquad (4.5)$$

where Tu is the freestream turbulence intensity, and λ_θ is the pressure gradient parameter. Figure 4.1 demonstrates the significant effect of Tu on $Re_{\theta t}$.
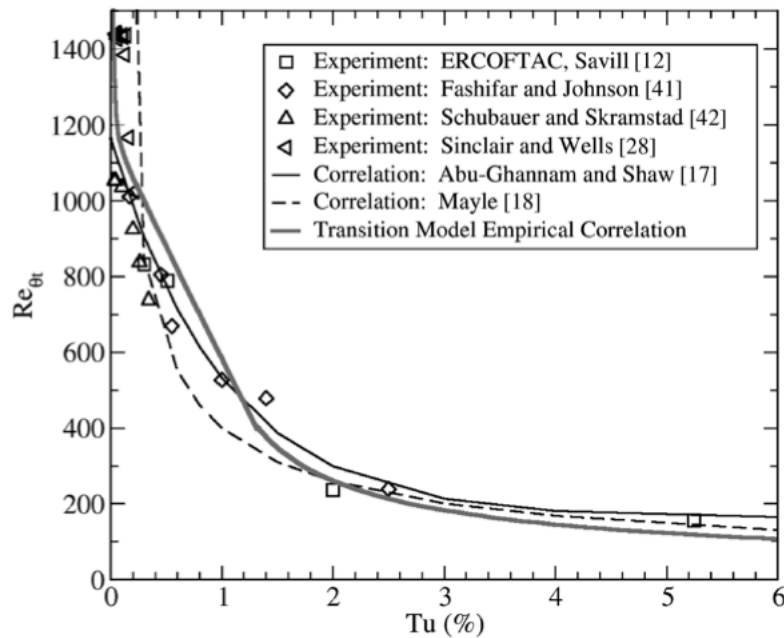

Figure 4.1. Plot of various empirical correlations demonstrating the effect of Tu on $Re_{\theta t}$ and how the Langtry-Menter model is related to other past experimental investigations, adapted from Langtry and Menter [37]

Tu and λ_θ are determined with the expressions:

43

$$\lambda_\theta = \frac{\rho \theta^2}{\mu} \frac{dU}{ds} \tag{4.6}$$

$$Tu = 100 \frac{\sqrt{2k/3}}{U} \quad \text{with} \quad k = \sqrt{u'^2 + v'^2 + w'^2} \tag{4.7}$$

The appearance of the momentum thickness, θ, in the pressure gradient parameter necessitates an iterative method to solve for $Re_{\theta t}$. The quantity $\frac{\rho}{\mu}$ acts to viscously dampen the influence of momentum thickness and dU/ds is the acceleration in the streamwise direction. U is the magnitude of the velocity ($U = \sqrt{u^2 + v^2 + w^2}$) and the derivative dU/ds is then computed:

$$\frac{dU}{ds} = \left[(u/U)\frac{dU}{dx} + (v/U)\frac{dU}{dy} + (w/U)\frac{dU}{dz} \right] \tag{4.8}$$

With dU/dx, dU/dy, dU/dz:

$$\frac{dU}{dx} = \frac{1}{\sqrt{(u^2+v^2+w^2)}} \cdot \left[u\frac{du}{dx} + v\frac{dv}{dx} + w\frac{dw}{dx} \right] \tag{4.9}$$

$$\frac{dU}{dy} = \frac{1}{\sqrt{(u^2+v^2+w^2)}} \cdot \left[u\frac{du}{dy} + v\frac{dv}{dy} + w\frac{dw}{dy} \right]$$

$$\frac{dU}{dz} = \frac{1}{\sqrt{(u^2+v^2+w^2)}} \cdot \left[u\frac{du}{dz} + v\frac{dv}{dz} + w\frac{dw}{dz} \right]$$

A slight weakness of the model is that the use of stream direction is not Galilean invariant, however this only poses an issue with multiple moving walls in close vicinity.

Once the distribution of $\tilde{Re}_{\theta t}$ is determined an intermediate value is computed referred to as the "critical momentum thickness Reynolds number", $Re_{\theta c}$. This parameter is a strong function of $\tilde{Re}_{\theta t}$:

$$Re_{\theta c} = f(\tilde{Re}_{\theta t}) \tag{4.10}$$

This parameter determines the value the vorticity Reynolds number must obtain to trigger intermittency (γ) production, thereby initiating the simulated transition process. The distribution of intermittency is governed by a second transport equation:

$$\frac{\partial(\rho\gamma)}{\partial t} + \frac{\partial(\rho U_j \gamma)}{\partial x_j} = P_\gamma - E_\gamma + \frac{\partial}{\partial x_j}\left[\left(\mu + \frac{\mu_t}{\sigma_f} \right) \frac{\partial\gamma}{\partial x_j} \right] \tag{4.11}$$

The value of intermittency in the freestream is set to one. This differs from the usual definition where an intermittency of one is reserved for a fully turbulent state. This is necessary to accurately account for freestream turbulence decay rates and to allow the SST turbulence model to function undisturbed outside the

44

laminar boundary layer. Additionally, even though it is not shut off directly using the intermittency variable, production of turbulent kinetic energy is limited in the freestream due to the lack of shearing stress in the mean flow.

The production term (P_γ) is given by:

$$P_\gamma = F_{length} c_{a1} \rho S [\gamma F_{onset}]^{.5} (1 - c_{e1} \gamma) \tag{4.12}$$

c_{e1} and c_{a1} are model constants and S is the magnitude of the strain rate. The function F_{onset} acts to compare Re_v and $Re_{\theta c}$, (i.e. $F_{onset} = f(Re_v, Re_{\theta c})$), while F_{length} is calibrated based on the ERCOFTAC [95] and the Schubauer and Klebanof [16] test cases such that:

$$F_{length} = f(\tilde{Re}_{\theta t}) \tag{4.13}$$

E_γ is included in the intermittency transport equation to account for the possibility of relaminarization under the influence of a highly favorable pressure gradient. The intermittency destruction/relaminarization source term is defined:

$$E_\gamma = c_{a2} \rho \Omega \gamma F_{turb} (c_{e2} \gamma - 1) \tag{4.14}$$

Once more c_{e2} and c_{a2} are model constants while Ω is the vorticity magnitude. F_{turb} switches off the destruction term outside the laminar boundary layer and within the viscous sublayer and is given by:

$$F_{turb} = e^{-\left(\frac{R_T}{4}\right)} \tag{4.15}$$

$$R_T = \frac{\rho k}{\mu \omega} = \frac{\nu_t}{\nu} \tag{4.16}$$

It can be seen that R_T is a ratio of the turbulent and the kinematic viscosity of the fluid. The ratio is also used to help predict separation induced transition with the definition of γ_{sep}:

$$\gamma_{sep} = \min \left\{ 2 \cdot \max \left[0 \; ; \; \left(\frac{Re_v}{3.235 Re_{\theta c}} \right) - 1 \right] F_{reattach} \; ; 2 \right\} F_{\theta t} \tag{4.17}$$

$$F_{reattach} = e^{\left(\frac{R_T}{20}\right)^4} \tag{4.18}$$

$$\gamma_{eff} = \max(\gamma \; , \; \gamma_{sep}) \tag{4.19}$$

The ratio $Re_v/3.235 Re_{\theta c}$ is similar to Eq. 4.2 with the exception of the constant 3.235. The change is associated with the rise in shape factor the laminar boundary layer experiences near separation. It can be observed near separation, γ_{eff} increases above the usual maximum value of one. This is necessary to account

for the rapid onset of transition triggered by flow separation as the production of k within the SST model does not increase rapidly enough. Finally, γ_{eff} is fed into the SST turbulence model as a scaling of turbulent kinetic energy (k) production. The modified k transport equation becomes:

$$\frac{\partial(\rho k)}{\partial t} + \frac{\partial(\rho U_j k)}{\partial x_j} = \tilde{P}_k - \tilde{D}_k + \frac{\partial}{\partial x_j}\left[(\sigma_k \mu_t + \mu)\frac{\partial k}{\partial x_j}\right] \tag{4.20}$$

with:

$$\tilde{P}_k = \gamma_{eff} P_k; \quad \tilde{D}_k = \min(\max(\gamma_{eff}, 0.1), 1.0) \cdot D_k \tag{4.21}$$

The blending function (F_1) of the SST turbulence model is also modified with the inclusion of the transition model.

$$\tilde{F}_1 = \max(F_{1,orig}, F_3); \quad F_3 = e^{-\left(\frac{R_y}{120}\right)^8}; \quad R_y = \frac{\rho y \sqrt{k}}{\mu} \tag{4.22}$$

The Langtry-Menter transition model has been validated on a number of different test geometries over the course of its development. The correlations, $Re_{\theta t}, Re_{\theta c}$, and F_{length} have seen considerable iteration and the accuracy of model continues to improve as more validation studies are conducted. With this in mind, one apparent weakness of the methodology is the dominant influence of the freestream turbulence intensity parameter in the correlations. This is an issue that will be demonstrated and discussed throughout the overview of the test cases.

Test Cases

The calibration of the transition model was performed on various flat plate cases, a turbine cascade, the S809 airfoil, and a multi-flap aircraft configuration. The results from the flat plate and S809 tests will be further explored to validate the implementation of the model in OVERFLOW, while results from the other geometries are presented in Langtry and Menter [37], and discussed in depth in Langtry [94]. Additionally, as the current work is part of a joint partnership, results from tests conducted at Texas A&M on a NACA $63_3 - 418$ airfoil are provided as further validation and to demonstrate the influence of freestream turbulence intensity.

Flat Plate

The flat plate test cases are based off an experiment conducted by the European Research Community on Flow Turbulence and Combustion (ERCOFTAC) [95] along with the results of Schubauer and Klebanoff [16]. The ERCOFTAC T3 series has become a benchmark for transition model studies with tests that use multiple pressure gradients and varying turbulence intensities [95]. The inflow conditions were set according to the reported freestream turbulence intensities (FSTI) and the ratio of freestream turbulent eddy to molecular viscosity (μ_t/μ) set to match the experimental decay rate of turbulence intensity. The tests

were performed using the code ANSYS CFX. The inlet conditions are summarized in Table 4.1 and the results from Langtry and Menter shown in Figure 4.2.

Table 4.1. Flat plate inflow conditions

Test Case	Inlet Velocity (m/s)	FSTI $(\%)$	μ_t/μ	Density (kg/m^3)	$\mu \ (kg/ms)$
T3A	5.4	3.3	12.0	1.2	$1.8 \cdot 10^{-5}$
T3B	9.4	6.5	100	1.2	$1.8 \cdot 10^{-5}$
T3A-	19.8	0.874	8.72	1.2	$1.8 \cdot 10^{-5}$
Schubauer and Klebanof	50.1	0.3	1	1.2	$1.8 \cdot 10^{-5}$
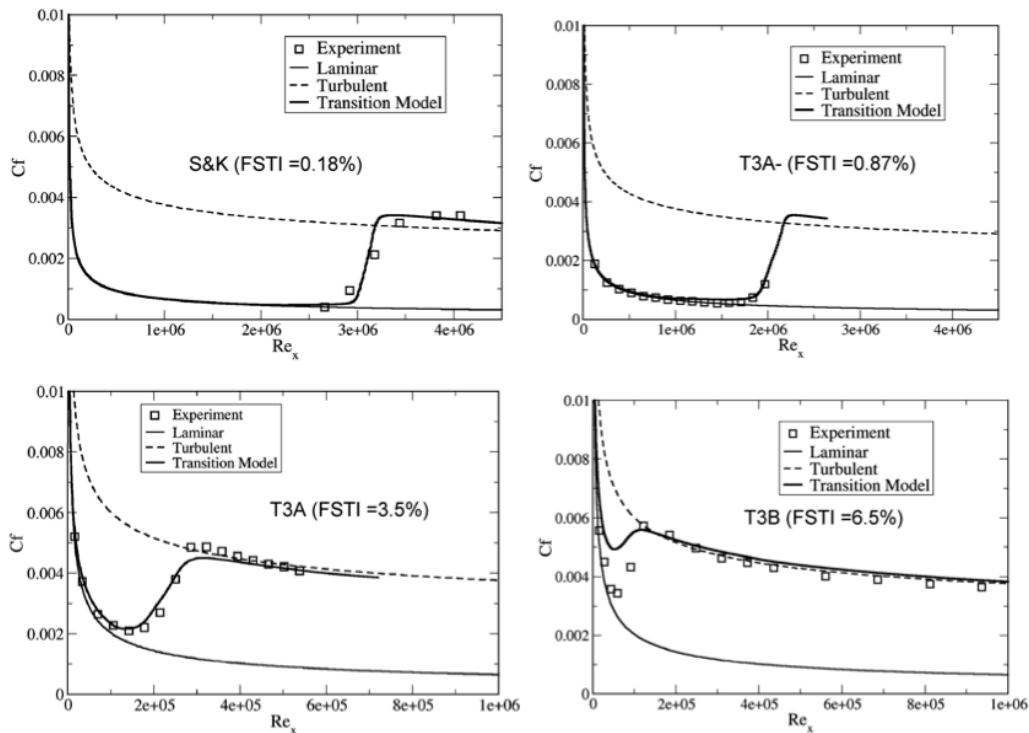
Figure 4.2. Zero pressure gradient flat plate test cases with varying freestream turbulence intensity, adapted from Langtry and Menter [37]

The Langtry-Menter transition model was developed for use in the code ANSYS CFX, and the correlations left as proprietary information in the initial publication of the methodology. The full equation set was then published in 2009 and subsequently coded into the latest release of OVERFLOW-2, version 2.2e. The zero-pressure gradient ERCOFTAC test cases were used as a validation of the implementation of the Langtry-Menter model in OVERFLOW-2. In the process of running flat plate cases a number of issues arose regarding the freestream turbulence intensity parameter. The initial computational mesh used for the validation of the flat plate test cases included three distinct sections, an inflow with inviscid wall, a viscous wall section corresponding to the flat plate, and an inviscid outflow (see Figure 4.3).
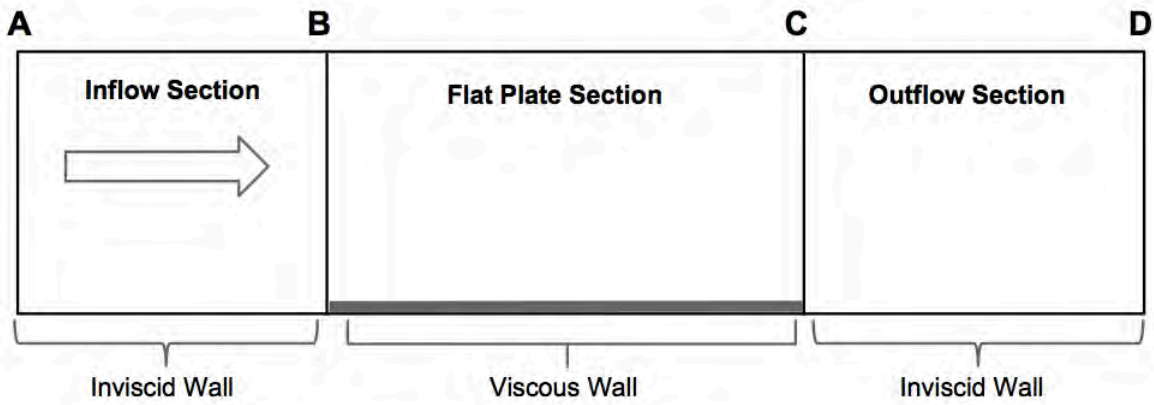
Figure 4.3. Outline of flat plate grid regions used in current study show-
ing placement of viscous and inviscid wall boundary condition

After prescribing the given freestream flow and turbulent conditions in the OVERFLOW-2 input file, the results unphysically indicated the flow was fully laminar along the length of the plate as shown in Figure 4.4. For reference the labeling convention in OVERFLOW-2 is the following, both are set under *FLOWINP* parameters with the variable *XKINF* corresponding to *FSTI*, and the variable named *RETINF* to (μ_t/μ).

Upon further examination and referencing an article by Spalart and Rumsey the problem arose due to the decay of freestream turbulence intensity [96]. The turbulent intensity is prescribed at the start of the inflow section (**A**) as indicated in Figure 4.3 however due to the destruction term in the transport equation for turbulent kinetic energy, the model predicts an unphysical drop in FSTI along the inflow section. The decay of k is associated with lack of proper grid resolution in the inflow section of the computational grid giving rise to unphysical numerical dissipation. The turbulence model did not include the influence of FSTI on transition; therefore, when using the transition model that is heavily correlated to turbulence intensity, additional considerations must be made. The approach taken by Langtry was to effectively eliminate the inflow section of the computational grid and prescribe the freestream turbulence conditions at the leading edge of the flat plate (B), see Figure 4.5. This eliminates the artificial dissipation in the inflow section created due to traditionally large grid spacing in the streamwise direction in this section.

The approach using a grid without an inflow region is shown in the current study primarily as a comparison to the published results, as the removal of the inflow section also eliminates the influence of any flow feature upstream of the leading edge. Due to the possibly significant changes in flow physics this might impose, two other solutions were investigated. The first was a limiter imposed on the turbulence model that limited the decay of ω along the inflow section. The second alternative procedure was to use multiple grids to represent the inflow and the flat plate section and combine the two using overset techniques. In separating the grids by oversetting, separate boundary and flow conditions can be prescribed allowing an inviscid solution to be imposed in the inflow region.

48
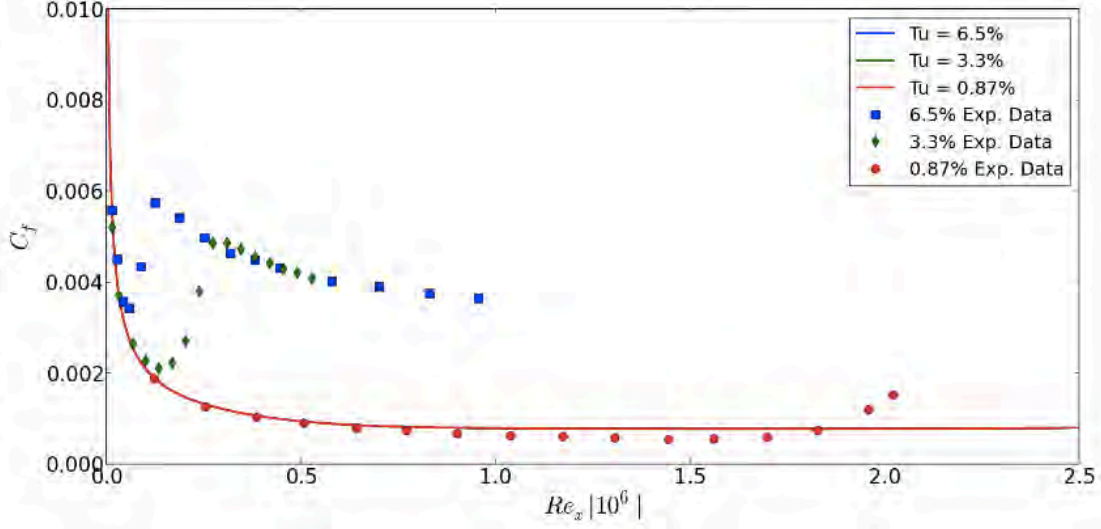
Figure 4.4. Unphysical laminar solution obtained due to freestream turbulence decay rates in the inflow section of flat plate grid, different lines are indistinguishable as all three turbulence intensities produce identical solution

1. Decay Limiter

The decay limiter was provided in the release notes of OVERFLOW-2 and modifies the destruction term in the equation for ω within the SST turbulence model. The modification followed the recommendation of minimum values imposed on the turbulence variables to avoid an unphysical decay off solid wall boundaries created due to numerical dissipation [96]. The adjustment is as follows with the original equation for ω:

$$\frac{\partial(\rho\omega)}{\partial t} + \frac{\partial(\rho U_j\omega)}{\partial x_j} = P_\omega - \beta\rho\omega^2 + 2(1-F_1)\sigma_\omega 2\frac{\mu_t}{k}\frac{\partial k}{\partial x_j}\frac{\partial \omega}{\partial x_j} + \frac{\partial}{\partial x_j}\left[(\sigma_\omega\mu_t + \mu)\frac{\partial \omega}{\partial x_j}\right] \qquad (4.23)$$

The modification:

$$\beta\rho\omega^2 \;\rightarrow\; \beta\rho\omega(\omega - C_\omega) \quad \text{where} \quad C_\omega = \text{Freestream decay rate} \qquad (4.24)$$

A rationalization may be made regarding the magnitude of the terms involved, as:

- ω near viscous wall $\qquad \sim O(1)$

- ω near inviscid wall $\qquad \sim O(10^{-4} - 10^{-5})$

- Freestream decay rate (C) $\quad \sim O(10^{-4} - 10^{-5})$

In effect the the limiter switches off the decay near inviscid walls corresponding to the inflow section
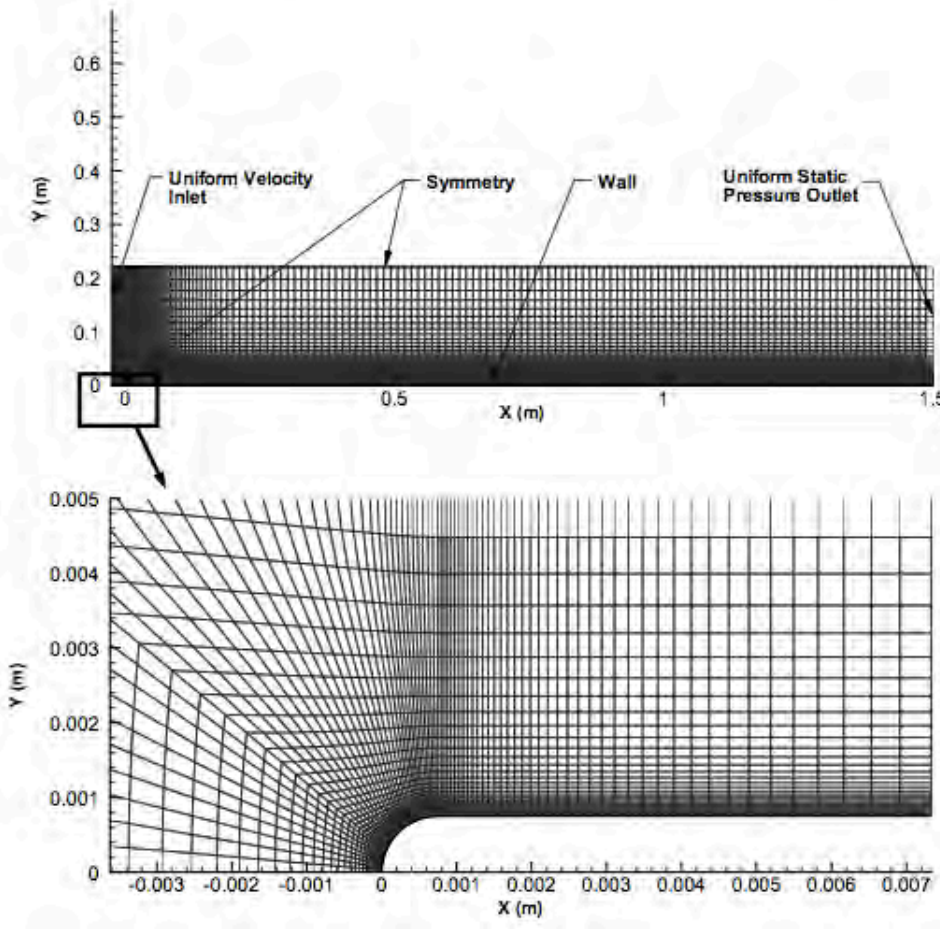
Figure 4.5. Schematic of the grid used by Langtry in validation studies for T3 zero pressure gradient test cases with a close up of leading edge [94]

of the grid. As the modification is to the turbulence model directly, the change is not purely limited to the inviscid section, and there is a slight change in the model globally.

The resulting flow solutions indicate that using the decay limiter is effective, however, it involves directly modifying the SST turbulence model. As there are only a limited number of geometries tested using the limiter, and the SST model itself has been extensively validated there are concerns that modifying the destruction term may have some undiscovered consequences. Although implementation of the limiter has provided much more accurate results than without in the flat plate test cases, the reader is advised to move forward with caution if implementing such a scheme. This is provided as a possible suggestion as the investigator did not have time to analytically or more extensively explore the validity of this option by example.

Figure 4.6. Comparison of computed skin friction for various zero pressure gradient flat plate configurations using decay limiter

2. Overset Approach

The other approach taken to resolve the issue of freestream decay was to create separate grids for the inflow and the viscous flat plate section and combine the two using overset grid techniques. Once the computational domains of the two grids were interconnected, the viscous terms in the inflow grid were shut off to effectively translate the freestream turbulence conditions to the leading edge of the flat plate. The use of overset grids has a number of advantages over just eliminating the inflow region entirely, primarily that flow effects upstream of the leading edge of the plate are still accounted for at least in the inviscid sense. This is far more of an issue on more complex geometries where the accuracy of the solution would be severely affected if the entire inflow section was removed. The results from the overset configuration is shown in Figure 4.7.

The overset grid configuration demonstrated a much more accurate solution than the original unmodified mesh or the cases run with the SST modification. As the overset configuration is the most accurate alternative from both a theoretical and practical sense, it is recommended that studies incorporating the Langtry-Menter transition model consider moving forward using an overset approach to handle the issue of freestream turbulence decay. The use of overset grids can also be extended to more complex geometries using an O-type grid for airfoil tests.
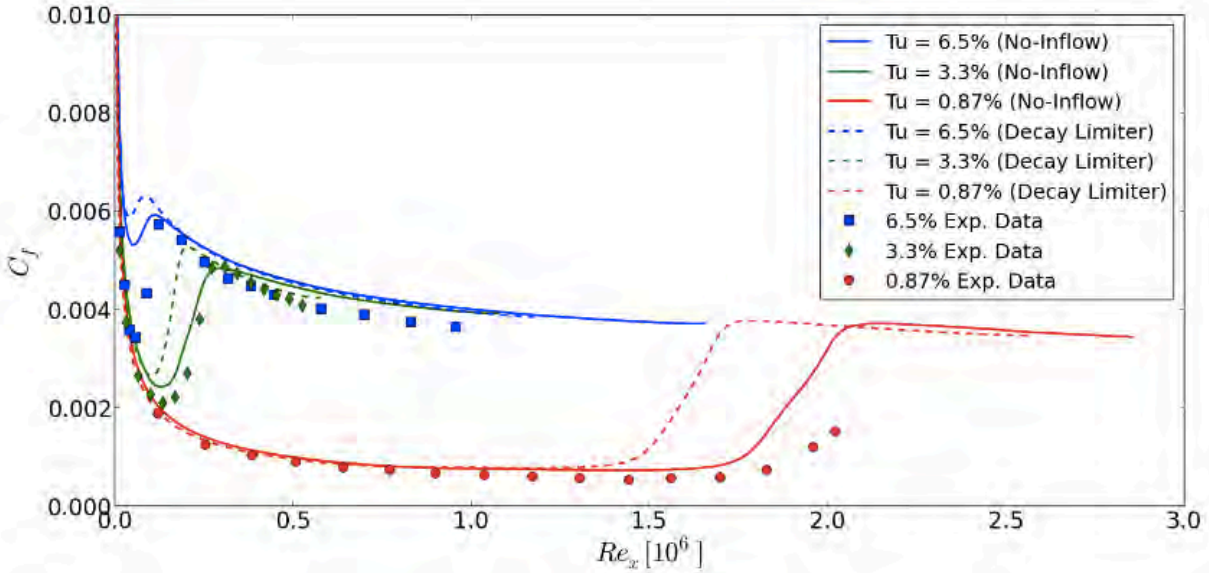
51
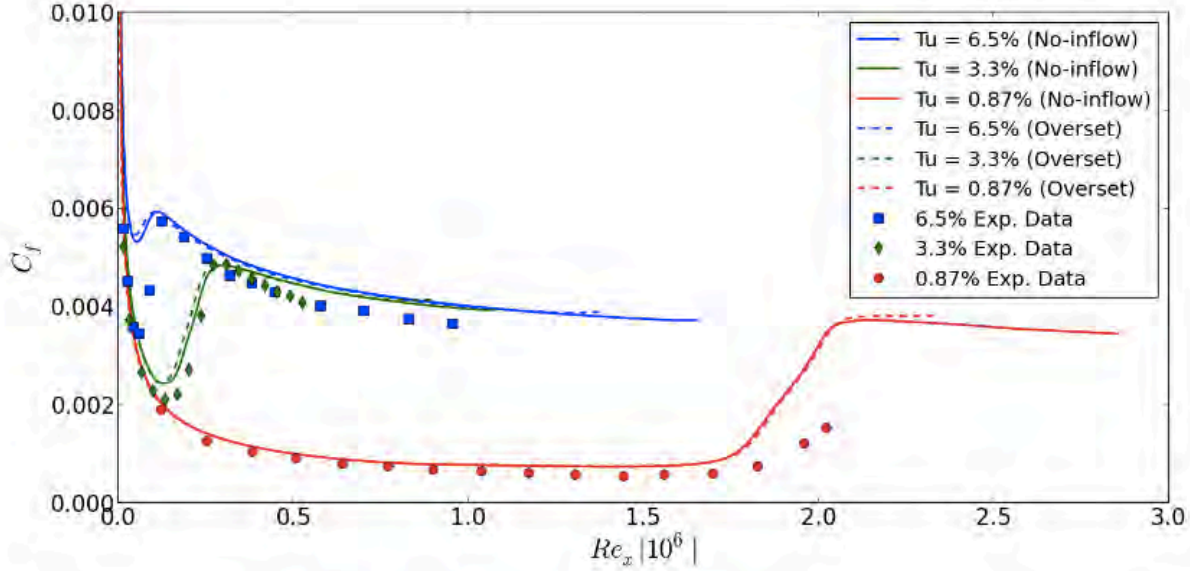
Figure 4.7. Comparison of computed skin friction for various zero pressure gradient flat plate configurations using overset grids

S809 Airfoil

The S809 is a thick airfoil designed primarily for use on stall-controlled horizontal axis wind turbines (HAWT). At moderate angles of attack, the flow along the airfoil is primarily laminar and then it experiences a laminar separation followed by reattachment as a turbulent boundary layer. These characteristics make it an ideal candidate for testing the capabilities of the transition model. The transition location plotted against angle of attack along with pressure distribution at an angle of attack of one are shown. Once more, detailed results can be found in Langtry. The grid used in the present study for the S809 airfoil was generated in a C-type configuration with 779 points in the j-direction and 222 in the normal direction. The wall spacing at the boundary was such that the $y^+ \approx .3$. An outline of the computational mesh can be seen in Figure 4.8. The inlet conditions are held constant at all angles of attack and are shown in Table 4.2. A C-type grid was chosen to match the the mesh used by Langtry. The laminar-turbulent transition of the boundary layer is pressure gradient driven which reduces the dominant influence of the freesream turbulence parameter. The cases were run with and without the decay limiter activated, and the results showed no change in transition location.

Table 4.2. S809 inflow conditions

Test Case	$Re_c \times 10^6$	Mach	FSTI (%)	μ_t/μ
S809 Airfoil	2.0	0.1	0.2	10.0

Figure 4.8. Airfoil section of C-type mesh used for S809 simulations

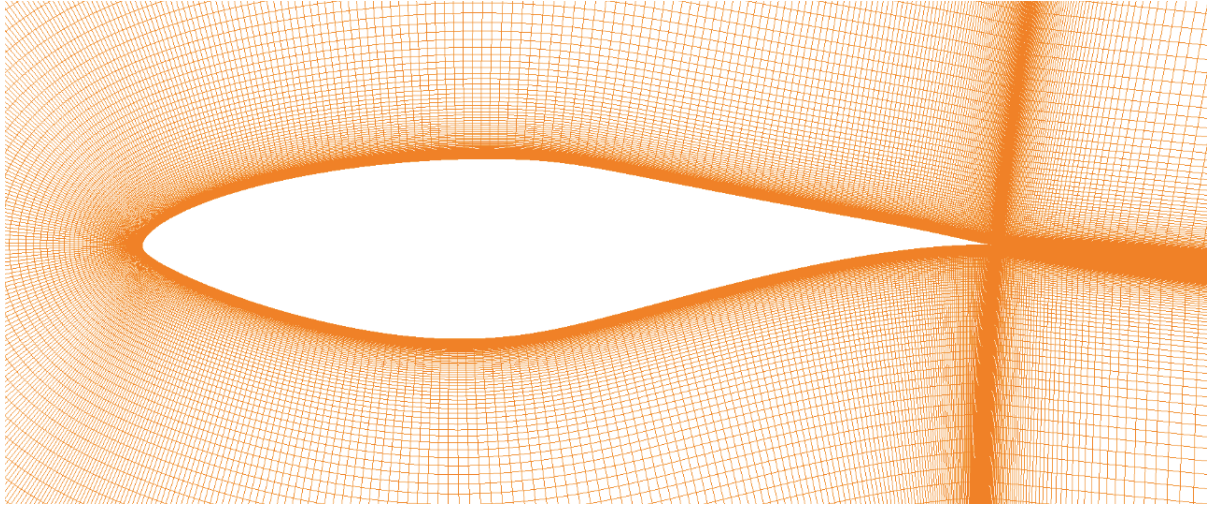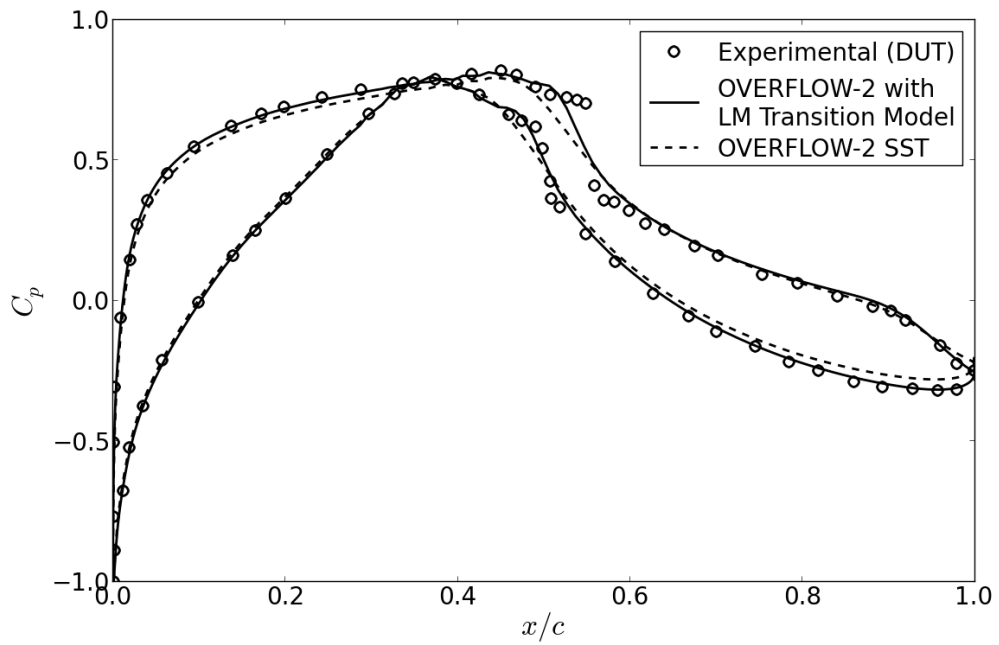**Figure 4.9.** Pressure distribution a 1° angle of attack, S809 airfoil, $Re_c = 2.0 \times 10^6$, $Tu = 0.2\%$

53

The S809 holds challenges for CFD simulations due to laminar flow separation at Reynolds numbers below 9×10^6 [21]. Accurate prediction of laminar separation can be obtained using the Langtry-Menter transition model; however, the bubble has a tendency to introduce unsteady effects and the solution must be time averaged. The pressure distribution at an angle of attack of 1° is shown, the markers correspond to experiments carried out at Delft University of Technology (DUT). The results from OVERFLOW-2 with the unmodified SST turbulence model in addition to a run with the Langtry-Menter model are shown in Figure 4.9. There is a clear distinction between the runs with and without the transition model as the SST turbulence model alone is clearly unable to predict separation on both the upper and lower surface. Additionally, the simulation with the transition model does not predict as abrupt of a drop in C_p following separation (around $x/c = .55$), which is likely due in part to the time averaging process. Regardless, the transition model does allow for more accurate simulation than with the unmodified turbulence model alone.

The transition location as compared to the same experimental results used in the original validation of the Langtry-Menter model can be seen in Figure 4.10. The results show a slight early prediction of the transition location, this is seen across many of the lower turbulence intensity flat plate test cases as well. Although it remains unclear why this tendency holds true, problems with accurately measuring turbulence intensity in experimental tests could alter the transition correlation enough to cause the shift. The trend of early onset prediction also holds constant when compared to the published results of Langtry and Menter. This gives rise to the possible explanation of slight differences in model implementation between OVERFLOW-2 and ANSYS CFX.
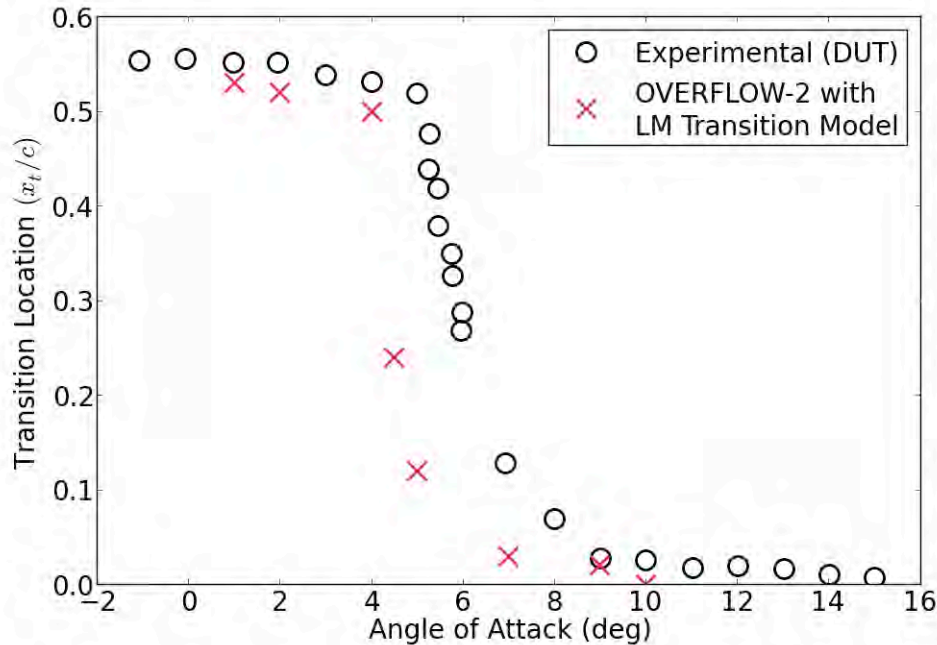

Figure 4.10. Transition location plotted against angle of attack, S809 airfoil, $Re_c = 2.0 \times 10^6$, $Tu = 0.2\%$

Despite the overall shift in transition location, the model predicts the rapid move forward in transition location correctly. The differences observed in overall drag can be substantial when comparing an airfoil

54

with a primarily laminar boundary layer and a configuration where the transition location is near the leading edge. If the same computational grid is run without the transition model, the turbulence model would generate a turbulent boundary layer almost immediately after the leading edge, even at angles of attack less than 4 deg. The quantitative result of the incorrect prediction is a 10% change in drag coefficient, and as seen in Figure 4.9, a shift in the overall pressure distribution along the airfoil. Despite some slight discrepancies the overall trend is a much more accurate prediction of airfoil characteristics using the transition model.

NACA 63$_3$ - 418 Airfoil

In conjunction with the development of the computational model, wind tunnel tests on a NACA 63$_3$ − 418 airfoil are being carried out at the Texas A&M Oran W. Nicks Low Speed Wind Tunnel (LSWT). The tunnel is closed return with a 7 ft × 10 ft test section and operates at a freestream turbulence intensity of approximately 0.24%. The NACA 63$_3$ − 418 was chosen as it is non-proprietary allowing for future validation studies. Additionally it is a frequently used airfoil for outboard rotor sections. The chord of the airfoil used was 0.813 m with a 2.1m span, more details regarding the test configurations can be found in [97]. To provide a baseline, the model is tested in a clean configuration, and compared to the OVERFLOW-2 results with the unmodified Langtry-Menter transition model. The O-type computational mesh, shown in Figure 4.11, contained 412 points along the surface and the initial wall spacing was set so the y^+ value remained much less than one.
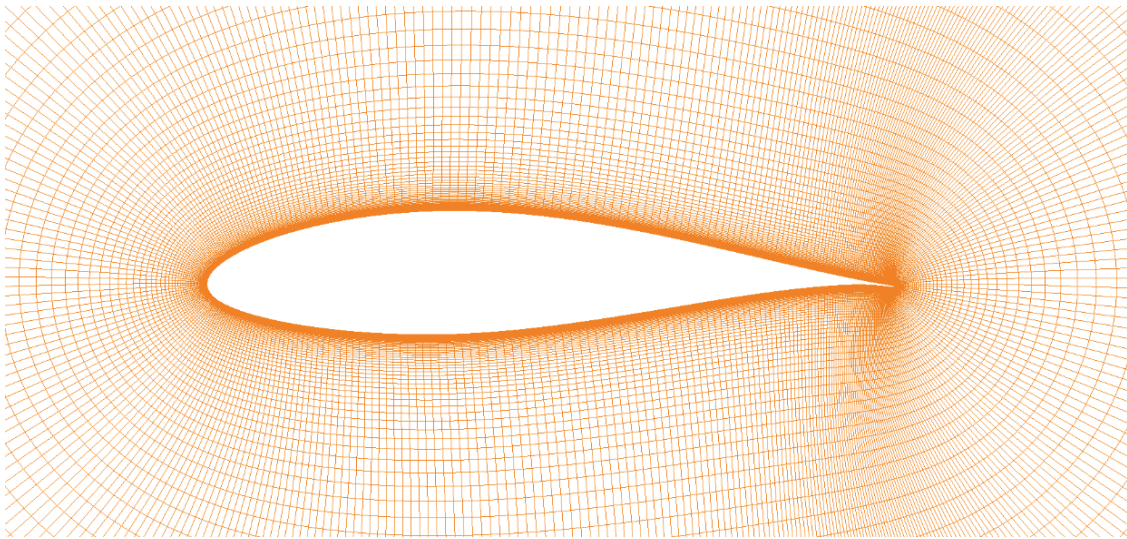
Figure 4.11. Airfoil section of O-type mesh used for NACA 63$_3$ − 418 simulations

The lift and drag comparisons for the clean configuration can be seen in Figure 4.13 and 4.14. There is a strong agreement between the experimental results and OVERFLOW-2 for the $Re_c = 1.6 \times 10^6$ cases, with the intermediate lift range very well aligned. There are slight discrepancies at higher lift coefficients, although this is not ideal, predicting post stall behavior is a well known weakness of RANS simulations.

Also provided as a comparison is the laminar-turbulent transition location as a function of angle of attack. The transition location was determined in the experiment using IR thermography, while the CFD
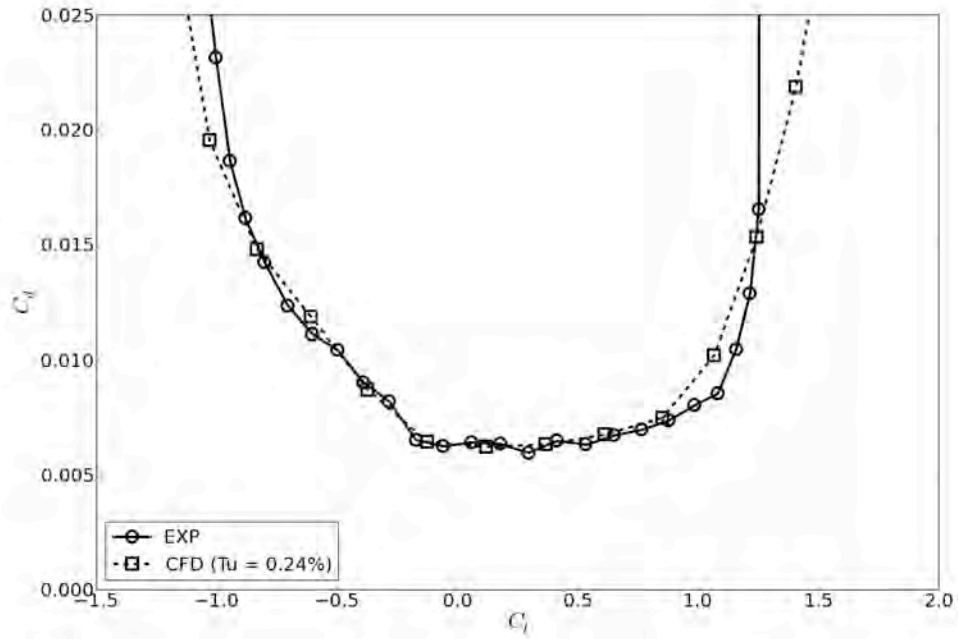
Figure 4.12. Drag polar of NACA $63_3 - 418$ airfoil, Langtry-Menter transition model and LSWT wind tunnel results, $Re_c = 1.6 \times 10^6$, $Tu = 0.24\%$

cases base the onset of transition on boundary layer shape factors. Once more the CFD simulations match up well with the experimentally reported results. The agreement of transition location is critical to accurate prediction of integrated values such as total lift and drag due to the differences in laminar and turbulent flow behavior.

As seen in Figure 4.14, there are a few discrepancies at the higher $Re_c = 3.2 \times 10^6$, demonstrating the sensitivity of the Langtry-Menter transition model to the freestream turbulence intensity as that was the only parameter changed between runs. The LSWT reports a freestream turbulence level of 0.24%, with that parameter the $Re_c = 1.6 \times 10^6$ cases line up with the experiment while the $Re_c = 3.2 \times 10^6$ cases clearly overpredict drag. There appears to be a sensitivity of the transition model to Reynolds number that may require the adjustment of the freestream turbulence intensity parameter or other aspect of the Langtry-Menter model accordingly.
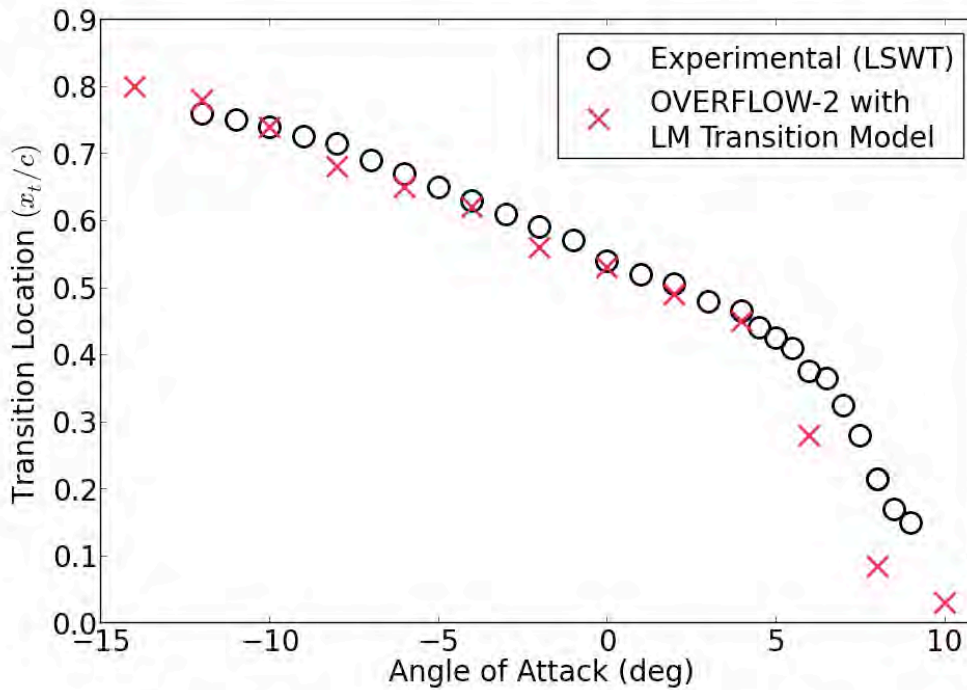
Figure 4.13. Transition location plotted as a function of attack, NACA $63_3 - 418$ airfoil, $Re_c = 1.6 \times 10^6$, experimental results from the Texas A&M LSWT, OVERFLOW-2 with Langtry-Menter transition model, $Tu = 0.24\%$

Modifications to Onset Criteria for Langtry-Menter Model

After examining the results of the cases run with the Langtry-Menter model, a clear trend emerges. At higher Reynolds numbers and angles of attack, the model predicts the onset of transition upstream of experimental results. This is indicated in Figure 4.14 where the early onset of transition causes a rise in the drag coefficient, effectively shifting the drag curve upward. This trend can also be seen in Figure 4.10, where the drop in transition location occurs slightly before the experimental.

Initially, attempts to explain discrepancies focused entirely on the freestream turbulence intensity param-eter due to the known influence on the model. Changing the freestream turbulence intensity parameter does provide more accurate results, however, for the model to operate robustly without a priori non-physical tuning of the parameter an alternate solution was explored.

Several researchers noted that a cause of the premature transition onset prediction was due to the function within the model that compared the strain-rate Reynolds number to the criteria for transition onset. As discussed in section 4.3 the model does not actually compute the momentum thickness of the boundary layer, but rather uses a relationship between the maximum value of the strain rate Reynolds number in the boundary layer, and a calibrated constant. One of the functions that controls the onset of transition is then defined as:
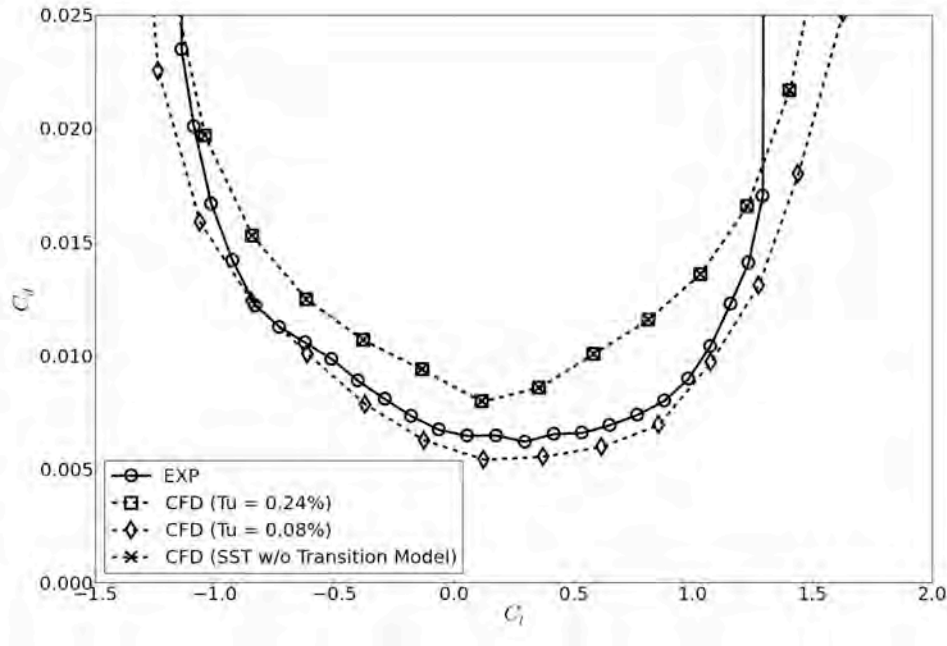
Figure 4.14. Drag polar of NACA $63_3 - 418$ airfoil, Langtry-Menter transition model with varying freestream turbulence intensity and LSWT wind tunnel results, $Re_c = 3.2 \times 10^6$

$$F_{onset1} = \frac{Re_v}{2.193 \cdot Re_{\theta c}} \tag{4.25}$$

The initial implementation was based on a Blasius profile with no pressure gradient where the relationship between Re_v and the momentum thickness Reynolds number is well defined. A solution investigated was to change the constant parameter in the F_{onset1} equation. By increasing the constant from 2.193 to 3.29, Khayatzadeh et al. [98] showed the model is less sensitive to freestream turbulence intensity and agrees better with the experimental results at higher Reynolds numbers and angles of attack. The modification effectively allows the boundary layer to develop further before switching the turbulence model on. The modified onset function:

$$F_{onset1,mod} = \frac{Re_v}{3.29 \cdot Re_{\theta c}} \tag{4.26}$$

The proposed modification was implemented in OVERFLOW-2 and the NACA $63_3 - 418$ cases reanalyzed to provide a first step at assessing the validity of the change. Figures 4.15 and 4.16 show the drag polars of the NACA $63_3 - 418$ airfoil at $Re_c = 1.6 \times 10^6$ and 3.2×10^6 with the onset function modification.

In Figure 4.15 the results of modification at $Re_c = 1.6 \times 10^6$ are almost identical in the lower portion of the drag bucket, and demonstrate better agreement at higher lift coefficients and therefore angles of attack. Around $C_l = -0.5$ the modified results actually deviate further from the experimental. The reason
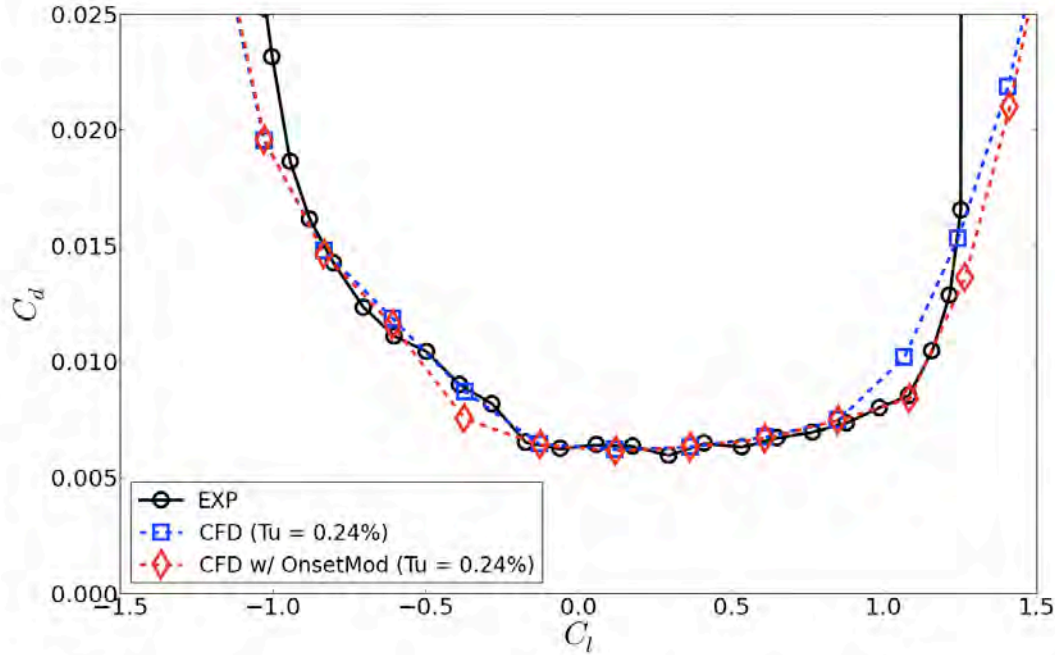
58

Figure 4.15. Drag polar of NACA $63_3 - 418$ airfoil, Langtry-Menter transition model with onset modification and LSWT wind tunnel results, $Re_c = 1.6 \times 10^6$

for this discrepancy, possibly due to a favorable pressure gradient at negative angles of attack, is still under investigation.

In Figure 4.16, the modified results at $Re_c = 3.2 \times 10^6$ demonstrate the purpose of the modification well, however the agreement with the experimental results still remains an issue. It can be seen that with the onset modification the results at $Tu = 0.24\%$ are closer to the LSWT results, but underpredict the drag coefficient (implying the prediction of transition occurs too far downstream) across the polar. The idea behind the modification was to allow the laminar boundary layer to grow to a larger shape factor before the onset function switches on the production of turbulent kinetic energy (k). It appears the modification may allow the laminar boundary layer to develop to much at higher Reynolds numbers, and the change of parameter constant will require further investigation.

A result that does show consistent improvement is the decreased sensitivity to freestream turbulence intensity. Without the modification, the difference between the cases run at $Tu = 0.24\%$ and those run at $Tu = 0.08\%$ (square markers vs. x's) is substantial. Furthermore, with the onset function modification implemented there is very little difference between the cases run at the different freestream turbulence levels. This is a very favorable effect of the modification and could potentially allow the model to behave more robustly without the user having to be particularly careful with the specification of the freestream turbulence levels. These turbulence levels are often not recorded accurately in experiments, and can be severely affected by numerical dissipation issues as demonstrated in previous sections.
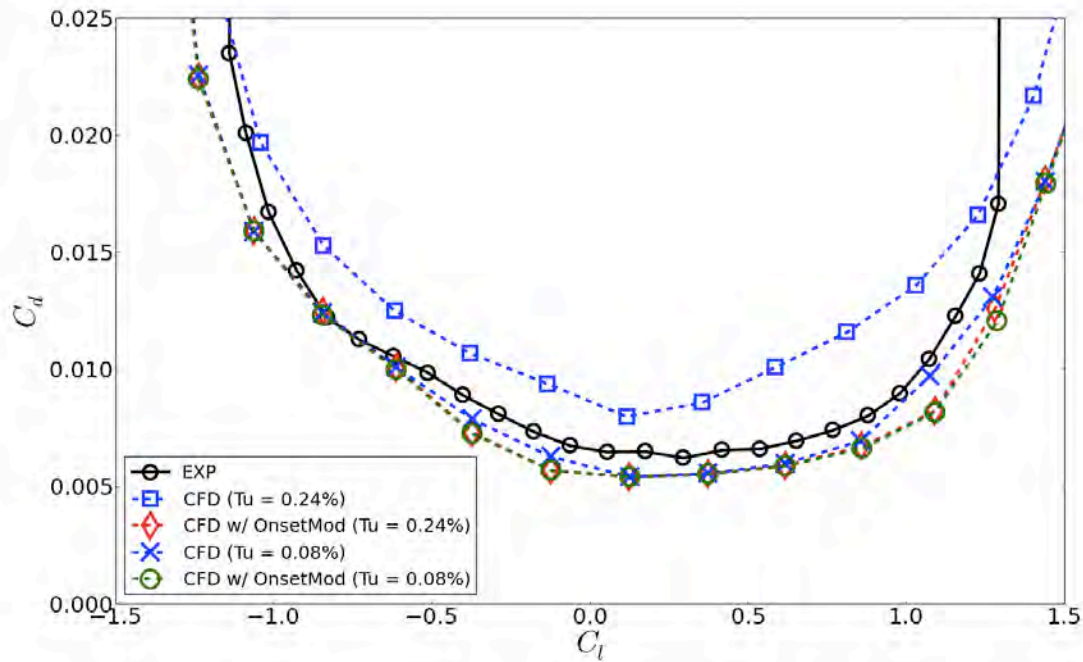
Figure 4.16. Drag polar of NACA $63_3 - 418$ airfoil, Langtry-Menter transition model with onset modification and varying freestream turbulence intensity, $Re_c = 3.2 \times 10^6$

Despite showing promise in lowering freestream turbulence sensitivity, the initial results do not provide enough conclusive evidence that the modification provides a robust improvement over the original formulation. Future work is planned to further investigate how a similar proposed change could improve the accuracy of the model at higher Reynolds numbers. The current modification changes the constant to simply a higher constant. It appears as though a single constant value is not adequate for all flow conditions, therefore the function itself may need a slight reformulation.

As the modification is still under active investigation, the tests conducted with the roughness model presented in the next chapter do not contain the modified onset function. Further rational is provided in Chapter 5 as the roughness modification will effectively override the original onset criteria.

Chapter 5

Roughness Model

Historically many different approaches have been taken to account for the influence of surface roughness on the nearby flow. The approaches generally involve some form of empirical correlation that scales up the practical effects such as increase in drag coefficient or frictional loss factor. As there are numerous factors that influence how surface roughness will alter the resulting flow field, the modeling problem grows in complexity. It has proven to be exceptionally difficult to generalize the effects or extend the correlations beyond very specific roughness configurations. There are two primary effects that the current work hopes to model: the shift of transition location upstream, and the increase in local skin friction along rough surfaces.

Despite the Langtry-Menter model accounting for many different modes of transition, it lacks the ability to simulate the effects of surface roughness. There are several reasons why the Langtry-Menter model itself cannot be directly modified to account for surface roughness. For one, unlike the boundary conditions for the SST model where the turbulent dissipation rate can be directly set at a viscous wall boundary, the values of intermittency and $\tilde{R}e_{\theta t}$ are not explicitly defined. The non-physical nature of both γ and $\tilde{R}e_{\theta t}$ mean the values must be determined implicitly through the solution of the transport equations. As to comply with a goal of the transition model, the location of the transition region is not known a priori, therefore it would be difficult to alter the boundary conditions of the model to account for roughness.

In an attempt to include the influence of surface roughness on boundary layer transition without having to geometrically redefine an existing grid, or case by case boundary conditions, Dassler, Kozulovic, and Fiala introduced a third term to the Langtry-Menter model [68]. The Roughness Amplification (A_r) variable is treated as an additional non-physical quantity produced at rough surface boundaries. Using a scalar transport equation, the variable is convected into the flow field and defines a region of roughness influence to locally modify the transition model downstream of a rough section. The variable attempts to represent the build up of roughness induced perturbations, and track the momentum deficit created in order to locally modify the criteria for transition onset. The form of the equation allows fluctuations in turbulent kinetic energy to be convected away from the roughness itself, and promotes an experimentally observed lag between encountering the rough section and the effects seen on the mean boundary layer flow.

Roughness Model Principles

The behavior of the Langtry-Menter transition model is strongly dependent on the momentum thickness of the boundary layer. Under similar freestream conditions, the higher the momentum thickness the more unstable the boundary layer becomes. Surface roughness has been reported to cause an increase in the momentum deficit behind the rough sections, and as a result increase the momentum thickness. This change will alter the correlation in the transition model as in principle it computes an estimate of the mo-

mentum thickness Reynolds number along a streamline and looks for a critical value as determined by the transport equation for $\tilde{Re}_{\theta t}$ (See Chapter 4 for more details). The options for modifying the correlation to account for roughness are to either increase the locally computed Re_θ, or lower the critical value, $\tilde{Re}_{\theta t}$, that must be obtained in the region affected by the surface roughness. This is accomplished with the roughness amplification variable A_r. How A_r is used to modify the correlation is outlined in the following this section.
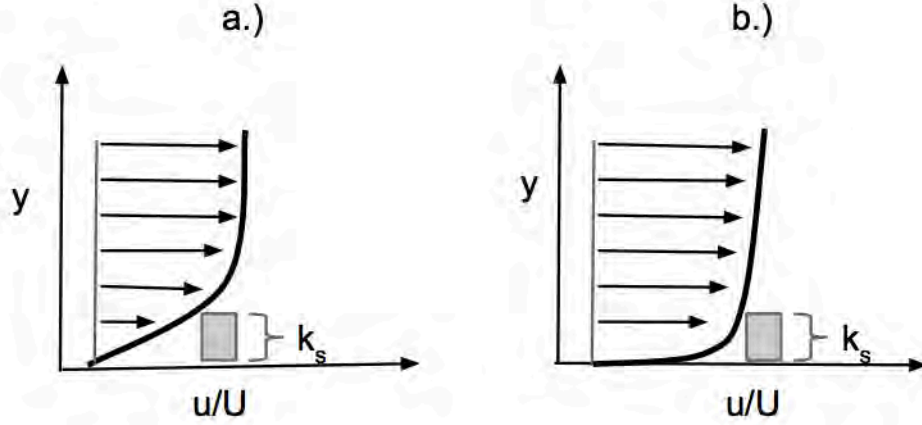
Figure 5.1. A comparison of the effect of a surface perturbation on the momentum deficit for boundary layers of two characteristic shapes, (a) boundary layer profile with low τ_w (b) boundary layer profile with high τ_w

To roughly determine the effects of roughness on a boundary layer flow a control volume approach was taken examining the momentum flux. Using the conservation of momentum equation:

$$\frac{\partial}{\partial t}(m\mathbf{v}) = \frac{\partial}{\partial t}\int_{CV}\rho\ dV + \int_{CS}\rho\mathbf{v}(\mathbf{v}\cdot\mathbf{n})\ dA \tag{5.1}$$

Assuming incompressible ($\rho_w \approx \rho$) and locally parallel steady flow where $\mathbf{v} = [u,0,0]^T$. Eq. 5.1 then reduces to:

$$\frac{\partial}{\partial t}(m\mathbf{v}) = \int_{CS}\rho u(u\cdot\mathbf{n})\ dA \tag{5.2}$$

Define the coordinate system such that x is the streamwise direction, y is the wall normal, and z the spanwise. Looking at a slice in the plane perpendicular to the streamwise direction (the $y-z$ plane) from the surface ($y=0$) to the boundary layer edge ($y=y_{edge}$). Additionally assume uniform flow along a unit span:

$$\frac{\partial p_x}{\partial t} \approx \int_0^{y_{edge}}\rho\left(u(y)\right)^2 dy \tag{5.3}$$

Looking at just the region from the wall to the height of the roughness, k_s:

$$\frac{\partial p_x}{\partial t} \approx \int_0^{k_s}\rho\left(u(y)\right)^2 dy \tag{5.4}$$

62

Assume the roughness is in the sublayer with linear varying velocity, $(u(y) = y(\partial u/\partial y))$:

$$\frac{\partial p_x}{\partial t} \approx \int_0^{k_s} \rho \left(y \frac{\partial u}{\partial z} \right)^2 dy = \int_0^{k_s} \rho \left(y \frac{\tau_w}{\mu} \right)^2 dy \tag{5.5}$$

$$\frac{\partial p_x}{\partial t} \approx \frac{\rho \tau_w^2 k_s^3}{3\mu^2} \tag{5.6}$$

There are dimensionality issues as there is an assumption of a unit span, this will effect calculations when considering varying roughness distributions, however, for the purpose of the calculations here the assumption can be made without too much loss of generality. If a unit time step is also used Eq. 5.6 further reduces to:

$$\Delta p_x \approx \frac{\rho \tau_w^2 k_s^3}{3\mu^2} \tag{5.7}$$

Physically Eq. 5.7 represents a crude estimate of the steamwise momentum that roughness of a given height can alter.

It is not difficult to see from Figure 5.1 and Eq. 5.7 that $\Delta p_2 > \Delta p_1$ implying that $\Delta p_x \approx f(k_s, \tau_w)$. The larger the Δp_x, the more potential the roughness has to extract streamwise momentum from the flow. As a larger loss of momentum is correlated with a larger increase in momentum thickness, it follows logically that A_r should be a function of k_s and τ_w as well. It should be noted that from both an analytical and practical standpoint, the entirety of the Δp term is not extracted from the flow. A portion of the u momentum is transferred vertically and is has been reported experimentally to occasionally cause an inflection in the velocity profile over rough sections. However the purpose of the analysis here is to determine what variables the formulation should include so the simplified expression in Eq. 5.7 can be used as a guideline.

Two important parameters in studying the effects of surface roughness are the non-dimensional height k^+ and the roughness Reynolds number Re_k defined as:

$$k^+ = \sqrt{\frac{\tau_w}{\rho} \frac{k_s}{\nu}} \tag{5.8}$$

$$Re_k = \frac{\rho U_k k_s}{\mu} \tag{5.9}$$

where U_k is the velocity in an undisturbed boundary layer at height k_s, ν the kinematic viscosity (μ/ρ), and τ_w the shear stress at the wall. As they both include k_s, and k^+ is a function of τ_w the two can potentially be used to modify the momentum thickness correlation.

Interestingly, there is a direct relationship between them as:

$$Re_{k_s} \approx (k^+)^2 \tag{5.10}$$

The assumptions that must be made to arrive at Eq. 5.10 are that of a linearly varying near wall velocity and incompressibility. Therefore:

63

$$U_{k_s} = k_s \left(\frac{\partial u}{\partial y} \right)_{wall} = \frac{k_s \tau_w}{\mu} \tag{5.11}$$

$$Re_{k_s} = \frac{\rho \left(\frac{k_s \tau_w}{\mu} \right) k_s}{\mu} = \frac{\rho \tau_w k_s^2}{\mu^2} = \frac{\tau_w}{\rho} \frac{k_s^2}{v^2} = (k^+)^2 \tag{5.12}$$

This relationship can be used to include empirically correlated values of $Re_{k,crit}$ while only having to compute k^+. Therefore, the formulation of the A_r variable, determined by a boundary condition at a rough wall, need only be a function of k^+. To determine the general form of the modification, the following analysis was performed.

Given the definition of momentum thickness for incompressible flow:

$$\theta = \int_0^\infty \frac{u(y)}{u_0} \left(1 - \frac{u(y)}{u_0} \right) dy \tag{5.13}$$

Assume linear varying velocity near wall:

$$u(y) \approx y \left(\frac{\partial u}{\partial y} \right)_{wall} = y \left(\frac{\tau_w}{\mu} \right) \tag{5.14}$$

Examining the contribution to θ from $0 < y < k_s$, therefore $\theta_{rough} = \theta - \Delta\theta$ with $\Delta\theta$:

$$\Delta\theta = \int_0^{k_s} \frac{y \left(\frac{\tau_w}{\mu} \right)}{u_0} \left(1 - \frac{y \left(\frac{\tau_w}{\mu} \right)}{u_0} \right) dy = \frac{1}{u_0} \int_0^{k_s} y \left(\frac{\tau_w}{\mu} \right) dy - \frac{1}{u_0^2} \int_0^{k_s} \left[y \left(\frac{\tau_w}{\mu} \right) \right]^2 dy$$

$$\Delta\theta = \frac{1}{2u_0} k_s^2 \left(\frac{\tau_w}{\mu} \right) - \frac{1}{3u_0^2} k_s^3 \left(\frac{\tau_w}{\mu} \right)^2 \tag{5.15}$$

with the definition of k^+:

$$\Delta\theta = \frac{v}{2u_0} (k^+)^2 - \frac{v}{3u_0^2} \sqrt{\frac{\tau_w}{\rho}} (k^+)^3 \tag{5.16}$$

As $Re_\theta = \theta u_0 / v$ and $Re_{\theta,rough} = Re_\theta - \Delta\theta u_0 / v$:

$$Re_{\theta,rough} = Re_\theta + \frac{1}{3} u^+ (k^+)^3 - \frac{1}{2} (k^+)^2 \tag{5.17}$$

If one sets A_r as a direct function of k^+ , i.e. $A_r = c_{r1} k^+$, with c_{r1} as some constant, then:

$$Re_{\theta,rough} = Re_\theta + \frac{1}{3} u^+ \left(\frac{A_r}{c_{r1}} \right)^3 - \frac{1}{2} \left(\frac{A_r}{c_{r1}} \right)^2 \tag{5.18}$$

64

The nature of the interaction between the A_r variable and the resulting increase in Re_θ can thus be regarded as a cubic function.

The goal of the A_r variable is to trigger the transition process with a smaller disturbance. This can be accomplished by using the variable to increase the local momentum thickness Reynolds number as in Eq. 5.1, or lower the correlated critical value by a similar amount. The option taken is to decrease the local correlation variable $\tilde{Re}_{\theta t}$ by modifying the production term in the transport equation. The reason for this is the computation of the local momentum thickness number is based on a relationship to Re_v rather than a direct computation. The modified production term for $\tilde{Re}_{\theta t}$ becomes:

$$\tilde{P}_{\theta t} = c_{\theta t} \frac{\rho}{t} \left[(Re_{\theta t} - \tilde{Re}_{\theta t})(1 - F_{\theta t}) - b F_{A_r} \right] \tag{5.19}$$

In general, the interaction of A_r with the transition model is to drive down the local $\tilde{Re}_{\theta t}$ downstream of rough sections, where high levels of A_r occur. This is accomplished by modifying the production term for $\tilde{Re}_{\theta t}$ to decrease with high levels of A_r using the F_{A_r} function. In lowering $\tilde{Re}_{\theta t}$, the value the local Re_θ must obtain to trigger intermittency production will ultimately be decreased, and therefore the onset of transition will occur with smaller flow disturbances. Furthermore, depending on the size of the roughness, the function can even shift the onset of transition to the location of the roughness itself, representing a bypass transition.

Roughness Model Formulation

The distribution of A_r is determined by an additional transport equation that takes a similar form to those of the transition model:

$$\frac{\partial(\rho A_r)}{\partial t} + \frac{\partial(\rho U_j A_r)}{\partial x_j} = \frac{\partial}{\partial x_j} \left[\sigma_{ar} (\mu + \mu_t) \frac{\partial A_r}{\partial x_j} \right] \tag{5.20}$$

The A_r transport equation does not include an explicit production term. Alternatively, the distribution of A_r is determined with a boundary condition at rough walls where the user inputs a representative equivalent sand grain roughness height (k_s). The vertical transfer of momentum is partially accounted for in the diffusion term of the transport equation that is dependent on the molecular and turbulent eddy viscosities. From the analysis in the previous section, the primary factor in determining the value of A_r at rough walls is the dimensionless sand grain roughness, k^+ as defined in Eq. 5.8. Upon computation of k^+ the value of A_r at the rough wall boundary is defined:

$$A_r|_{wall} = c_{r1} k^+ \tag{5.21}$$

The direct correlation defines the effective value of k^+ at both the wall boundary and distributes it according to the transport equation.

A secondary function that is based on the local A_r value is defined as:

$$F_{A_r} = \begin{cases} c_{r2} \cdot (A_r)^3 & : A_r < C_{A_r} \\ c_{r3}(A_r - C_{A_r}) + c_{r2} C_{A_r}^3 & : A_r \geq C_{A_r} \end{cases} \tag{5.22}$$

The cubic function at low values of A_r is designed to remain small enough such that a "hydraulically smooth" wall will have no effect on the transition model. Also, a cubic function is used as that is the general form of the interaction between k^+ and $Re_{\theta,rough}$ as supposed in the previous section. The cubic function is then switched to a linear function at an A_r value of C_{A_r} such that the slope of the cubic function matches that of the linear in order to prevent unphysical overshoots at high levels of A_r. The simplicity of the interaction is permissible as the transition model itself already includes the influence of many flow features that contribute towards the transition process.

The current model parameters used for the test cases presented are:

$$c_{r1} = 8.0 \quad c_{r2} = 0.0005 \quad c_{r3} = 2.0 \quad \sigma_{ar} = 10.0 \tag{5.23}$$

The F_{A_r} function is switched at $C_{A_r} = \sqrt{c_{r3}/3c_{r2}}$ to allow the smooth transition between the cubic and linear functions.

Another blending function is included so that when the local $\tilde{Re}_{\theta t}$ value nears the prescribed minimum from the transition model, the roughness model will no longer decrease the production of $\tilde{Re}_{\theta t}$. The function is defined:

$$b = \left[\frac{1}{2} \sin \left(\frac{\pi}{155} \tilde{Re}_{\theta t} - \frac{97\pi}{155} \right) + \frac{1}{2} \right]^2 \tag{5.24}$$
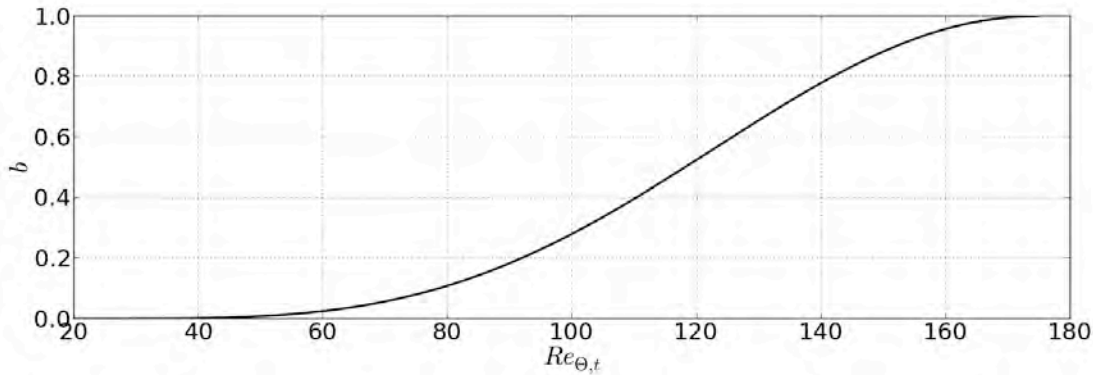
Figure 5.2. Graphical representation of the blending function, b

This prevents unphysical undershoots in the transition onset criterion, and smooths out the influence of A_r as the $\tilde{Re}_{\theta t}$ variable approaches the imposed minimal value.

Modification of SST Boundary Condition

The inclusion of the A_r variable in the transition model allows the model account for the early onset of transition under the influence of surface roughness. However, the effects on a fully turbulent boundary layer and the lowering of the turbulent dissipation rate along both the laminar and turbulent portion of

the boundary layer need additional consideration. Modifying the near wall turbulence model behavior can adequately represent the effects of distributed surface roughness on a fully developed turbulent boundary layer by shifting the expected mean profile in the law of the wall region [99]. The transformation of the logarithmic function for the mean velocity profile can be expressed:

$$u^+ = \frac{1}{\kappa}\ln y^+ + B \quad \rightarrow \quad u^+ = \frac{1}{\kappa}\ln y^+ + B - \Delta B \tag{5.25}$$

$$\Delta B = \frac{1}{\kappa}\ln k^+ - 3.65 \tag{5.26}$$

Originally, Nikuradse assumed the values of $\kappa = 0.40$ and $B = 5.5$ however these have been subsequently changed to $\kappa = 0.41$ and $B = 5.0$ [65].

This roughness induced change at the rough wall are accounted for using a modification of the boundary condition of the specific dissapation rate, ω.

The original boundary condition:

$$\omega_{smooth} = 10\frac{6\nu}{\beta(\Delta y)^2} \quad \text{with} \quad \beta = 0.09 \quad \text{at} \quad y = 0 \tag{5.27}$$

Here Δy represents the normal distance from the wall to the nearest grid point.

The update to account for roughness, originally proposed by Wilcox:

$$\omega_{rough} = \frac{\mu_\tau^2 S_r}{\nu} \quad \text{with} \quad \mu_\tau = \sqrt{\frac{\tau_w}{\rho_w}} \quad \text{at} \quad y = 0 \tag{5.28}$$

where S_r is dependent on the non-dimensional k^+ value.

$$S_r = \left(\frac{50}{k^+}\right)^2 \quad \text{if} \quad k^+ \leq 25 \tag{5.29}$$

$$S_r = \frac{100}{k^+} \quad \text{if} \quad k^+ > 25 \tag{5.30}$$

The modified boundary conditions allow the model to not only account for roughness induced transition, but also the effects on the fully turbulent boundary layer, including the increase in local skin friction.

Roughness Model Implementation

In the current study, the roughness amplification model was coded into the flow solver OVERFLOW-2. The code allows the user to select a number of different turbulence models, and the release of version 2.2e
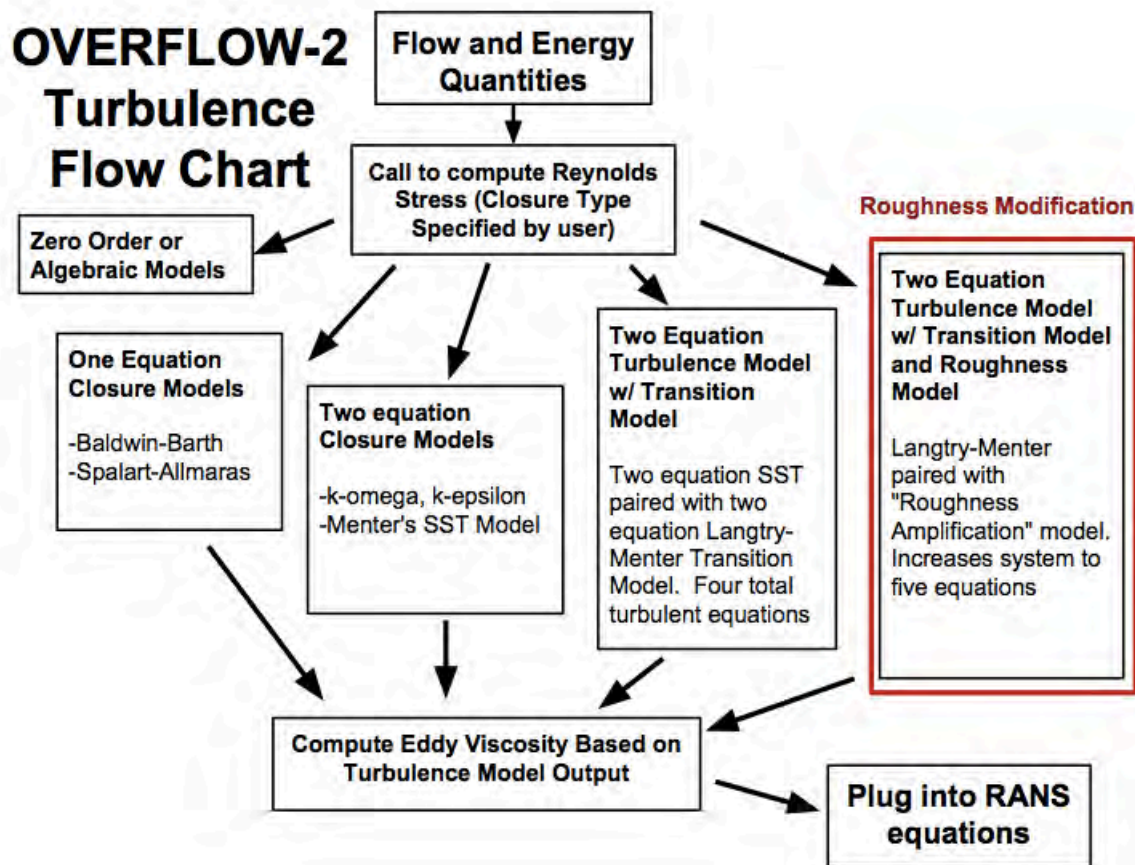
Figure 5.3. Turbulence Flow Chart in OVERFLOW-2

included the Langtry-Menter transition model. Figure 5.3 illustrates how the roughness model relates to the existing turbulence options.

Within OVERFLOW-2, the turbulence and transition model variables are solved separately from the primary flow quantities. At each iteration of the global solution, the turbulence/transition model variables are resolved, then the computed eddy viscosity is used for the primary flow equation. The flow variable equations are then iterated another step and the process is repeated.

To implement the roughness amplification model, global routines were modified to accommodate the additional flow quantity A_r. An additional "branch" of code was constructed that included the Langtry-Menter and new roughness amplification equations. The convective and diffusive fluxes were discretized using the same HLLC upwind scheme used in the existing Langtry-Menter model. The equation set requires an implicit solution and a linear system is constructed at each iteration. The linear matrix generated by the turbulence variables, including A_r, is solved using a successive symmetric over-relaxation (SSOR) algorithm similar to the one implemented for the Langtry-Menter model.

The roughness amplification model is activated by selecting a new option for the $N QT$ variable in the *GLOBAL* portion of the input file. The interaction the user has with the roughness model is to apply a bound-

ary condition to the surface contaminated by roughness with a representative k_s value passed in as an input parameter for that particular boundary. As the only change is a boundary condition, the model can easily be applied to existing grids without having to geometrically define the roughness. This is advantageous as roughness height sweeps can easily be performed to determine critical behavior, and different airfoil profiles can be tested for roughness sensitivity.

Roughness Model Calibration - Flat Plate

The calibration of the roughness model began with the flat plate test cases of Feindt used in the original validation of the model by Dassler et al. [68]. Figure 5.4 is provided to show the distribution of the A_r variable over a rough flat plate. The spike in A_r near $x/c = 0.0$ is due to the leading edge singularity, which generates a large increase in skin friction over the first 5% of the flat plate.
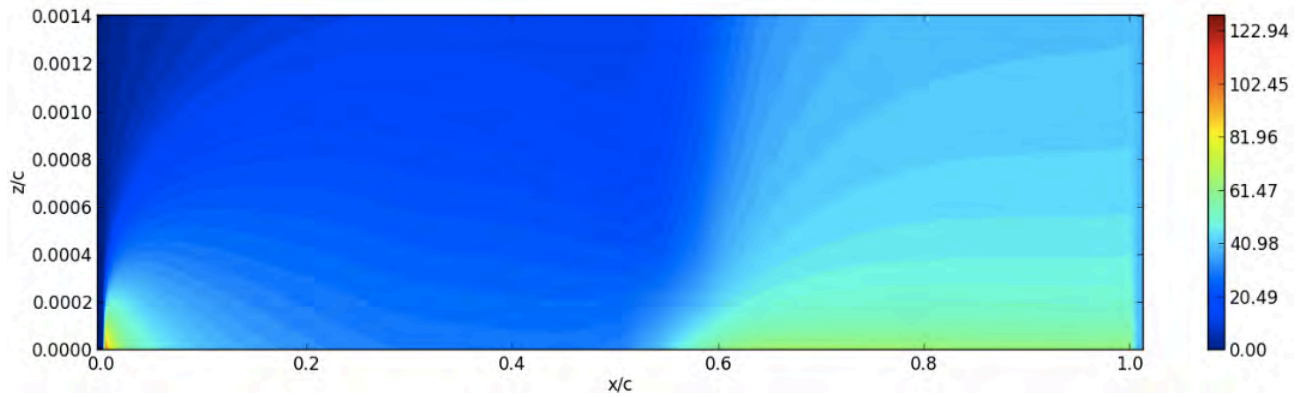

Figure 5.4. Contours of A_r over rough flat plate, $k_s = 120\mu m$, $Re_c = 1.3 \times 10^6$, zero pressure gradient, roughness applied $x/c = 0.02 - 1.0$

An import correlation in the study of roughness effects is that of the roughness Reynolds number (Re_k) and the corresponding location of transition onset, in non-dimensional form $(Re_{xt} = \rho U x_t / \mu)$, where x_t is the onset location measured from the initiation of the boundary layer. The experimental results of Feindt are used as a baseline calibration study. Three different pressure gradients are simulated using the grid geometry where the inlet height and length of the plate were fixed. In addition to the baseline zero gradient test, two of the grids utilized an expanding or constricting upper wall along the chord to provide an adverse or favorable pressure gradient respectively. The profile of the upper wall for the non-zero gradients was determined with the function:

$$y(x) = \sqrt{\frac{y_0^2}{\sqrt{1.0 - PG}}} \quad \text{with:} \quad PG = \frac{p_1(x) - p_0}{q_0} \tag{5.31}$$

where y_0 represents the distance from the flat plate to the upper wall at the inlet, p_0 and q_0 the static and dynamic pressure at the inlet respectively, and p_1 the static pressure along the plate. The PG parameter was set to match the conditions in the Feindt experiment for the two non-zero pressure gradient tests as seen in Figure 5.5. The initial distance from the plate to the upper wall, y_0 was set as $0.1495c$ to match the grid used

in the original CFD tests of Dassler, Kozulovic, and Fiala [68]. The input parameters held constant were the inlet velocity = 20 m/s, $\mu_t/\mu = 150$, $\rho = 1.2$ kg/m³, and $\mu = 1.8 \cdot 10^{-5}$ kg/m·s

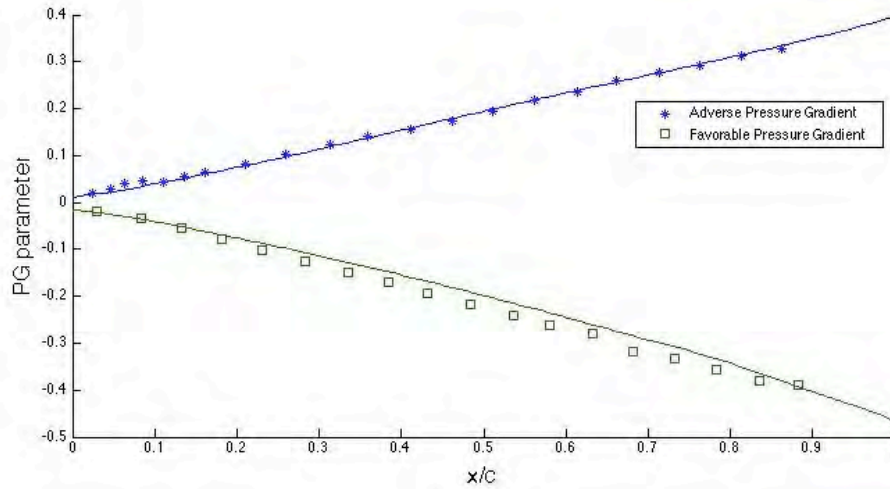**Figure 5.5.** Plot of PG parameter used in construction of the flat plate grids, markers correspond to experimentally measured while the lines indicate the computational prediction

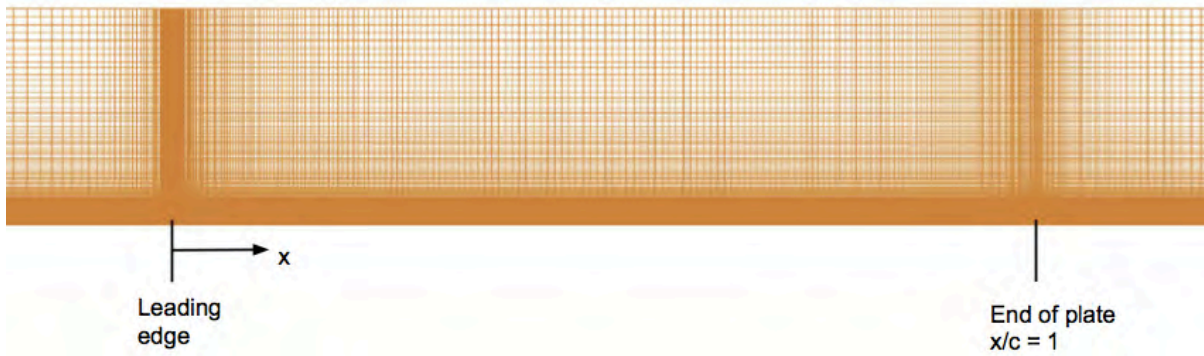An outline of the grid geometries can be seen in Figures 5.6 - 5.8

Figure 5.6. Grid used for zero pressure gradient test cases, inflow and outflow sections continue 10 and 25 chord lengths respectively in either direction (not shown)

Figure 5.7. Grid used for adverse pressure gradient test cases, inflow and outflow sections continue 10 and 25 chord lengths respectively in either direction (not shown)
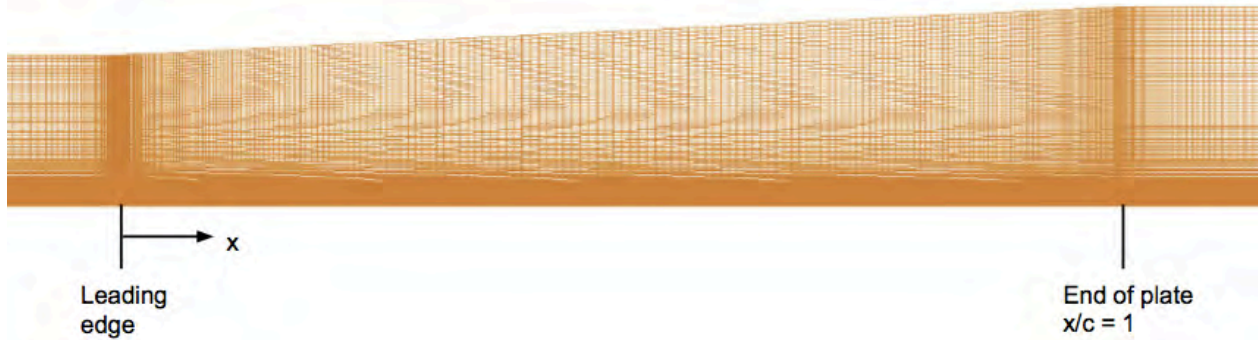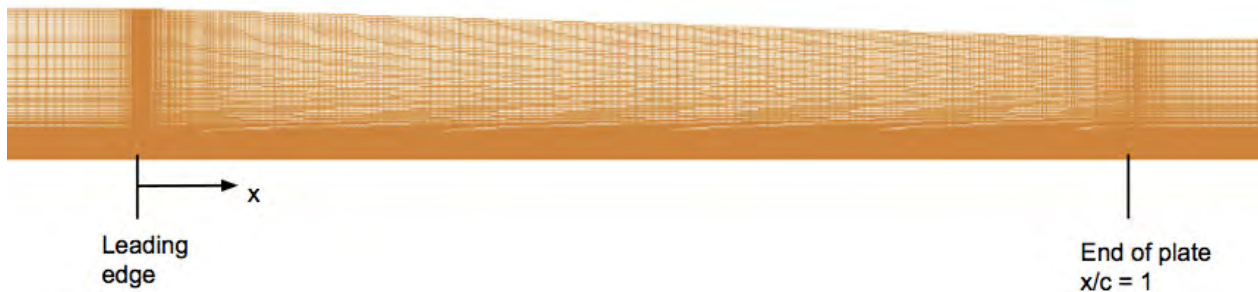

Figure 5.8. Grid used for favorable pressure gradient test cases, inflow and outflow sections continue 10 and 25 chord lengths respectively in either direction (not shown)

Information regarding freestream turbulence levels were not recorded in the Feindt experiment, so the turbulent intensities were set according to those used in Dassler et al. [68]. The levels are set such that the smooth wall behavior matches up with the experimental results. The tests used a Tu of 0.91% for the zero pressure gradient and adverse pressure gradient test cases. The favorable pressure gradient required a higher Tu than the condition used in Dassler et al. to retain an accurate simulation of smooth wall transition location. This could potentially be a product of the differences in implementation of the Langtry-Menter model in OVERFLOW-2 and in the code used by Dassler et al. Although not an ideal method to produce proper smooth wall behavior, the purpose of the flat plate cases was to determine how the roughness model compared to the original CFD implementation. Additionally, the age of the data set introduces high levels of uncertainly due to primitive measurement techniques. Despite the inherent limitation of the flat plate data the results serve as an appropriate first check for the implementation of the roughness amplification model. Additionally due to the simple geometry the skin friction profiles can be compared to what is expected theoretically.

Figure 5.9 demonstrates the effect of varying Re_k on the local skin friction coefficient (C_f), transition onset can be seen as the location where the local C_f spikes. Additionally, the large discrepancy in skin friction between the laminar portion (before the spike) and the turbulent emphasizes the importance of

accurately locating the transition onset location in drag calculations. As expected there is a clear trend as the value of Re_k increases, the location of transition onset moves upstream. There is only a slight change in transition location between the smooth and the lowest roughness configuration due to the physically observed phenomena of small roughness heights having a very small impact on the location of transition onset. Another trend is the modulation of the skin friction graphs upward in the "turbulent" portion with increasing Re_k, this effect can be attributed to the modification of the boundary condition for ω as discussed previously in section 5.2.1.
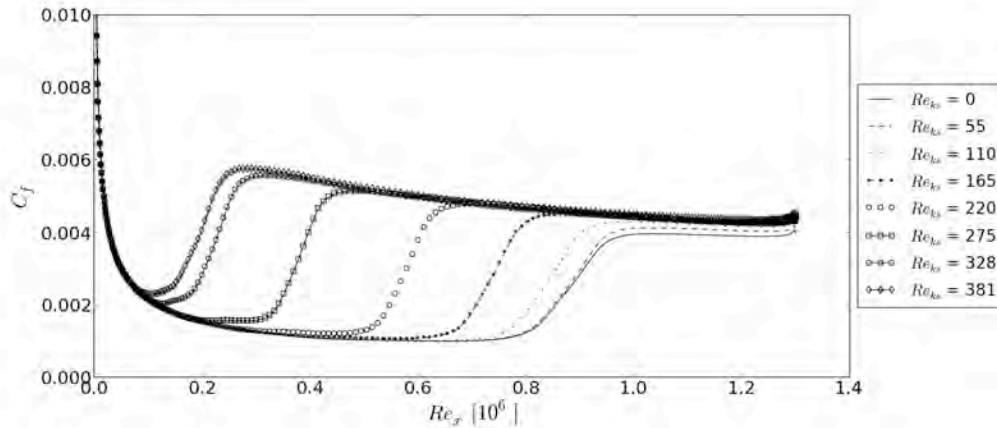

Figure 5.9. The effect on local skin friction coefficient (C_f) of varying Re_k. Zero pressure gradient flat plate, FSTI = 0.91%
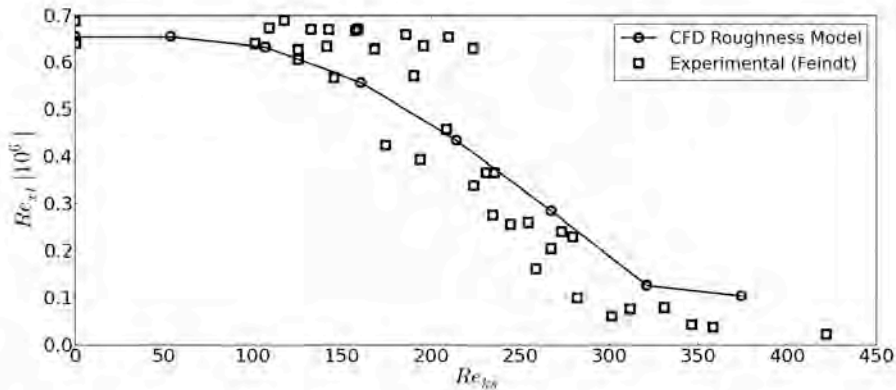

Figure 5.10. Roughness Reynolds number (Re_k) plotted against location of transition onset (Re_{xt}) for zero pressure gradient flat plate

After defining the location of transition onset as the location just before the skin friction plot spikes, the correlation between the Reynolds number of transition onset, Re_{xt}, and Re_k can be made. Despite the scatter in the experimental data, the model does a good job at predicting the overall trends up until large Re_k values. The model can be adjusted to behave better in the high Re_k range however this has a converse effect on accurately representing the boundary layer development. This issue is discussed more thoroughly in the section regarding the calibration study on the NACA 0012 airfoil. The critical range is roughly between $Re_k = 100 - 350$ which matches up with many experimental investigations on determining an $Re_{k,crit}$ for distributed roughness.

The results from the two non-zero pressure gradient configurations also show agreement throughout the Re_k range, and once more despite the scatter and uncertainly in the experimental data, predict the overall trends well. Another favorable characteristic of the method is the ability to represent subcritical roughness heights that will not immediately trigger the transition process. Crude roughness correlations often assume the boundary layer transitions at the location of the roughness, which can result in large discrepancies in drag predictions. The location of transition can have effects on the lift characteristics by promoting separation and changing the stall angle; therefore, accurate prediction of transition location may favorably change predictions.
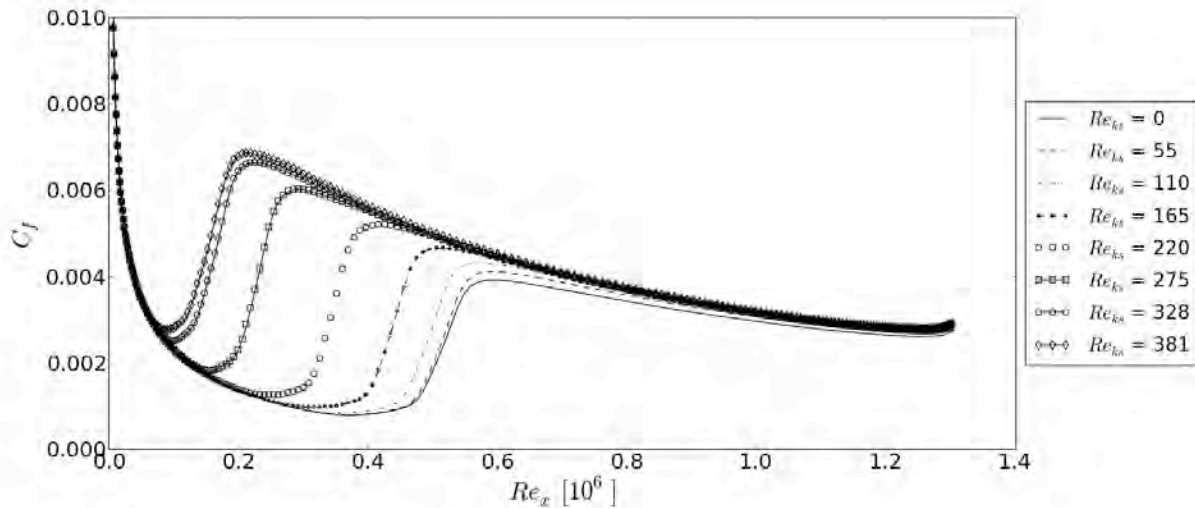
Figure 5.11. The effect on local skin friction coefficient (C_f) of varying Re_k. Flat plate, adverse pressure gradient, FSTI = 0.91%

73
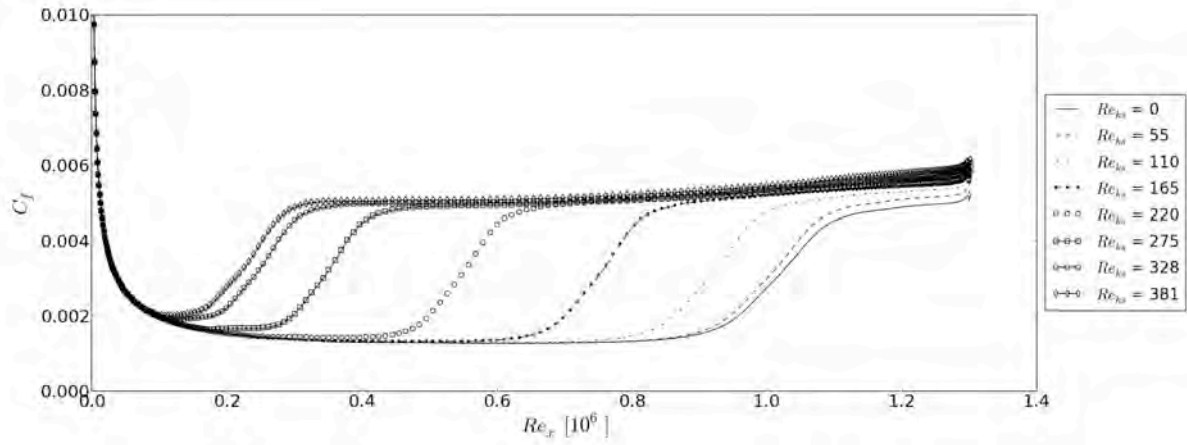
Figure 5.12. The effect on local skin friction coefficient (C_f) of varying Re_k. Flat plate, favorable pressure gradient, FSTI = 2.10%
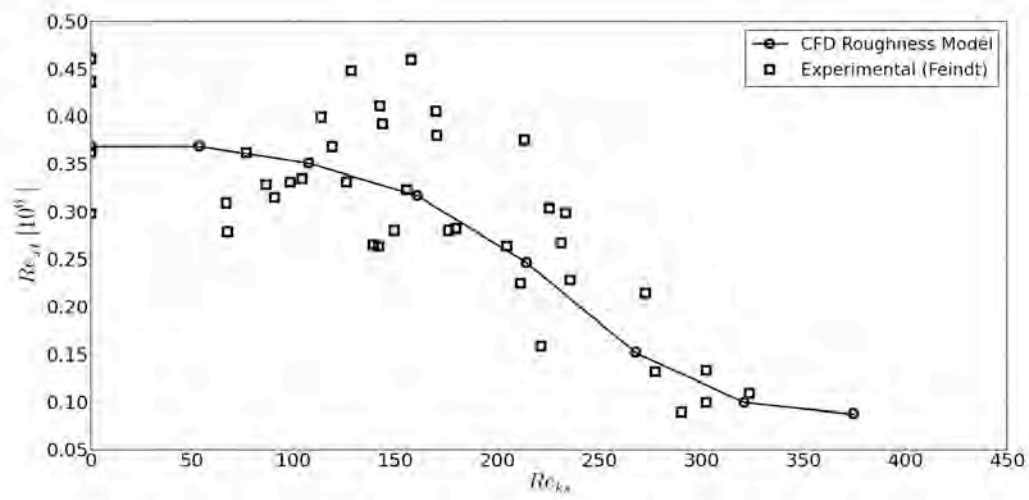

Figure 5.13. Roughness Reynolds number (Re_k) plotted against location of transition onset (Re_{xt}) for flat plate, adverse pressure gradient
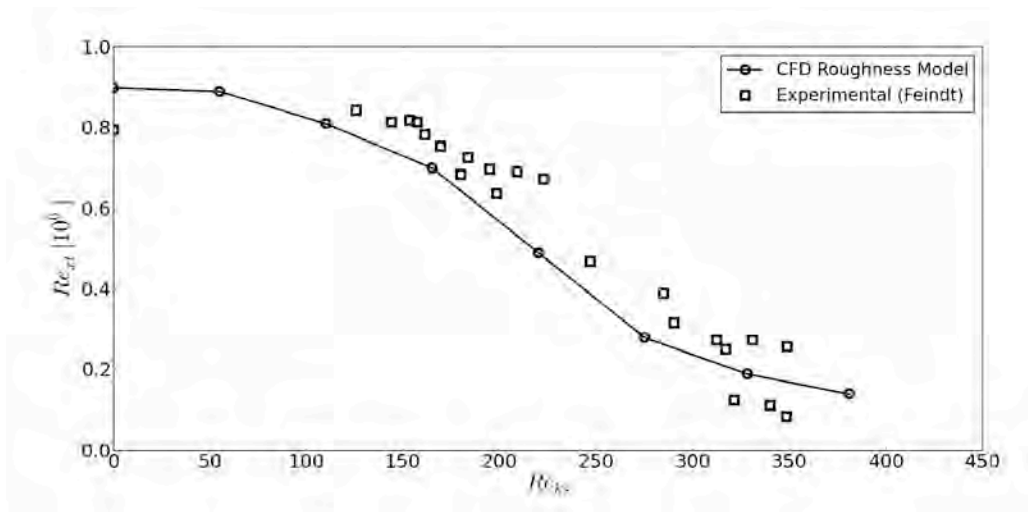
Figure 5.14. Roughness Reynolds number (Re_k) plotted against location of transition onset (Re_{xt}) for flat plate, favorable pressure gradient

Roughness Model Calibration - NACA 0012 Airfoil

The experimental results of Kerho and Bragg were used to asses the behavior of the model applied to an airfoil with large scale leading edge erosion at varying locations and extents [57, 2]. All experimental tests were performed on a NACA 0012 airfoil of chord length 0.5334 m using a tape strip with hemispherical shapes simulating distributed roughness. The roughness strips were nominally 0.35 mm high ($k/c = 656 \times 10^{-6}$) including the tape substrate and the center to center spacing of the rough elements was 1.3 mm. Figure 5.15 provides a picture of the simulated roughness used in the experiment.
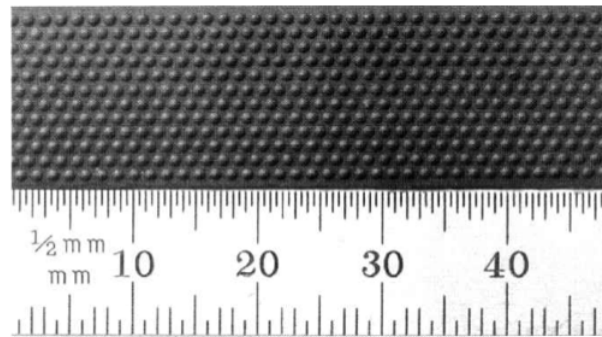
Figure 5.15. Image of simulated roughness used by Kerho and Bragg, adapted from [2]

The authors report the location of the start of the roughness measured in mm from the leading edge center and chordwise length of the rough region in inches. More information regarding the experimental configuration can be found in [2]. The labeling convention is used in this study to provide a means of referencing particular test configurations. A summary of the test configurations can be found in Table 5.1. A noteworthy characteristic is the particularly high Re_k values across all test configurations. Due to these high Re_k values, the test cases are useful in establishing the extremum behavior of the roughness amplification model.
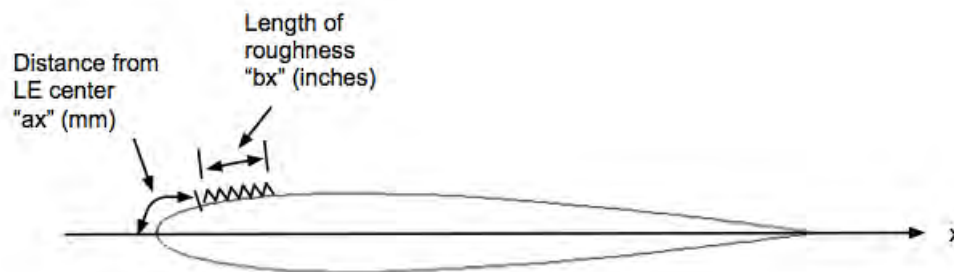
Figure 5.16. Sketch of NACA 0012 airfoil to demonstrate labeling convention

In the computational simulations, an overset O-type grid was used with 415 points along the surface

Table 5.1. Summary of roughness characteristics for $Re_c = 1.25 \times 10^6$ test cases [2]

Case bx @ ax	k/c $(\times 10^{-6})$	Re_k (start of roughness)	Re_k (end of roughness)	x/c of roughness
1/4" @ 7 mm	656	656	834	0.00490 - 0.0138
1/2" @ 4 mm	656	479	878	0.00187- 0.0191
1/2" @ 8 mm	656	701	907	0.00612 - 0.0258
1/2" @ 12 mm	656	811	920	0.0117 - 0.0327
1/2" @ 18 mm	656	899	918	0.0212 - 0.0432
1/2" @ 24 mm	656	919	899	0.0314 - 0.0539

and 141 in the normal direction of the innermost overset grid. The near wall grid spacing was such that $y^+ \approx .35$. Figure 5.17 depicts the region of the grid showing the airfoil and overset boundary. Additionally grid independence was checked with solutions computed on grids with 829 and 277 number of points along the airfoil surface.

Figure 5.17. NACA 0012 grid used showing the overset region, viscous terms only applied to inner grid to prevent numerical dissipation of freesteam turbulence variables

An attribute that made the Kerho and Bragg study particularly useful was the inclusion of detailed boundary layer profiles for many of the configurations as well as turbulence intensity data. Boundary layer profiles from a few of the test cases are compared to the roughness model an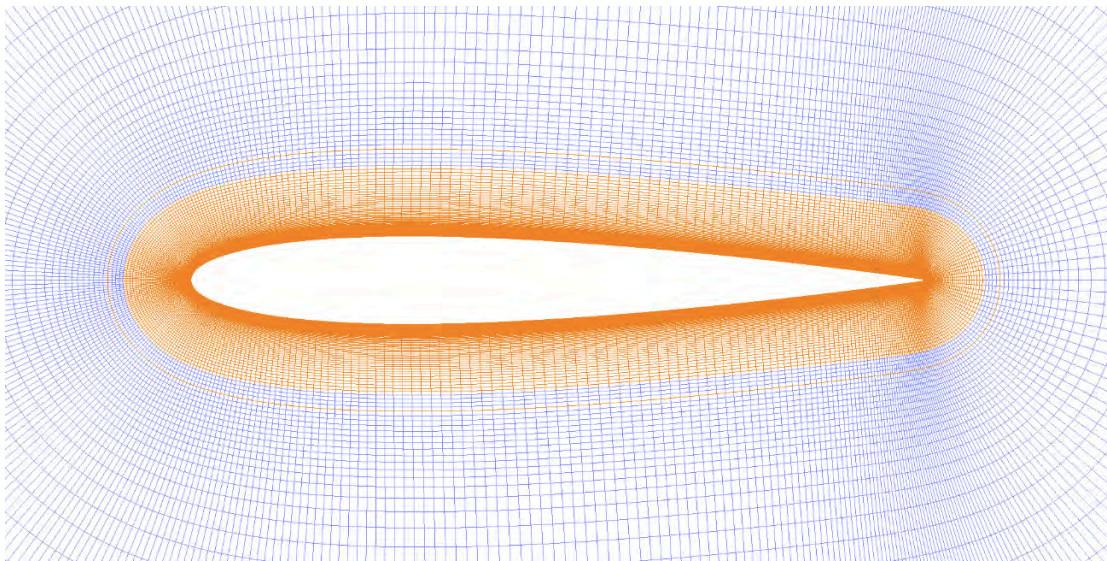d baseline Langtry-Menter transition model to demonstrate the impact the roughness has on the development of the boundary layer.

Figure 5.18. Boundary layer profiles: Kerho [57], unmodified Langtry-Menter transition model, computational roughness model. NACA 0012 airfoil, $Re_c = 1.25 \times 10^6$, $\alpha = 0^o$, $Tu = 0.1\%$, distributed roughness applied $x/c = 0.0018 - 0.0191$

Figure 5.19. Boundary layer profiles: Kerho [57], unmodified Langtry-Menter transition model, computational roughness model. NACA 0012 airfoil, $Re_c = 1.25 \times 10^6$, $\alpha = 0^o$, $Tu = 0.1\%$, distributed roughness applied $x/c = 0.0061 - 0.0258$

The first two cases (Figures 5.18 & 5.19) demonstrate significant improvement in comparison to the baseline Langtry-Menter model, and match up exceptionally well compared to the experimentally measured profiles. However, with the roughness located relatively far aft (Figure 5.20), slight discrepancies occur. As seen in the first two frames of Figure 5.20 ($x/c = .075$ & $x/c = .10$), the roughness model displays a lag in transition onset prediction, and the profile produced by both the roughness and Langtry-Menter transtion model follow a typical laminar profile. By $x/c = .15$ the roughness model has influenced the transition model enough such that the boundary layer profile begins to shift closer to the experimental.
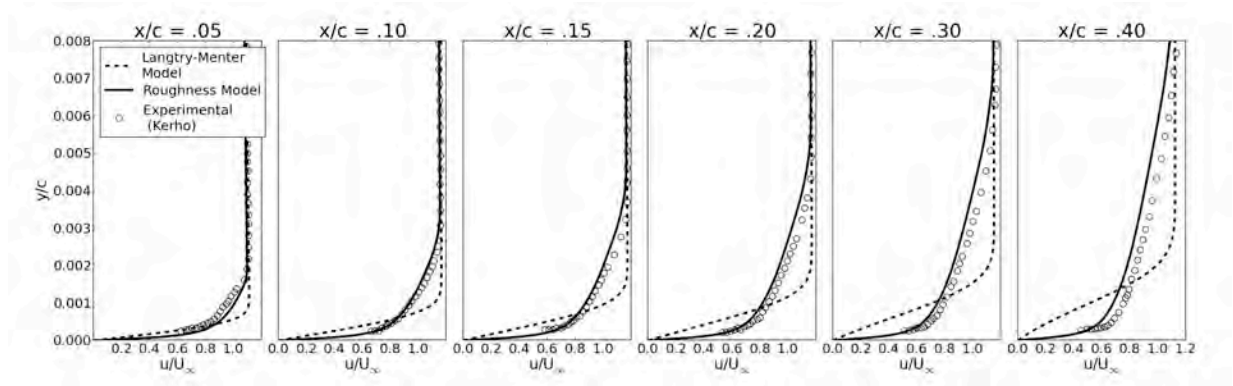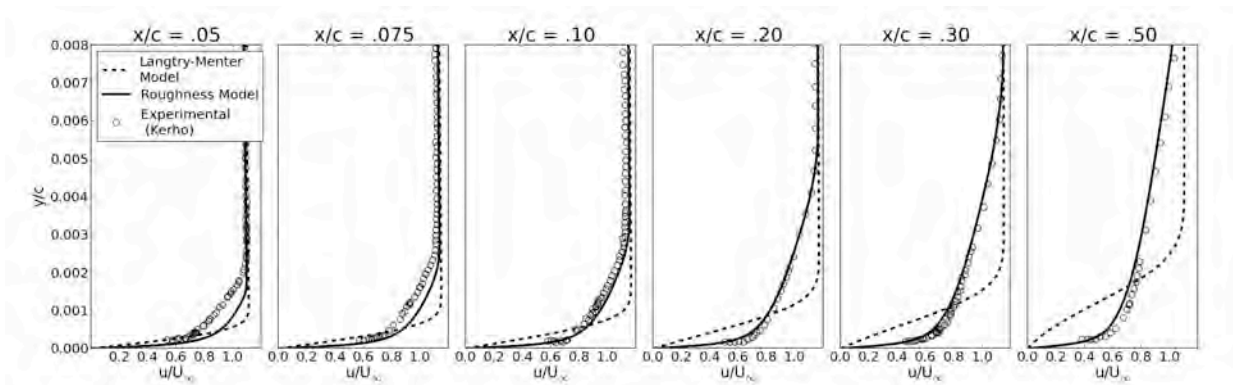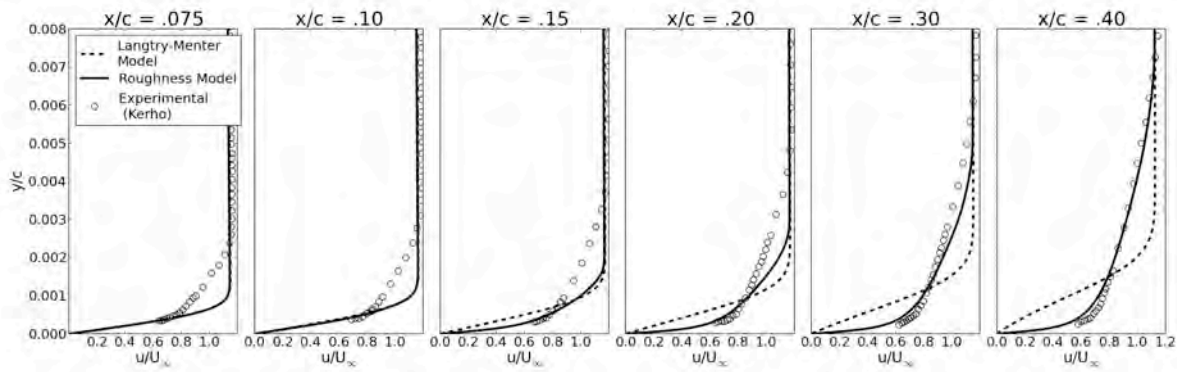
78

Figure 5.20. Boundary layer profiles: Kerho [57], unmodified Langtry-Menter transition model, computational roughness model. NACA 0012 airfoil, $Re_c = 1.25 \times 10^6$, $\alpha = 0^o$, $Tu = 0.1\%$, distributed roughness applied $x/c = 0.0314 - 0.0539$

A slight discrepancy is the shift in the profile seen in the more aft chord locations ($x/c = .40$ & $.50$). This is the result of a turbulent boundary layer developing too rapidly in the simulation, caused by a large production of k from the turbulence model. The trend was consistently observed across all roughness configurations even those which demonstrated a lag in onset prediction. The likely cause of this discrepancy is in the intermittency function in the transition model. The length of the transition region is determined within the intermittency equation, and effectively controls how rapidly the production of turbulent kinetic energy is switched on. As the model was calibrated using test cases that transition without the influence of roughness, the inability to accurately simulate the development of a roughness induced transition is not surprising. This issue and initially proposed solution is discussed in more depth after the results from the remaining cases are presented.

Another observation recorded by Kerho and Bragg was the "state" of the boundary layer at varying chord locations for all the test configurations. The categories used to describe the boundary layers were laminar, transitional, and fully turbulent. The criterion used to determine the onset of transition in the experiment was where the integrated intermittency ($\hat{\gamma} = \frac{1}{T}\int_0^T \gamma(t)\,dt$, $t \in [0,T]$) measurement began to rise.

Due to the fact in RANS simulations the fluctuating components are not resolved, it is not possible to determine the integrated intermittency parameter, therefore a different approach must be taken to determine the location of transition onset. As suggested by Thompson [100], a good indicator determining the onset of transition is the boundary layer shape factor ($H = \delta^*/\theta$). Under ideal conditions a Blasius profile will retain a constant shape factor until the onset of transition where it will drop substantially. Realistically, it takes some time for the boundary layer to develop into a characteristic laminar shape, therefore the shape factor rises initially, then plateaus, and finally begins to drop after the onset of transition. The criterion for onset used in the present study is the point after the inflection in the shape factor plot as demonstrated in Figure 5.21. Also shown is the theoretical Blasius shape factor for a laminar and turbulent boundary layer, the profile shown does not ever obtain a value comparable to a Blasius ($H = 2.59$) as the roughness promotes transition before the boundary layer fully develops to a theoretical Blasius laminar profile.

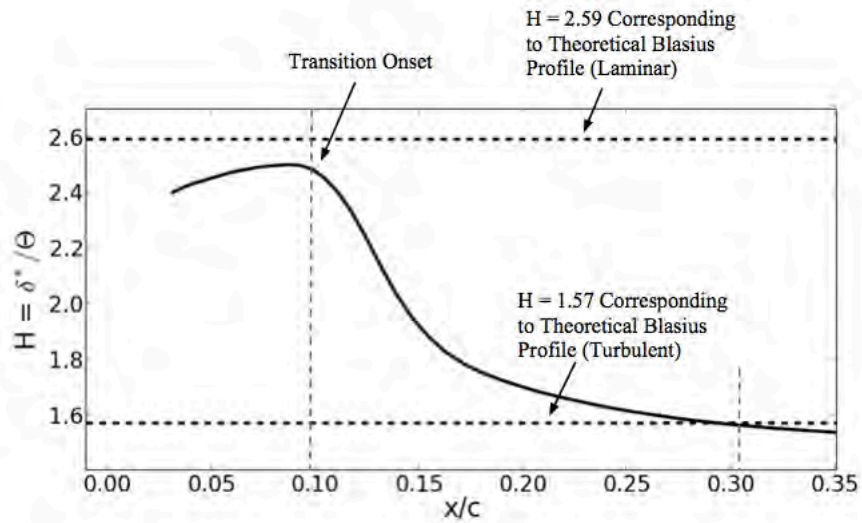**Figure 5.21.** Plot of boundary layer shape factor along chord, NACA 0012 airfoil, $Re_c = 1.25 \times 10^6$, $\alpha = 0^o$, $Tu = 0.1\%$, distributed roughness applied $x/c = 0.0314 - 0.0539$
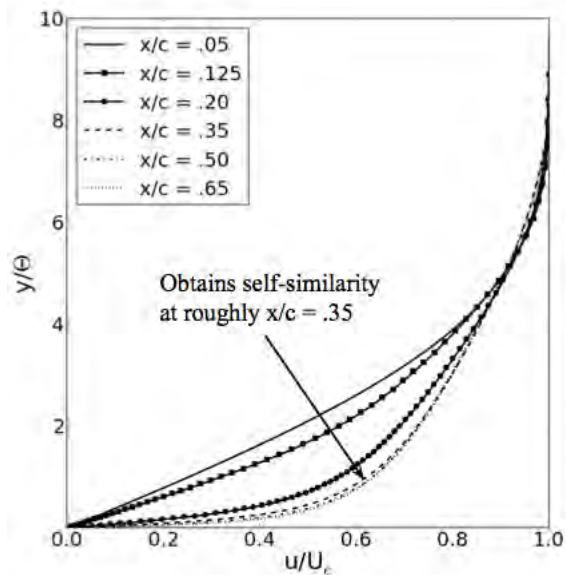

Figure 5.22. Plot of boundary layer normalized by momentum thickness at several chord locations, NACA 0012 airfoil, $Re_c = 1.25 \times 10^6$, $\alpha = 0^o$, $Tu = 0.1\%$, distributed roughness applied $x/c = 0.0314 - 0.0539$

Additionally, a criterion for where the boundary layer obtains a fully turbulent state must be established. As the boundary layer is constantly growing, there is no single profile that can be used to determine the final shape that an ideal "fully" turbulent boundary layer will obtain. The experimental study defines the location where the boundary layer obtains self-similarity when normalized by momentum thickness (θ) as a "fully" turbulent state. For consistency, the current study uses the same criteria. Figure 5.22 demonstrates how the evolving boundary layer will obtain self-similarity when normalized by momentum thickness. Additionally, one can use the point of intersection between the shape factor plot and ideal turbulent profile as a criterion for a "fully" turbulent state.

Comparison of Figures 5.21 and 5.22 shows that both methods for determining where the boundary layer achieves a fully turbulent state are in close agreement. After defining the criteria for transition onset, and obtaining a fully turbulent profile, the status of the boundary layer for various test configurations were examined. Figure 5.23 compares the results from the roughness amplification model to the experimental results of Kerho and Bragg [2].
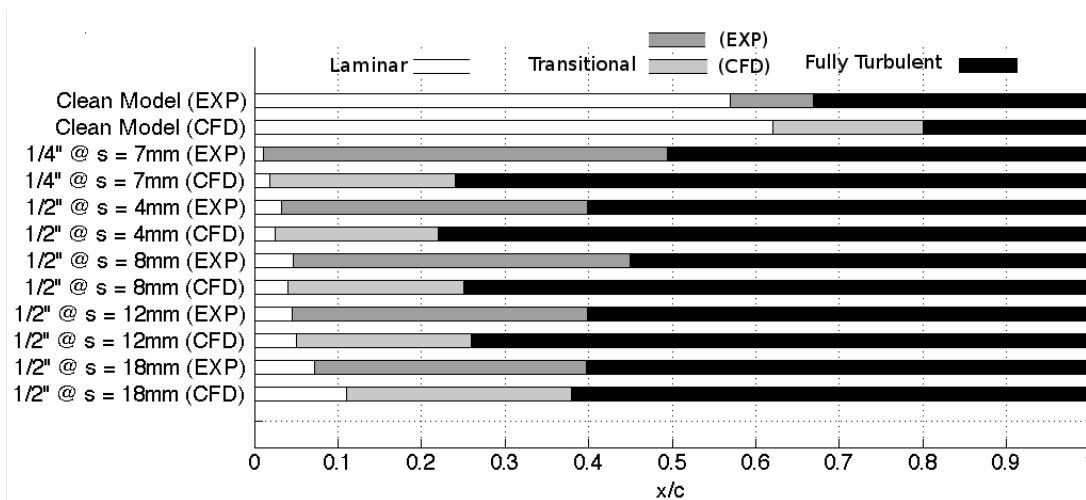
Figure 5.23. Comparison of boundary layer states for simulations run at $Re_c = 1.25 \times 10^6$, details of test configurations can be found in Table 5.1

As seen in Figure 5.23, the model does a good job tracking the change of onset location as the location of the roughness is moved along the chord. That is, the experimental test that transitions earliest is mirrored in the simulation and the relative locations of onset across the configurations match up. There is a slight delay in onset prediction in some of the cases; however, on the whole the model does a good job predicting the change in onset characteristics as the location of the roughness is moved. This has very desirable implications as despite the fact the changes in the placement of roughness are relatively small, the model is able to represent the movement of transition location consistently.

There is another very clear trend in Figure 5.23 and that is the length of the "transitional" region is repeatedly under predicted. This can be rephrased as the model forces the turbulent boundary layer to develop too rapidly. The effects of this are visible in Figure 5.18 and 5.19 where at the latter chord regions, the computationally predicted boundary layer profile is shifted to the left of the experimental. As discussed, the root of this discrepancy can be traced back to the production term of the intermittency transport equation. The calibration of the F_{length} function that determines the length of the transitional region was performed using

81

the results from the ERCOFTAC cases where transition occurred "naturally", and appears to inadequately represent roughness induced transition.

Turbulent Kinetic Energy Considerations

The observation of turbulent kinetic energy (k) levels by Kerho and Bragg [2] could potentially give insight to why the transitional region is consistently shorted by the roughness model. Across all Reynolds numbers, the roughness induced transition cases repeatedly produced a lower maximum turbulent kinetic energy value than the respective smooth configuration. The natural Tollmien-Schlichting (TS) dominated transition process has frequently been described as "explosive" once the amplification of the disturbances enters the non-linear regime [17]. This sudden and powerful appearance of turbulent fluctuations is absent in many of the roughness influenced cases recorded by Kerho [57]. Rather, a much more progressive ramping is observed with an earlier initial appearance of k. The phenomena can be seen in Figure 5.24.

Upon examination, one can see three distinct types of transition in Figure 5.24. The top "clean" configuration demonstrates a typical natural transition where a patch of high turbulence intensity is seen at the transition location. In the bottom case shown, transition is triggered using a 2-D trip strip. The mechanism by which the transition process is accelerated by a 2-D disturbance has been identified as an amplification of the natural TS disturbance waves. As follows, a similar sudden and strong appearance of turbulent fluctuations is seen at the bottom of Figure 5.24. The three middle images all include a distributed roughness strip at varying chord locations near the leading edge. The turbulence intensity pattern in the case second from the top looks very similar to the "tripped" case. This also happened to have the smallest chordwise extent of the roughness pattern. With both these considerations in mind, it can be reasoned this particular rough patch had the effect of introducing something similar to a 2-D disturbance. The remaining two configurations shown demonstrate the gradual build up of turbulent kinetic energy as discussed. This is characteristic of many of the roughness influenced cases from the Kerho [57] investigation. Additionally, the report included a large amount of discussion regarding the decreases in maximal turbulent kinetic energy observed in the roughness influenced transition. Although limited definitive conclusions can be drawn, the clear trend observed indicates markedly different turbulence behavior for roughness influenced transitions.

The Langtry-Menter model is calibrated to represent the rapid development of turbulent kinetic energy seen in free transition cases. Within the Langtry-Menter model, there is a function called F_{length} that controls the rate at which the turbulent boundary layer develops. The current roughness model merely modifies the criteria for transition onset, therefore once triggered, the model will react as if a natural transition has occurred. This is characterized by an immediate and strong appearance of k at the transition location. As discussed, Kerho and Bragg make note transition triggered by roughness will introduce turbulent kinetic energy in a markedly different manner. Therefore, a recalibration of F_{length} function within the Langtry-Menter model could potentially allow the model to better represent a developing roughness influenced boundary layer. Unfortunately, the modification is not trivial as F_{length} and $\tilde{Re}_{\theta,t}$ are strongly coupled and small changes can result in dramatic changes to the model globally. Nonetheless, a potential modification ought to be explored due to the substantial differences in turbulent kinetic energy production seen between clean and rough configurations in experiments.
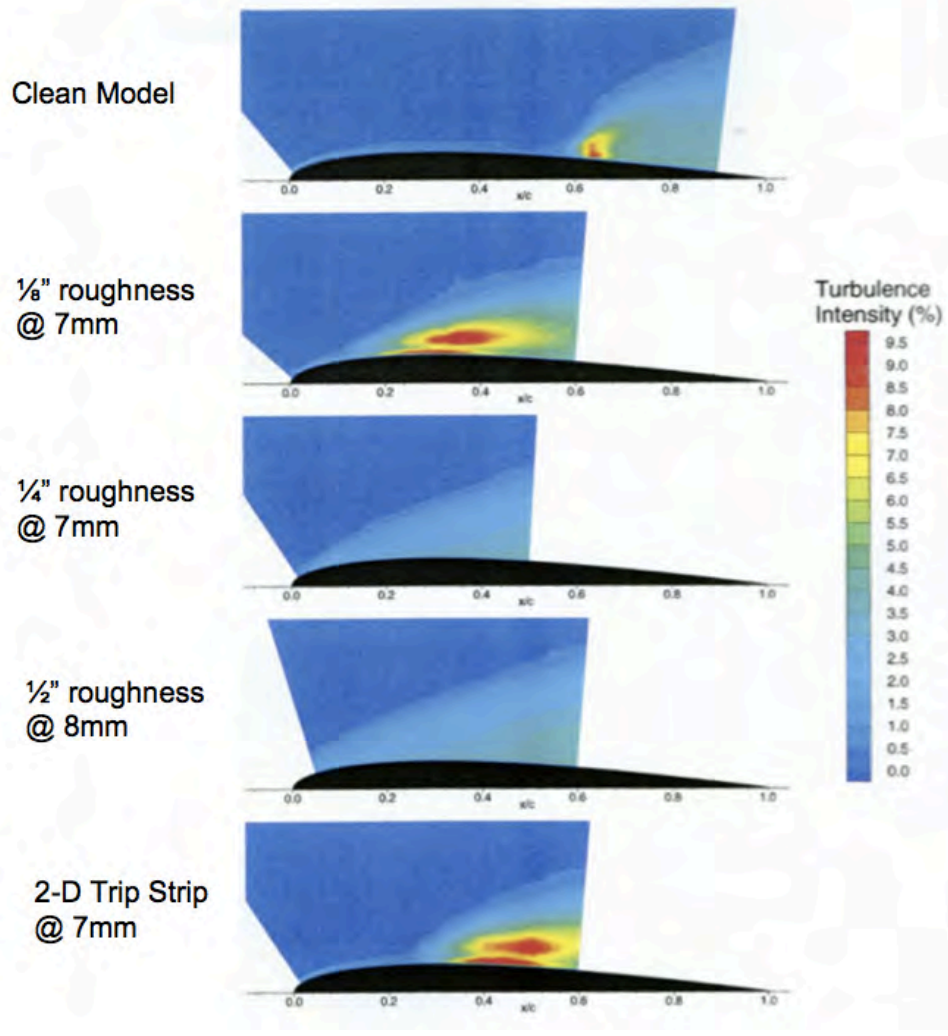
Figure 5.24. Contours of turbulence intensity for varying clean and rough configurations, NACA 0012, $Re_c = 1.25 \times 10^6$, adapted from Kerho [57]

Comparison With Texas A&M Tunnel Tests - NACA 63_3- 418 Airfoil

The following section contains comparisons to the experimental results from the companion Texas A&M LSWT experimental campaign. Tests at Reynolds numbers of 1.6×10^6 and 2.4×10^6 are chosen initially for comparison at this intermediate range of Reynolds numbers the transition location is shown to shift upstream more gradually with an increase in angle of attack than at higher Reynolds numbers. This progressive shift provides better results to calibrate the computational model against.

Additionally, the variable of roughness density must be considered. Markedly different behavior has been observed both historically and in the current study regarding the flow over distributed roughness of varying densities. As the roughness model was initially calibrated on cases with densely distributed surface roughness, the Texas A&M cases with highest distribution density were selected to further verify the model. This is the reason the "140 Dense" experimental results are shown in the following plots. The 140 corresponds to a roughness height of 140 μm ($k/c = 170 \times 10^{-6}$) and the density is such that 15% of the "contaminated" area is covered by randomly distributed circles and ellipsoids.

Figure 5.25. Comparison of upper surface transition location as indicated by experimental results and predictions by computation roughness model, NACA $63_3 - 418$, $Re_c = 1.6 \times 10^6$, roughness with $k/c = 170 \times 10^{-6}$ applied $x/c = -0.12 : 0.04$

The result in Figures 5.25 and 5.26 demonstrate the model does an adequate job of tracking the change transition location along the upper surface. A slight concern is that the model does not progressively move the transition location forward with an increase in angle of attack, as is indicated by the experimental results. Despite this, the model still properly identifies the critical angle of attack (the angle of attack such that the
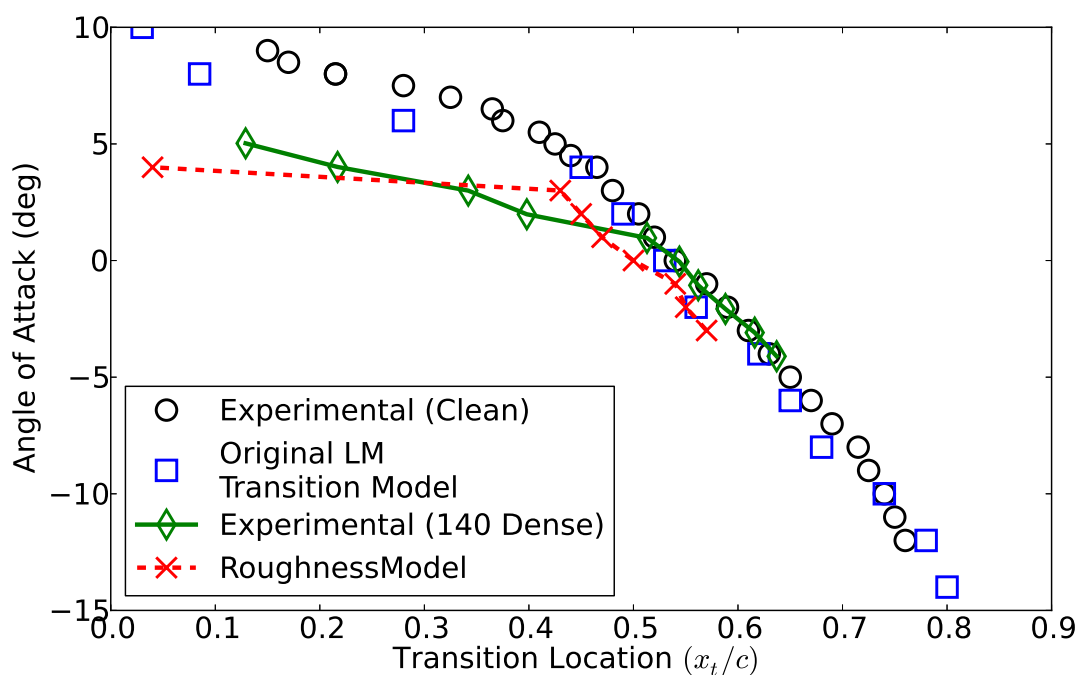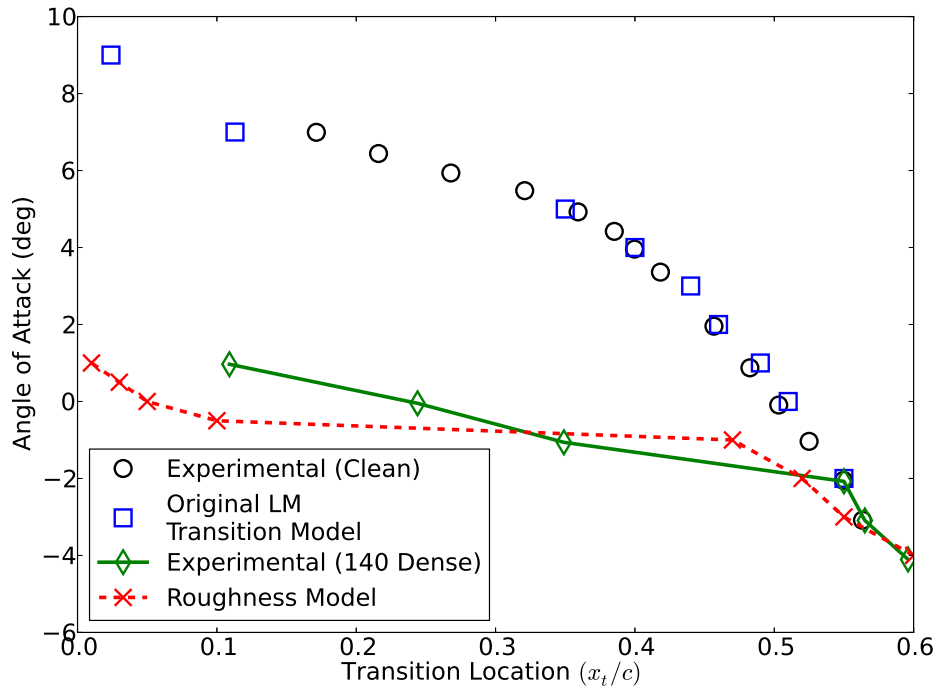
Figure 5.26. Comparison of upper surface transition location as indicated by experimental results and predictions by computation roughness model, NACA $63_3 - 418$, $Re_c = 2.4 \times 10^6$, roughness with $k/c = 170 \times 10^{-6}$ applied $x/c = -0.12 : 0.04$

transition moves rapidly forward) range for this roughness configuration at both Reynolds numbers. The results are promising as the primary purpose of the roughness model is to modify the transition criteria within the transition model.

Although it is a necessary comparison, the upper surface transition location alone does not imply complete accuracy of the model. Additional results are provided that show how the predicted lift and drag coefficients compare to the experimental results. The comparisons in Figures 5.27 and 5.28 indicate the model causes an overprediction of drag. Upon further investigation, it was observed that the roughness model forces the boundary layer along the lower surface of the airfoil to transition too far forward in the cases that show discrepancies. As a consequence, a larger production of turbulent kinetic energy was predicted with the effect of increasing the drag coefficient substantially.

The results are not entirely unexpected as calibration of the roughness model has been based primarily on flow cases where chordwise pressure gradients encountered are generally small. The differences in pressure gradients observed on the lower and upper surface result in changes to the transition behavior. The effect is more prominent under the influence of a strongly favorable pressure gradient, which has been shown to dampen out some of the roughness effects. The model at this stage of development does not explicitly account for pressure gradients. This is clearly a limitation that needs to be addressed during subsequent model development.

Comparisons of the predicted and measured drag polars in Figures 5.27 and 5.28 indicate that at approx-

imately zero angle of attack, where pressure gradients tend to be small, the model accurately predicts the drag coefficient. However, as the angle of attack increases or decreases the chordwise pressure gradients increase and with that the model overpredicts drag. The fact the drag predictions from the model begin to converge with the experimental at higher lift coefficients can be explained by recognizing at higher angles of attack the boundary layer tends to transition close to the leading edge even without roughness.

It has long been observed that pressure gradients influence roughness effects on flow behavior. However, there has been little comprehensive work done studying how to model the combined effects. It has been proposed a pressure gradient correction factor be added to the formulation of the roughness model to adjust the predicted transition behavior in the presence of a strong pressure gradient. This should allow more robust calculation of transition location under the influence of roughness on surfaces exposed to large pressure gradients.

Figure 5.27. Comparison of drag polars- experimental results and predictions by computation roughness model, NACA $63_3 - 418$, $Re_c = 1.6 \times 10^6$, roughness with $k/c = 170 \times 10^{-6}$ applied $x/c = -0.12 : 0.04$
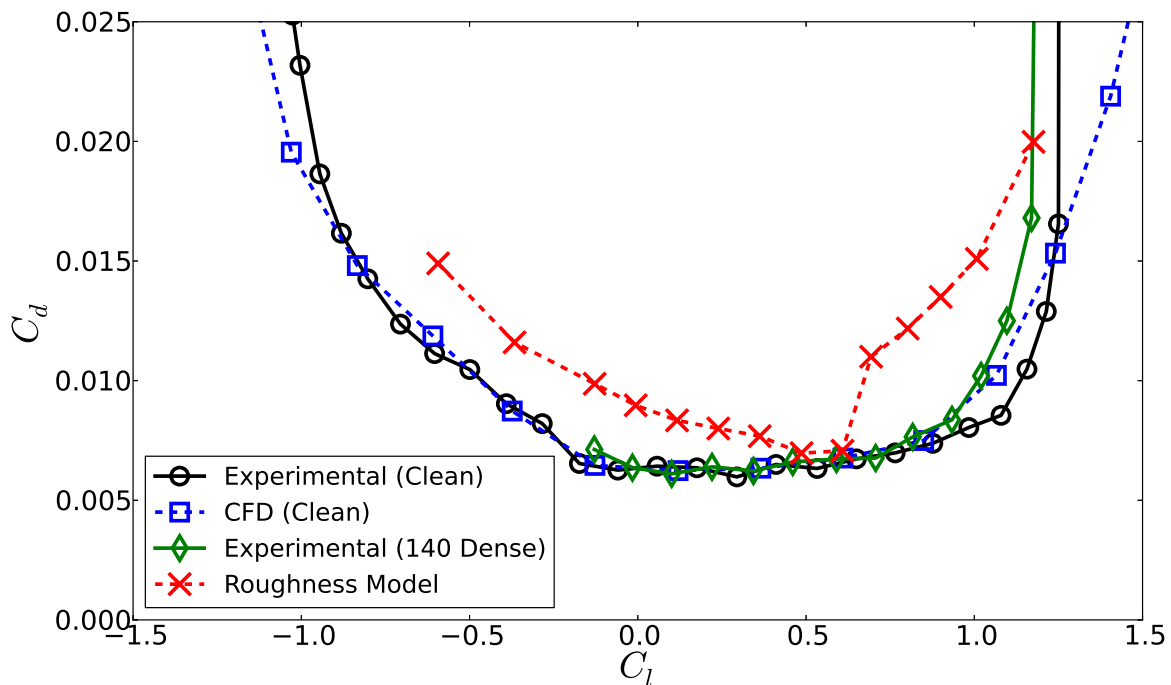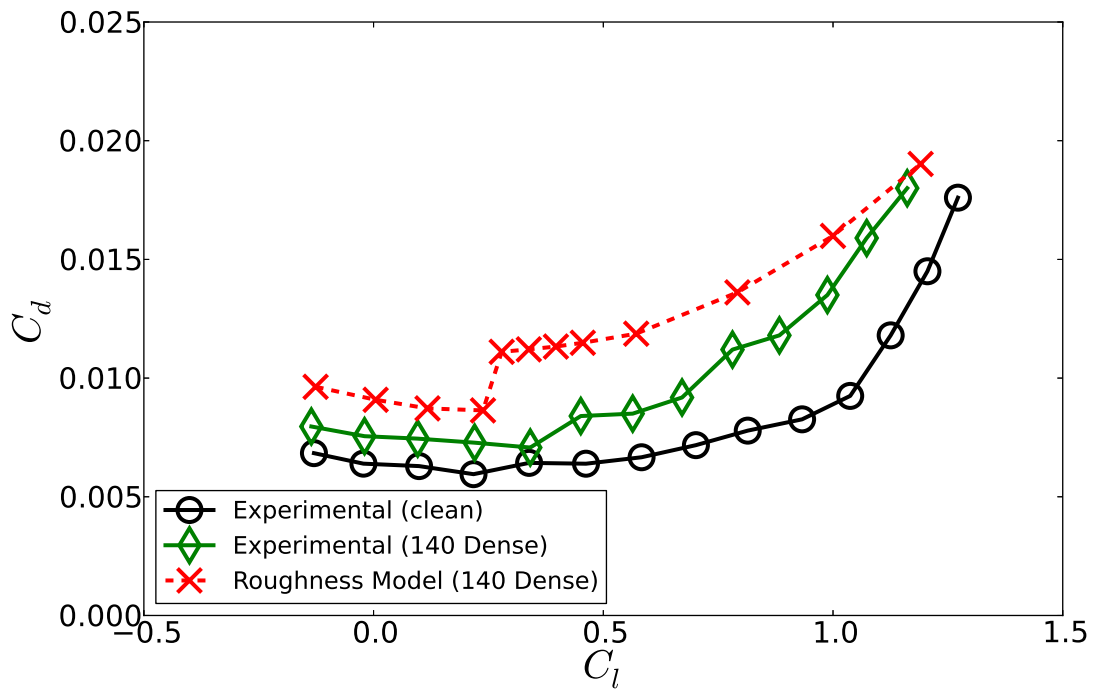
Figure 5.28. Comparison of drag polars- experimental results and predictions by computation roughness model, NACA $63_3 - 418$, $Re_c = 2.4 \times 10^6$, roughness with $k/c = 170 \times 10^{-6}$ applied $x/c = -0.12 : 0.04$

Chapter 6

Conclusions

A computational model to emulate the effects of surface roughness has been successfully implemented in the flow solver OVERFLOW-2. An additional transport equation was used to account for non-local effects that roughness will have on the flow over a contaminated surface. The new scalar variable is coupled with the Langtry-Menter transition model and modifies the criteria for transition onset accordingly. The implementation of the model has proven to be stable in all tests conducted and only slightly slows the convergence of the transition model. In addition to implementing the roughness amplification method to account for the effects of roughness on the transition process, a modification to the rough wall turbulent boundary condition has been implemented. The calibration of the model was performed on a variety of flat plate test cases with varying pressure gradients as a comparison to original implementation of Dassler, Kozulovic, and Fiala [68]. Additionally, calibration tests were conducted on a NACA 0012 airfoil with large scale leading edge roughness applied at numerous chord locations. The results from the tests on the NACA 0012 are very promising and the model has proven to accurately represent the change in transition location observed under the influence of numerous roughness configurations. Preliminary comparisons of the computational model to the concurrent Texas A&M wind tunnel experiment have revealed both the strengths and weaknesses of the present formulation. Transition locations are reasonably predicted on the upper airfoil surface, however the model lacks the ability to account for the roughness mitigating effects of a highly favorable pressure gradient.

As the Langtry-Menter transition model is the platform on which the roughness amplification model is built, a portion of this work is dedicated to the foundations of the model. Additionally, a number of case studies were performed to asses the range of the transition model's validity, including a comparison with the experiments performed at Texas A&M. Several suggestions are presented to help remedy the issue of the dominate influence of freestream turbulence intensity. Also, issues regarding non-physical turbulence dissipation were highlighted and possible solutions explored.

Next Steps

The current work is part of a collaboration and there are several stages of the model's development still in progress. A large number of wind tunnel experiments have been performed at the Texas A&M Oran W. Nicks Low Speed Wind Tunnel (LSWT) on a NACA $63_3 - 418$ airfoil with different leading edge roughness configurations. Multiple roughness heights and densities were used across a large range of Reynolds numbers to create a massive data set to further calibrate the model.

As discussed the roughness model does not currently have the capacity to account for the potentially dominant effects of a strong pressure gradient. A new formulation is being pursued that will explicitly

account for these pressure gradient effects. This will hopefully extend the models validity to flows over rough surfaces under the influence of a pressure gradient.

In the initial calibration runs, the effect of roughness density was not included in the model formulation. After the first round of tunnel results where it was observed the density of the roughness had a first order effect on transition location, it became clear a second parameter would be needed. Tests were then performed to further determine the detailed effects of roughness density. The data from these experiments is still being analyzed and will be used to extensively calibrate the roughness model. A full analysis of these tests will be published in a subsequent report.

References

[1] J. Bons, "A review of surface roughness effects in gas turbines," *Journal of Turbomachinery*, vol. 132, no. 021004, pp. 1–16, 2010.

[2] M. Kerho and M. Bragg, "Airfoil boundary-layer development and transition with large leading-edge roughness," *AIAA Journal*, vol. 35, no. 1, pp. 75–84, 1997.

[3] R. Mayle, "The role of laminar-turbulent transition in gas turbo engines," *Journal of Turbomachinery*, vol. 113, no. 4, pp. 509–537, 1991.

[4] M. Keegan, D. Nash, and M. Stack, "On erosion issues associated with the leading edge of wind turbine blades," *Journal of Applied Physics*, vol. 46, pp. 1–20, 2013.

[5] A. Sareen, C. Sapre, and M. Selig, "Effects of leading edge erosion on wind turbine blade performance," *Wind Energy*, vol. DOI: 10.1002/we.1649, 2013.

[6] R. van Rooij and W. Timmer, "Roughness sensitivity considerations for thick rotor blade airfoils," *Journal of Solar Energy Engineering*, vol. 125, pp. 468–478, 2003.

[7] R. Ramsay, M. Hoffmann, and G. Gregorek, "Effects of grit roughness and pitch oscillations on the s815 airfoil," Tech. Rep. 442-7820, National Renewable Energy Lab, 1996.

[8] D. Berg, "A review of the workshop on WECS blade-surface roughness," in *ASME Wind Energy Symposium*, 1994.

[9] T. Pulliam, "High order accurate finite-difference methods: as seen in overflow," in *AIAA Computational Fluid Dynamics Conference*, 2011.

[10] L. Rayleigh, "On the stability of instability of certain fluid motions," *Proc. London Math. Soc*, vol. s1-11, no. 1, pp. 57–72, 1879.

[11] G. Schubauer and H. Skramtad, "Laminar-boundary-layer oscillations and transition," Tech. Rep. 909, National Advisory Committee for Aeronautics, 1943.

[12] P. Klebanoff, K. Tidstrom, and L. Sargent, "The three-dimensional nature of boundary-layer instability," tech. rep., National Bureau of Standards, 1961.

[13] T. Herbert, "Secondary instabilities of boundary layers," *Annual Review of Fluid Mechanics*, vol. 20, pp. 487–526, 1988.

[14] A. Craik, "Wave-induced longitudinal-vortex instability in shear flows," *Journal of Fluid Mechanics*, vol. 125, pp. 37–52, 1982.

[15] E. V. Driest and C. Blumer, "Boundary layer transition: Freestream turbulence and pressure gradient effects," *AIAA Journal*, vol. 1, no. 6, pp. 1303–1306, 1963.

[16] G. Schubauer and P. Klebanoff, "Contributions on the mechanics of boundary-layer transition," Tech. Rep. 3489, National Advisory Committee for Aeronautics, 1955.

[17] H. Schlichting, *Boundary-Layer Theory*. McGraw-Hill, 6th ed., 1968.

[18] M. Morkovin, "Bypass transition to turbulence and research desiderata," Tech. Rep. CP-2386, NASA, 1984.

[19] C. van Dam, S. Los, and S. Miley, "In-flight boundary-layer state measurements on a high-lift system: Slat," *Journal of Aircraft*, vol. 34, no. 6, pp. 748–756, 1997.

[20] C. van Dam, S. Los, and S. Miley, "In-flight boundary-layer state measurements on a high-lift system: Main element and flap," *Journal of Aircraft*, vol. 34, no. 6, pp. 757–763, 1997.

[21] E. Mayda and C. van Dam, "Bubble-induced unsteadyness on a wind turbine airfoil," *Journal of Solar Energy Engineering*, vol. 124, pp. 335–344, 2002.

[22] W. Elsner, "Transition modelling in turbomachinery," *Journal of Theoretical and Applied Mechanics*, vol. 45, no. 3, pp. 539–556, 2007.

[23] P. Durbin, G. Medic, J. Seo, J. Eaton, and S. Song, "Rough wall modification of two layer $k - \varepsilon$," *Journal of Fluids Engineering*, vol. 123, pp. 16–21, 2001.

[24] W. Saric, H. Reed, and E. White, "Stability and transition of three-dimensional boundary layers," *Annual Review of Fluid Mechanics*, vol. 35, pp. 413–440, 2003.

[25] M. Germano, M. Piomelli, P. Moin, and W. Cabot, "A dynamic subgrid-scale eddy-viscosity model," *Physics of Fluids*, vol. 3, no. 7, pp. 1760–1765, 1991.

[26] J. van Ingen, "A suggested semi-empirical method for the calculation of the boundary layer transition region," Tech. Rep. VTH-74, Technische Hogeschool Vliegtuigbouwkunde, 1956.

[27] J. van Ingen, "The e^n method for transition prediction. historical review of work at tu delft," in *38th Fluid Dynamics Conference and Exhibit*, 2008.

[28] C. Merkle and T. Kubota, "An analytical study of the effects of surface roughness on boundary-layer transition," Tech. Rep. AD/A-004 786, Flow Research Inc., 1973.

[29] R. Brodeur and C. van Dam, "Transition prediction for a two-dimensional Reynolds-averaged Navier-Stokes method applied to wind turbine airfoils," *Wind Energy*, vol. 4, pp. 61–75, 2001.

[30] E. Mayda, *Boundary-layer Transition Prediction for Reynolds-averaged Navier-Stokes Methods*. PhD thesis, University of California, Davis, 2007.

[31] B. Abu-Ghannam and R. Shaw, "Natural transition of boundary layers - the effects of turbulence, pressure gradient and flow history," *Journal of Mechanical Engineering Sciences*, vol. 22, no. 5, pp. 213–228, 1980.

[32] K.-Y. Chien, "Predictions of channel and boundary-layer flows with a low-Reynolds-number turbulence model," *AIAA Journal*, vol. 20, no. 1, pp. 33–38, 1982.

[33] S. Dhawan and R. Narasimha, "Some properties of boundary layer flow during the transition form laminar to turbulent motion," *Journal of Fluid Mechanics*, vol. 3, no. 4, pp. 418–436, 1958.

[34] J. Gostelow, A. Blunden, and G. Walker, "Effects of freestream turbulence and adverse pressure gradients on boundary layer transition," *Journal of Turbomachinery*, vol. 116, no. 3, pp. 392–404, 1994.

[35] J. Steelant and E. Dick, "Modelling of bypass transition with conditioned Navier-Stokes equations coupled to an intermittency transport equation," *International Journal for Numerical Methods in Fluids*, vol. 23, pp. 193–220, 1996.

[36] F. Menter, T. Esch, and S. Kubacki, "Transition modelling based on local variables," in *5th International Symposium on Engineering Turbulence Modelling and Measurements*, 2002.

[37] R. Langtry and F. Menter, "Correlation-based transition modeling for unstructured parallelized computation fluid dynamics codes," *AIAA Journal*, vol. 47, no. 12, pp. 2894–2906, 2009.

[38] T. Corke, A. Bar-Sever, and M. Morkovin, "Experiments on transition enhancement by distributed roughness," *Physics of Fluids*, vol. 29, no. 10, pp. 3199–3213, 1986.

[39] H. Dryden, "Combined effects of turbulence and roughness on transition," *ZAMP Zeitschrift für Angewandte Mathematik und Physik*, vol. 9, no. 5-6, pp. 249–258, 1958.

[40] J. Kendall, "The effect of small-scale roughness on the mean flow profile of a laminar boundary layer," *Instability and Transition*, vol. 1, pp. 296–302, 1990.

[41] P. Klebanoff and K. Tidstrom, "Mechanism by which a two-dimensional roughness element induces boundary-layer transition," *Physics of Fluids*, vol. 15, no. 7, pp. 1173–1186, 1972.

[42] F. Ergin and E. White, "Unsteady and transitional flows behind roughness elements," *AIAA Journal*, vol. 44, no. 11, pp. 2504–2514, 2006.

[43] M. Acalar and C. Smith, "A study of hairpin vortices in a laminar boundary layer. part 1. hairpin vortices generated by a hemisphere protuberance," *Journal of Fluid Mechanics*, vol. 175, pp. 1–41, 1987.

[44] I. Tani, H. Komoda, and Y. Komatsu, "Boundary-layer transition by isolated roughness," Tech. Rep. 375, Aeronautical Research Institute, University of Tokyo, 1962.

[45] N. Gregory and W. Walker, "The effect of transition of isolated surface excrescences in the boundary layer," Tech. Rep. 2779, Aeronautical Research Council, 1951.

[46] M. Mochizuki, "Smoke observations on boundary layer transition caused by a spherical roughness element," *Journal of Physical Society of Japan*, vol. 16, no. 5, pp. 995–1007, 1961.

[47] P. Klebanoff, W. Cleveland, and K. Tidstrom, "On the evolution of a turbulent boundary layer induced by a three-dimensional roughness element," *Journal of Fluid Mechanics*, vol. 237, pp. 101–187, 1992.

[48] R. Norman, *On Obstacle-generated Secondary Flows in Laminar Boundary Layers and Transition to Turbulence*. PhD thesis, Illinois Institute of Technology, 1972.

[49] M. Bernardini, S. Pirozzoli, P. Orlandi, and S. Lele, "Compressible boundary layer transition induced by isolated roughness elements," in *Center for Turbulence Research, Proceedings of the Summer Program*, 2012.

[50] J. Nikuradse, "Laws of flow in rough pipes," Tech. Rep. 1292, NACA, 1933.

[51] A. Braslow and E. Knox, "Simplified method for determination of critical height of distributed roughness particles for the boundary-layer transition at mach numbers from 0 to 5," Tech. Rep. 4363, National Advisory Committee for Aeronautics, 1958.

[52] I. Gartshore and K. D. Croos, "Roughness element geometry required for wind tunnel simulations of the atmospheric wind," *Journal of Fluids Engineering*, vol. 99, no. 3, pp. 480 – 485, 1976.

[53] M. Stripf, A. Schulz, H.-J. Bauer, and S. Wittig, "Extended models for transitional rough wall boundary layers with heat transfer - part i: Model formulations," *Journal of Turbomachinery*, vol. 131, no. 031016, pp. 1–10, 2009.

[54] W. Elsner and P. Warzecha, "Numerical study of transitional rough wall boundary layers," *Journal of Turbomachinery*, vol. 136, no. 011010, pp. 1–11, 2014.

[55] E. Feindt, "Untersuchungen uber die abha ngigkeit des umschlages laminar turbulent von der oberfla chenrauhigkeit und der druckverteilung," *DFL Bericht*, vol. 43, 1956.

[56] L. Levanthal and E. Reshotko, "Preliminary experimental study of disturbances in a laminar boundary-layer due to distributed surface roughness," Tech. Rep. 81-0588, Case Western Reserve University, 1981.

[57] M. Kerho, *Effect of Large Distributed Roughness Near an Airfoil Leading Edge on Boundary-Layer Development and Transition*. PhD thesis, University of Illinois at Urbana-Champaign, 1995.

[58] K. Singh and J. Lumley, "Effect of roughness on the velocity profile of a laminar boundary layer," *Applied Science Res.*, vol. 24, pp. 168–186, 1971.

[59] M. Lessen and S. Gangwani, "Effect of small amplitude waviness upon the stability of laminar boundary layers," *Physics of Fluids*, vol. 19, no. 4, pp. 510–514, 1976.

[60] R. Downs, E. White, and N. Denissen, "Transient growth and transition induced by random distributed roughness," *AIAA Journal*, vol. 46, no. 2, pp. 451–462, 2008.

[61] E. Reshotko and A. Tumin, "Role of transient growth in roughness-induced transition," *AIAA Journal*, vol. 42, no. 4, pp. 766–770, 2004.

[62] E. White, "Transient growth of stationary disturbances in a flat plate boundary layer," *Physics of Fluids*, vol. 14, no. 12, pp. 4429–4439, 2002.

[63] J. van Rij, B. Belnap, and P. Ligrani, "Analysis and experiments on three-dimensional, irregular surface roughness," *Journal of Fluids Engineering*, vol. 124, pp. 1–7, 2002.

[64] Q. Zang, S. Lee, and P. Ligrani, "Effects of surface roughness and turbulence intensity on the aerodynamic losses produced by the suction surface of a simulated turbine airfoil," *Journal of Fluids Engineering*, vol. 126, pp. 257–265, 2003.

[65] A. Hellsten and S. Laine, "Extension of the $k - \omega$ - sst turbulence model for flows over rough surfaces," in *AIAA Atmospheric Flight Mechanics Conference*, 1997.

[66] B. Aupoix and P. Spalart, "Extensions of the spalart-allmaras turbulence model to account for wall roughness," *International Journal of Heat and Fluid Flow*, vol. 24, no. 4, pp. 454–462, 2003.

[67] N. Denissen and E. White, "Continuous spectrum analysis of roughness-induced transient growth," *Physics of Fluids*, vol. 21, no. 114105, pp. 1–13, 2009.

[68] P. Dassler, D. Kozulovic, and A. Fiala, "Modelling of roughness-induced transition using local variables," in *V European Conference on Computational Fluid Dynamics*, 2010.

[69] P. Dassler, D. Kozulovic, and A. Fiala, "An approach to modelling the roughness-induced boundary layer transition using transport equations," in *European Congress on Computational Methods in Applied Sciences and Engineering*, 2012.

[70] C. Navier, "Mémoire sur les lois du mouvement des fluides," *Mem. Acad. R. Sci. Paris*, vol. 6, pp. 389–416, 1823.

[71] A. Cauchy, *Exercises de mathmatiques*. Bure Bure frres, 1828.

[72] G. Stokes, "On the theories of internal friction of fluids in motion," *Trans. Camb. Phil. Soc.*, vol. 8, pp. 287–305, 1845.

[73] C. Wang, "Exact solutions of the steady-state Navier Stokes equations," *Annual Review of Fluid Mechanics*, vol. 23, pp. 159–177, 1991.

[74] A. Chorin, "Numerical solution of the Navier-Stokes equations," *Mathematics of Computation*, vol. 22, pp. 745–762, 1968.

[75] L. Berselli, T. Iliescu, and W. Layton, *Mathematics of Large Eddy Simulation of Turbulent Flows*. Springer, 2006.

[76] D. Wilcox, *Turbulence Modeling for CFD*. DCW Industries, 2006.

[77] E. van Driest, "On turbulent flow near a wall," *Journal of the Aeronautical Sciences*, vol. 23, no. 11, pp. 1007–1011, 1956.

[78] B. Baldwin and T. Barth, "A one-equation turbulence transport model for high Reynolds number wall-bounded flows," Tech. Rep. 102847, NASA, 1990.

[79] P. Spalart and S. Allmaras, "A one-equation turbulence model for aerodynamic flows," in *30th Aerospace Sciences Meeting and Exhibit*, 1992.

[80] J. Bardina, P. Huang, and T. Coakley, "Turbulence modeling, validation, testing and development," Tech. Rep. 110446, NASA, 1997.

[81] L. Kral, "Recent experience with different turbulence models applied to the calculation of flow over aircraft," *Progress in Aerospace Sciences*, vol. 34, pp. 481–541, 1998.

[82] W. Jones and B. Launder, "The prediction of laminarization with a two-equation model of turbulence," *International Journal of Heat and Mass Transfer*, vol. 15, pp. 301–314, 1972.

[83] D. Wilcox, "Multiscale model for turbulent flows," *AIAA Journal*, vol. 26, pp. 1311–1320, 1988.

[84] D. Wilcox, "A half century historical review of the $k - \omega$ model," in *29th Aerospace Sciences Meeting*, 1991.

[85] F. Menter, "Improved two-equation $k - \omega$ turbulence models for aerodynamic flows," Tech. Rep. 103975, NASA, 1992.

[86] B. Launder, G. Reece, and W. Rodi, "Progress in the development of a Reynolds-stress turbulent closure," *Journal of Fluid Mechanics*, vol. 68, no. 3, pp. 537–566, 1975.

[87] C. Spezial, S. Sarkar, and T. Gatski, "Modeling the pressure-strain correlation of turbulence: an invariant dynamical systems approach," *Journal of Fliud Mechanics*, vol. 227, pp. 245–272, 1991.

[88] S. Nasizima and A. Yoshizawa, "Turbulent channel and Couette flows using an anisotropic $k - \varepsilon$ model," *AIAA Journal*, vol. 25, no. 3, pp. 414–420, 1987.

[89] P. Spalart, W. Jou, M. Strelets, and S. Allmaras, "Comments on the feasibility of les for wings, and on a hybrid RANS/LES approach," in *Advances in DNS/LES, 1st AFOSR International Conerence on DNS/LES*, 1997.

[90] R. Chow and C. van Dam, "Verification of computational simulations of the nrel 5 mw rotor with a focus on inboard flow separation," *Wind Energy*, 2011.

[91] P. Spalart, "Detached-eddy simulation," *Annual Review of Fluid Mechanics*, vol. 41, pp. 181–202, 2009.

[92] T. Pulliam and D. Chaussee, "A diagonal form of an implicit approximate-factorization algorithm," *Journal of Computational Physics*, vol. 39, pp. 347–363, 1981.

[93] T. Pulliam, "Development of implicit methods in cfd nasa ames research center 1970's - 1980's," *Computers and Fluids*, vol. 41, pp. 65–71, 2011.

[94] R. Langtry, *A Correlation-Based Transition Model using Local Variables for Unstructured Parallelized CFD codes*. PhD thesis, University of Stuttgart, Germany, 2006.

[95] A. Savill, *Some Recent Progress in the Turbulence Modeling of By-pass Transition*. Elsevier Science Publishers, 1993.

[96] P. Spalart and C. Rumsey, "Effective inflow conditions for turbulence models in aerodynamic calculations," *AIAA Journal*, vol. 45, no. 10, pp. 2544–2558, 2007.

[97] R. Ehrmann, E. White, D. Maniaci, R. Chow, C. Langel, and C. van Dam, "Realistic leading-edge roughness effects on airfoil performance," in *31st Applied Aerodynamics Conference*, 2013.

[98] P. Khayatzadeh and S. Nadarajah, "Laminar-turbulent flow simulation for wind turbine profiles using the $\gamma - \tilde{r}e_{\theta t}$ transition model," *Wind Energy*, vol. DOI: 10.1002/we.1606, pp. 1–18, 2013.

[99] D. Wilcox, "Simulation of transition with a two-equation turbulence model," *AIAA Journal*, vol. 32, no. 2, pp. 247–255, 1994.

[100] B. Thompson, "A critical review of existing methods of calculating the turbulent boundary layer," Tech. Rep. 3447, Aeronautical Research Council Reports and Memoranda, 1967.

DISTRIBUTION

External (electronic)

M. Derby   Department of Energy

SNL Internal (electronic)

MS0825	M. F. Barone	1515
MS1124	D. C. Maniaci	8821
MS1124	D. G. Minster	8821
MS1124	J. A. Paquette	8821
MS0899	Technical Library	9536

Sandia National Laboratories